UC Berkeley
UC Berkeley Electronic Theses and Dissertations

Title

Supramolecular Assembly of Halide Perovskite Building Blocks

Permalink

https://escholarship.org/uc/item/0bd3j7gc

Author

Zhu, Cheng

Publication Date

2024

Peer reviewed|Thesis/dissertation

eScholarship.org Powered by the California Digital Library
University of California

Supramolecular Assembly of Halide Perovskite Building Blocks

By

Cheng Zhu

A dissertation submitted in partial satisfaction of the

requirements for the degree of

Doctor of Philosophy

in

Engineering – Materials Science and Engineering

in the

Graduate Division

of the

University of California, Berkeley

Committee in charge:

Professor Peidong Yang, Chair

Professor Mark Asta

Professor David Limmer

Spring 2024

Supramolecular Assembly of Halide Perovskite Building Blocks

© Copyright 2024
Cheng Zhu
All rights reserved

Abstract

Supramolecular Assembly of Halide Perovskite Building Blocks

by

Cheng Zhu

Doctor of Philosophy in Engineering – Materials Science and Engineering

University of California, Berkeley

Professor Peidong Yang, Chair

In recent years, there has been significant attention drawn towards metal halide perovskites, a class of semiconducting materials distinguished by their remarkable optoelectronic properties. In the halide perovskite structure, the metal halide octahedron ($[BX_6]^{n-}$, B = metal cation, X = halide anion) is the fundamental building block and functional unit. This dissertation aims to present a novel perspective by proposing a supramolecular approach to manipulate the metal halide octahedral building blocks. The new supramolecular building block is constructed from the ionic halide perovskite octahedral unit and crown ether supramolecular cations, resulting in the formation of a novel (crown-ether@A)$_2BX_6$ (A = alkali metal cation) dumbbell structural unit. The chemistry, properties, and application of this supramolecular approach constitute the main topics of this dissertation.

Chapter 1 provides an overview of halide perovskite materials, encompassing their structure, synthesis, properties, and applications. The concept of dimensionality in halide perovskites and the significance of the metal halide octahedral $[BX_6]^{n-}$ building blocks are introduced, laying the foundation for the subsequent discussion on the supramolecular assembly approach. In Chapter 2, we delve into the details of the supramolecular assembly approach, highlighting its structural and compositional adaptability, along with its immense potential in various optoelectronic applications. Chapter 3 delves into the synthesis and characterization of two new blue and green emitters with near-unity photoluminescence quantum yield (PLQY), (18-Crown-6@K)$_2HfBr_6$ and (18-Crown-6@K)$_2ZrCl_4Br_2$, derived from the supramolecular assembly approach. Comprehensive optical studies of these materials are presented, along with demonstrations of their applications in display and 3D-printing technologies. Lastly, chapter 4 provides a summary of the research findings and offers insights into the future directions for the supramolecular assembly approach, establishing a solid foundation for the future development and application of halide perovskites.

Table of Contents

Acknowledgements

Ph.D. has been a very challenging and extremely fruitful experience for me. It is challenging both intellectually and mentally, and I could not imagine myself conquering it without the invaluable help and support from my advisor, colleagues, friends and family.

First and foremost, I would like to express my sincerest gratitude for my advisor, Prof. Peidong Yang. He took me under his wing and shaped me into the person that I am today. Every accomplishment I achieved is not possible without his invaluable guidance and support throughout the past five years. When I was struggling in finding my thesis project in my first two years, he offered enormous help and encouragement. When I showed a weakness, he cared about me and showed me how to improve. He cared not only about my research, but also my career and life. We had many conversations about my future development, and I will forever remember his words and wisdom. He has made me into a creative and critical thinker and a tough and confident young man.

Moreover, I would like to extend my gratitude to all the UC Berkeley professors that I have guided and helped me during my Ph.D. I would like to thank my qualifying exam committee chair, Prof. Mark Asta, and committee members Prof. David Limmer, Prof. Jie Yao, and Prof. Joel Ager. They helped me established the foundation for my Ph.D. thesis, and their invaluable suggestions and guidance carried all the way towards the later stages of my Ph.D. Prof. Mark Asta and Prof. David Limmer have also been helping me with my Ph.D. dissertation, and I am grateful for their support throughout my Ph.D. I would also like to thank my GSI advisor, Prof. Phillip Messersmith, for teaching me how to pass on my knowledge to younger students. During my research, I also worked closely with Prof. Xiaoyu (Rayne) Zheng and Prof. Feng Wang. Their expertise in 3D printing and PL characterizations, respectively, had helped me greatly advance my projects. They broadened my expertise, and I am forever grateful.

Furthermore, I would like to thank my fellow group members in the Yang group. They are not only my colleagues, but also my friends. I would like to give special thanks to Lissette Garcia and Crystal Garcia, who serve as group administrators, for all their assistance in my daily research and life. I would like to thank my closest collaborator, Dr. Jianbo Jin, for all the scientific discussions and all the experiments we have done together. I would like to thank Dr. Mengyu Gao for being my mentor when I joined the group. I would also like to thank my colleagues in the perovskite/nanowire subgroup for all the help and support: Heqing Zhu, Yuxin Jiang, Han K. D. Le, Alex M. Oddo, Dr. Maria C. Folgueras, Lior Verbitsky, Dr. Chung-Kuan Lin, Dr. Ye Zhang, Dr. Zhenni Lin, Dr. Lina Quan, and Emily Lu. I also had the great privilege to work with members from the other subteams: Dr. Jie Luo, Jia-An Lin, Maria F. Guzman, Lihini Jayasinghe, Dr. Sheena Louisia, and Dr. Ji Min Kim. I am thankful for all their support. I hope I can stay in touch with all of them and wish them all the best in their future endeavors.

I could not complete my Ph.D. without the help from people outside the Yang group. I would like to thank Dr. Zhen Wang and Dr. Zhenpeng Xu from Prof. Rayne Zheng's group for the immense help in my project. They always considered our collaboration the highest priority, and I am very grateful for their selfish support. Also, I would like to thank Can B. Uzundal from Prof. Feng Wang's group, who also helped me tremendously with my project. I would also like to express my gratitude for the people who helped me with various measurements: Dr. Nicholas Settineri at CheXray, Dr. Chang Yan from Prof. Paul Alivisatos's group, Dr. Katherine Armstrong from LBL, and Dr. Juliet Jamtgaard from Stanford University.

Last but not least, I would like to give special thanks to my family. I would like to express my sincerest gratitude to my parents and grandparents. Although they were not in the same country, but they have supported me in so many ways, and they are the reason why I never give up. I would also like to thank my fiancée Honglin Zheng for the unwavering support and love over the years. I shared all my ups and downs with her, and she offered so much emotional support.

Chapter 1 Background of Halide Perovskites

1.1 Fundamentals of Halide Perovskites

1.1.1 A New Ionic Semiconductor

Despite the long history tracing back to Gustav Rose's discovery of the oxide perovskite structure calcium titanate ($CaTiO_3$) in the Ural Mountains over 150 years ago, it is only in recent years that analogous halide perovskites have been optimized for practical applications. Halide perovskites have surged in popularity due to their cost-effective synthesis methods, facile fabrication processes, tunable color emissions, high photoluminescence quantum yields (PLQYs), and remarkable excitonic and charge carrier properties[1]. These advantageous characteristics render halide perovskites highly suitable for the construction of various electronic devices, including light-emitting diodes (LEDs), lasers, photodetectors, and solar cells.

Halide perovskites, characterized by their crystalline structure denoted as ABX_3, have received significant research attention in recent years. In this structure, A and B represent cations, with A being larger than B, while X signifies the anion (**Figure 1.1**). This arrangement maintains fixed positions for each constituent, resulting in a three-dimensional framework typified by a corner-sharing octahedral network. Specifically, the B cations are coordinated by X anions to form BX_6 octahedra, while the A cations are positioned at the eight corners of the cubic lattice (**Figure 1.1**)[2,3]. The ABX_3 structure has a variety of compositions. The A-site cation could be Cs^+, methylammonium ($CH_3NH_3^+$), or formamidinium [$(CH(NH)_2)^{2+}$], and occupies the interstitial spaces formed by the corner-sharing BX_6 octahedra. Moreover, the ABX_3 structure has orthorhombic and tetragonal crystal symmetries as well (**Figure 1.2a**). Variations in halide perovskites are achieved by altering the A- or B-site cations, such as Pb^{2+}, Sn^{2+}, and Ge^{2+}, along with the halide ion (X = Cl, Br, I) (**Figure 1.2b**)[4].

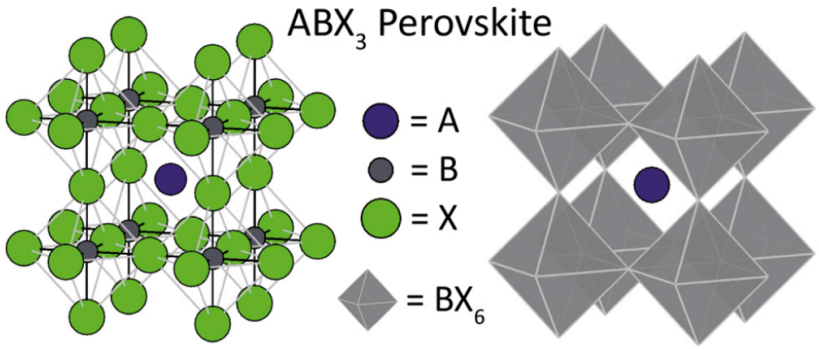

Figure 1.1. Depiction of the cubic halide perovskite structure. Shown in display styles evidencing either all the atoms (left) or only the BX_6 octahedral network and A atoms (right).[2] Copyright © 2020 American Chemical Society.

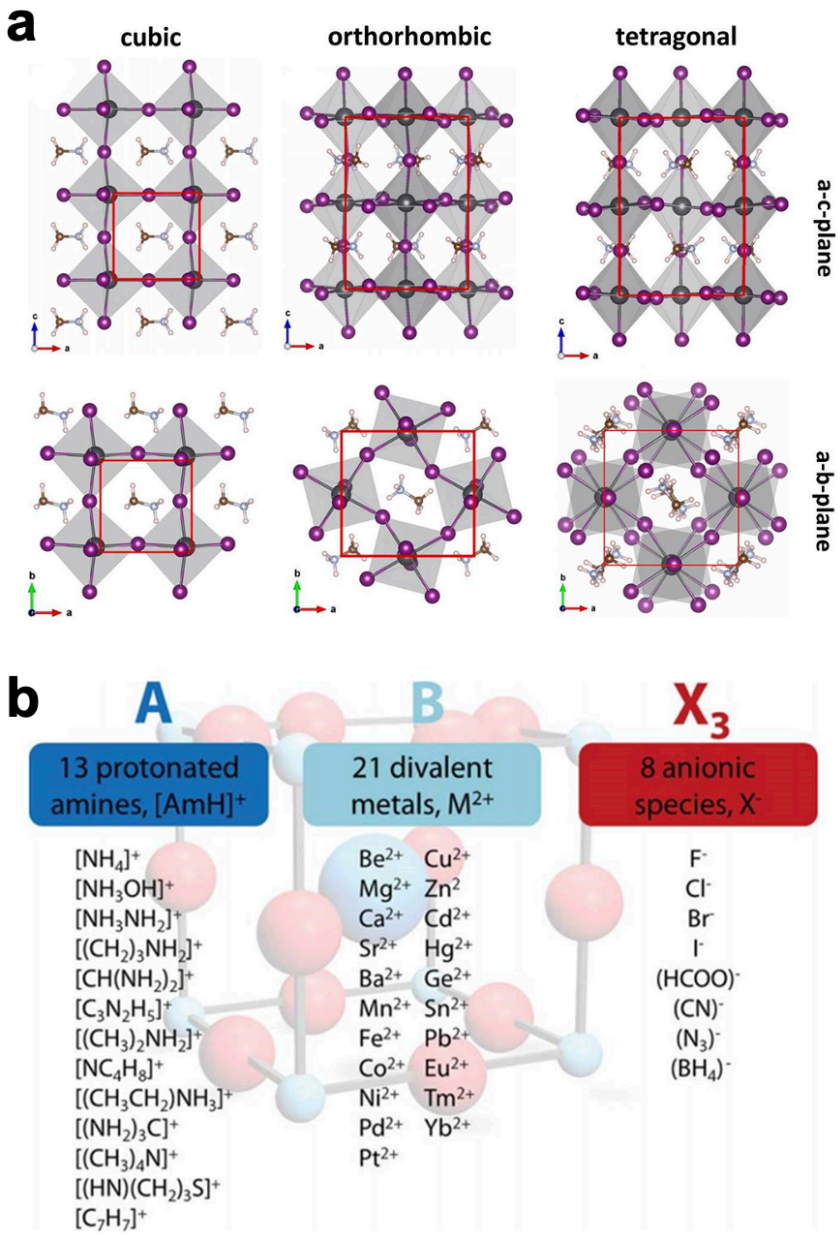

Figure 1.2. (a) Comparison of cubic, orthorhombic and tetragonal perovskite phases for the prototype ABX_3 perovskite. (b) Choice of site substituents for perovskite.[4] Copyright © 2019 Elsevier Ltd.

Halide perovskites are significantly different from conventional covalent bonded semiconductors like silicon[5]. They have remarkably lower cohesive energy. While traditional semiconductors boast cohesive energies exceeding 4 eV/atom, halide perovskites exhibit substantially lower values, exemplified by 3.40 eV per atom for bulk $CsPbI_3$[6]. This discrepancy arises from the distinctive ionic chemical bonding characteristics and the presence of stereochemically active ns^2 lone pair electrons in Pb^{2+} and Sn^{2+} cations within the perovskite lattice. Consequently, the ionic nature of the perovskite lattice renders reduced mechanical

strength, a lower melting point, and enhanced solution processability. This ionic lattice structure also facilitates a rich structural diversity and chemistry, enabling facile synthesis and diverse applications. Furthermore, the ionic nature of halide perovskite structures allows for unique physical phenomena such as lattice dynamics, structural transformations, and facile hybridization with organic molecules. This stands in stark contrast to the rigid, covalent-bonded lattice typical of traditional semiconductors, highlighting the distinctive reconfigurable nature of halide perovskite[7] (**Table 1.1**).

Table 1.1. Comparative study of the structural properties of conventional semiconductors and halide perovskites.[7] Copyright © 2021, Elsevier Inc.

	Conventional semiconductors	**Halide perovskites**
Bonding type	covalent, ionic	ionic
Cohesive energy	>4 eV/atom	3 eV/atom
Melting point	above 1000℃	below 600℃
Solubility	insoluble in solvents	soluble in polar solvents
Synthesis temperature	mostly above 1000℃	mostly below 150℃
Growth kinetics	slow	fast even at low temperature
Incorporation with organic components	only on the surface (nanocrystals)	in the lattice (hybrid or 2D perovskite) or on the surface (nanocrystals)

1.1.2 Optoelectronic Properties of Halide Perovskites

Halide perovskites have received immense interest in the field of optoelectronics due to their exceptional properties. These materials exhibit high PLQYs, broad absorption spectra covering the visible and near-infrared regions, and long carrier diffusion lengths, making them highly efficient light absorbers and emitters. Additionally, halide perovskites demonstrate excellent charge carrier mobility, low trap densities, and long carrier lifetimes, facilitating efficient charge transport and collection. Their defect tolerance and tunable bandgap enable the engineering of optoelectronic devices with tailored optical and electronic properties[8].

(1) Tunable absorption and emission.

Halide perovskites offer tunable absorption and emission properties, which are highly advantageous for various optoelectronic applications. One key aspect of their tunability lies in the ability to precisely control their bandgap by adjusting the composition of the material[9]. This compositional flexibility allows the fine-tuning of the absorption spectrum of halide perovskites across a broad range of wavelengths, spanning from the ultraviolet to the near-infrared region (**Figure 1.3a**). Consequently, halide perovskites can efficiently absorb photons across a wide range of energies, making them suitable for harvesting solar radiation in photovoltaic devices. Moreover, the emission spectrum of halide perovskites can also be tailored to match specific application requirements (**Figure 1.3b, c**). By varying factors such as the halide composition, crystal size, or surface ligands, the emission color of these materials

can be manipulated[10], making halide perovskites promising candidates for light-emitting diodes (LEDs) and other display technologies.

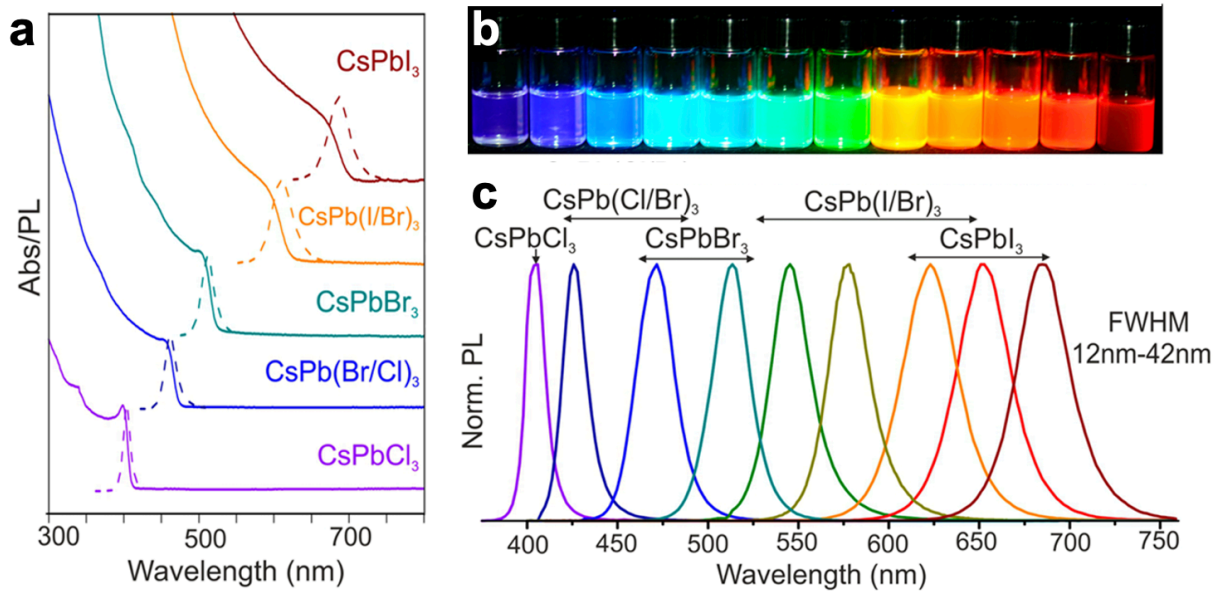

Figure 1.3. Tunable absorption and emission of halide perovskites covering the entire visible spectral region. (a) Typical optical absorption and PL spectra of colloidal $CsPbX_3$ NCs (X = Cl, Br, I) (b) Colloidal $CsPbX_3$ NCs solutions in toluene under UV lamp (λ = 365 nm). (c) Representative PL spectra (λ_{exc} = 400 nm for all but 350 nm for $CsPbCl_3$ samples).[10] Copyright © 2015, American Chemical Society.

(2) High PLQY.

The high PLQY exhibited by halide perovskites is a key factor contributing to their exceptional performance in optoelectronic devices. PLQY refers to the efficiency with which a material converts absorbed photons into emitted photons upon photoexcitation. Several factors contribute to this high PLQY, which is a result of their low defect densities, favorable electronic structure, and high crystalline quality. These factors minimize non-radiative recombination processes, ensuring that a large proportion of photoexcited carriers undergo radiative recombination, emitting photons efficiently[11]. Additionally, the direct bandgap nature and strong quantum confinement effect of halide perovskites further enhance radiative transitions, contributing to high PLQY values exceeding 90% in many cases[12]. Overall, these characteristics make halide perovskites highly attractive for optoelectronic applications, including photovoltaics, LEDs, lasers, and photodetectors.

(3) Efficient charge transport and collection.

Halide perovskites exhibit remarkable characteristics related to charge carrier dynamics, which are crucial for their performance in optoelectronic devices. Firstly, they display excellent charge carrier mobility, indicating that the charge carriers (electrons and holes) can move easily through the crystal lattice. This high mobility ensures rapid transport of charges within the material, minimizing losses and enhancing device efficiency. Secondly, halide perovskites have

low trap densities and shallow trap states, meaning there are relatively few defects or imperfections in the crystal structure that can capture and immobilize charge carriers (**Figure 1.4**). Low trap densities reduce recombination rates, allowing more charges to reach the device's electrodes and contribute to electrical output. Finally, halide perovskites possess long carrier lifetimes, meaning that once generated by light absorption, the charges persist in the material for extended periods before recombining. This prolonged lifetime increases the likelihood of charge extraction and utilization in devices, resulting in improved performance and stability. Collectively, these characteristics facilitate efficient charge transport and collection in halide perovskites, making them highly promising materials for a wide range of optoelectronic applications[13].

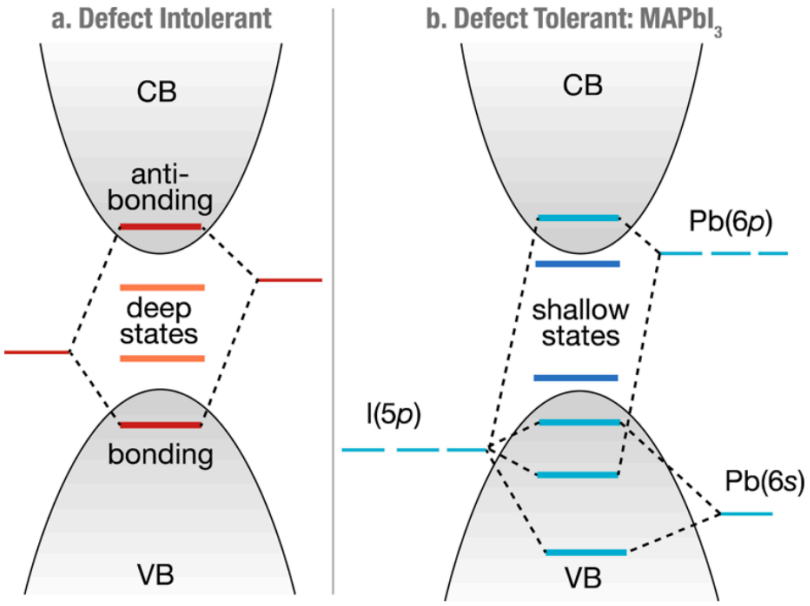

Figure 1.4. Electronic structure of typical III−V, II−VI, or group IV semiconductors (left) compared to the lead halide perovskite crystal structure (right).[13] Copyright © 2017 American Chemical Society.

1.1.3 Synthesis of Halide Perovskites

As discussed in **Chapter 1.1.1**, halide perovskites feature facile low-temperature solution-based synthesis with fast growth kinetics. This allows for the synthesis of single crystals of halide perovskites, which can be used for structural determination of the synthesized materials. The single-crystal growth involves employing various solution-based techniques, with the solvent evaporation crystallization method being a traditional and straightforward approach under ambient conditions. This method entails preparing a solution by mixing reactants in a solvent, which subsequently undergoes evaporation, resulting in crystal growth[14] (**Figure 1.5a**). To achieve optimal crystallization, the choice of solvents with moderate solubility is crucial, as oversaturation can lead to the formation of extremely small crystals. Additionally, the antisolvent vapor-assisted crystallization process offers another route for single crystal

synthesis, depending on the different solubility of perovskites in various solvents. By applying two miscible solvents, one serving as the main solvent and the other as the antisolvent, the solubility of the perovskite precursors decreases upon addition of the antisolvent, facilitating precipitation[14] (**Figure 1.5b**). The speed at which the antisolvent is introduced is a critical factor influencing the crystal quality and size.

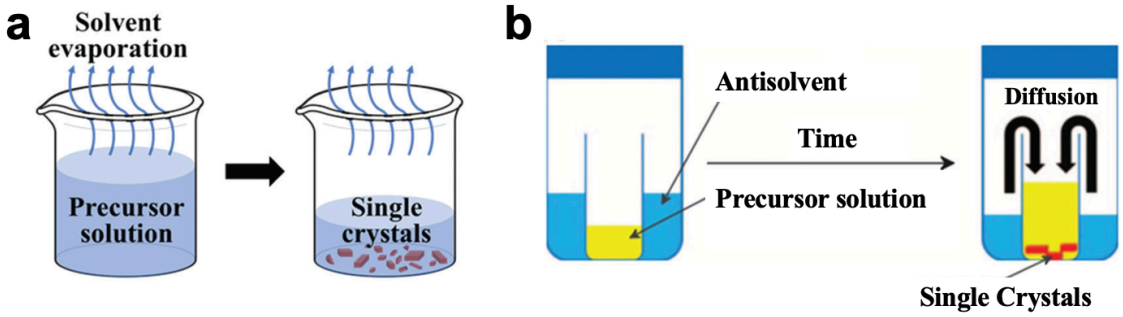

Figure 1.5. Schematics of the single crystal growth of halide perovskites. (a) The solvent evaporation crystallization method. (b) The antisolvent vapor-assisted crystallization method.[14] Copyright © The Royal Society of Chemistry 2022.

Halide perovskite can also be synthesized in the form of thin films. It represents a significant advancement in low-temperature solution-processed semiconductors, offering a promising avenue for the fabrication of semiconductor materials. These materials can be readily processed in ink form through wet chemistry methods. Notably, they enable large-area deposition from solution using standard manufacturing techniques like spin coating, roll-to-roll printing, spray coating, and doctor blading[15] (**Figure 1.6**). This versatility in deposition methods allows for scalability and cost-effectiveness in production processes. Moreover, the synthesis of halide perovskite thin films occurs at low temperatures and under ambient conditions, further enhancing their appeal for practical applications. These characteristics collectively contribute to the growing interest in halide perovskite thin films as versatile and efficient materials for various optoelectronic devices.

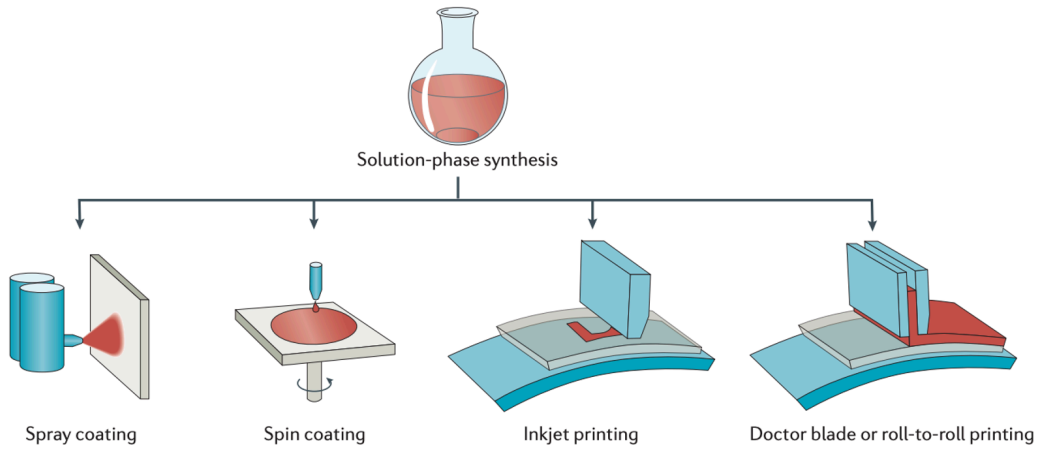

Figure 1.6. Solution-processed halide perovskite thin films are synthesized in the form of semiconductor inks. They can be deposited using spray coating or spin coating, or manufacturing techniques such as inkjet printing, doctor blading or roll-to-roll printing.[15] Copyright © 2017, Macmillan Publishers Limited, part of Springer Nature.

1.2 Structural Tunability of Halide Perovskites

1.2.1 Morphological Dimensionality

The morphological dimension of halide perovskites can be precisely adjusted, ranging from single crystals measuring centimeters to nanocrystals only a few nanometers in size, thus significantly enhancing their versatility. The ability to adjust the bandgap is a crucial property of semiconductor nanocrystals, leveraging the quantum confinement effect on excitons[16]. Halide perovskite nanocrystals are synthesized through methods like hot-injection or ligand-assisted reprecipitation (LARP) (**Figure 1.7**), enabling precise control over size and morphology. Long-chain organic ligands, such as aliphatic carboxylic acids and amines, are used for surface capping, confining crystal growth to the nanometer scale. The hot-injection method involves dissolving precursors like cesium acetate and oleic acid in hexadecene, which are then injected into a solution of lead bromide and capping ligands at elevated temperatures. Conversely, $FAPbBr_3$ nanocrystals are synthesized at lower temperatures by injecting a solution of octadecylammonium bromide into a mixture of lead acetate, formamidinium acetate, and oleic acid in octadecene[16]. The reaction is quenched promptly, and nanocrystals are collected via centrifugation or purification. Alternatively, the LARP method offers room temperature synthesis convenience for perovskite nanocrystals[17].

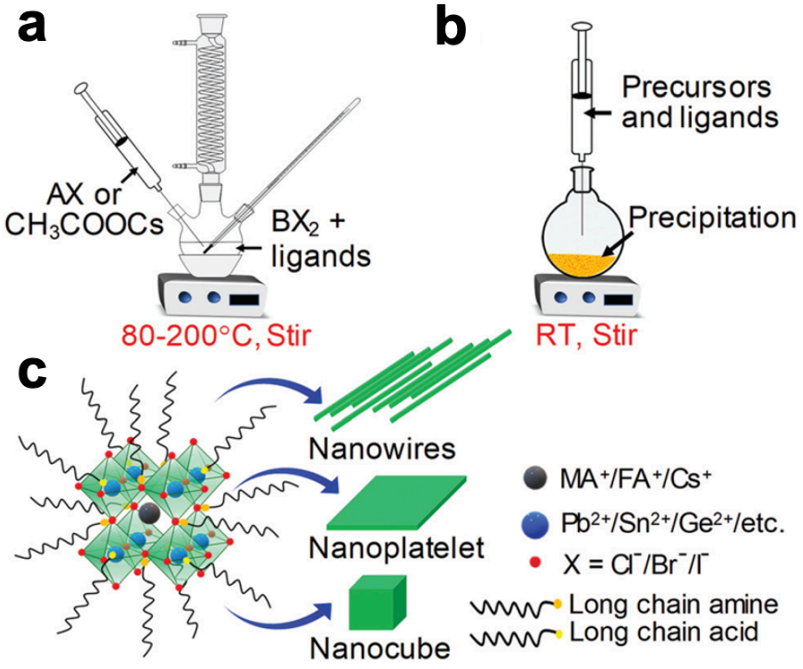

Figure 1.7. Synthesis of perovskite nanocrystals. (a) Hot injection method, and (b) LARP method. (c) Ligand-capped nanocrystals of perovskites with different morphologies.[17] Copyright © The Royal Society of Chemistry 2020.

1.2.2 Electronic Dimensionality

In halide perovskites, the connectivity of the halide octahedra determines the electronic dimensionality of the materials. Their electronic dimensionalities greatly influence the bandgap values and the band dispersion in perovskite materials. To elucidate the impact of electronic dimensionalities on the optical properties of perovskite materials, Density Functional Theory (DFT) calculations on the band structures are done for prototype perovskite materials[18]. These materials consist of the same elements: Cs, Pb, and I, yet exhibit different crystal dimensionalities. Specifically, 3D $CsPbI_3$ (cubic), 2D Cs_2PbI_4 (tetragonal), 1D Cs_3PbI_5 (orthorhombic), and 0D Cs_4PbI_6 (rhombohedral). These structures encompass 3D networks, 2D single layers, 1D single chains of [PbI_6] octahedra, and isolated [PbI_6] octahedra, respectively (**Figure 1.8a**). **Figure 1.8b** depicts the calculated band structures. As the electronic dimensionality decreases, the bandgap becomes larger, and the bands are less dispersive. Also, the 3D and 2D structures have direct bandgaps, while the 1D and 0D versions have indirect band gaps.

The presence of electronic dimensionality offers a broad space to explore the structure-property relationship of halide perovskites. Apart from the all-inorganic halide perovskites, various organic cations can also be incorporated into the structure, achieving organic-inorganic hybrid perovskites with diverse electronic dimensionalities. By substituting Cs^+ with larger organic cations, an array of low-dimensional metal halide hybrids can be generated, encompassing layered 2D, linear 1D, and 0D connected octahedra configurations (**Figure 1.9b**).

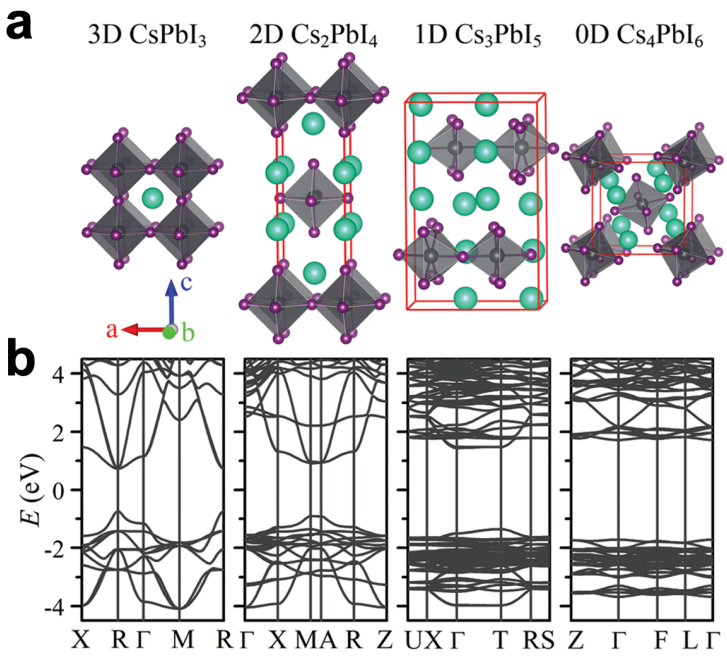

Figure 1.8. Electronic dimensionality of halide perovskites. (a) Hypothetical model crystal structures of $CsPbI_3$, Cs_2PbI_4, Cs_3PbI_5, and Cs_4PbI_6. (b) Calculated band structures.[18] Copyright © The Royal Society of Chemistry 2017.

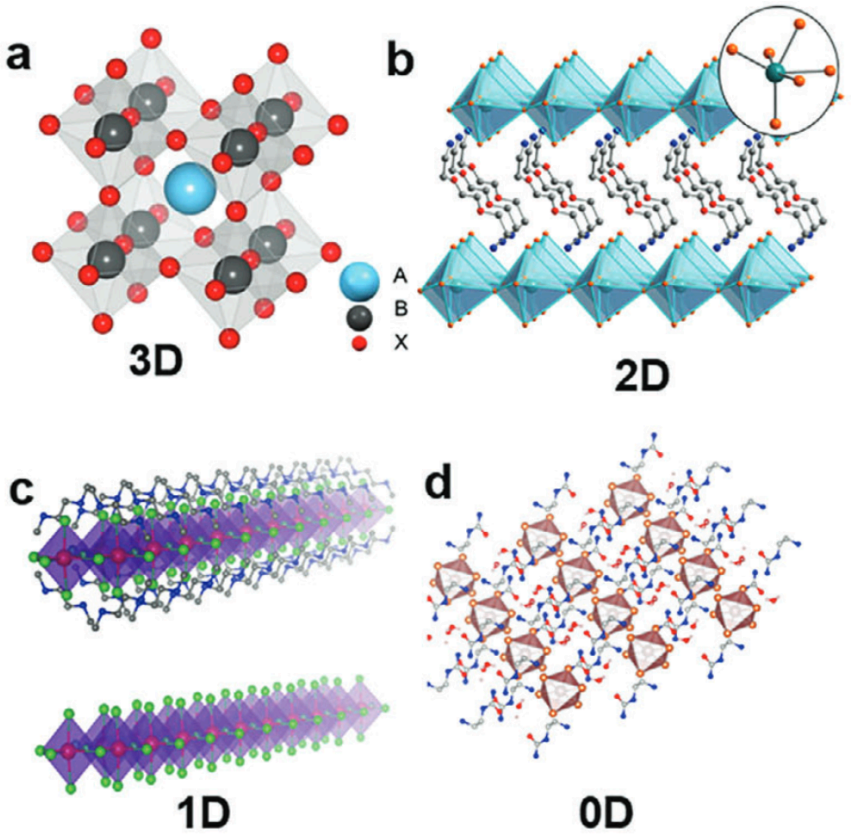

Figure 1.9. Typical single crystal structures of 0D-3D organic-inorganic hybrid perovskites.[19] Copyright © 2021 The Authors. Advanced Science published by Wiley-VCH GmbH.

1.3 Halide Perovskite Building Blocks

1.3.1 Ionic Octahedron Building Blocks

As elucidated in **Chapter 1.2.2**, the interconnectivity and spatial arrangement of $[BX_6]^{n-}$ halide octahedra play a pivotal role in shaping the optical properties of halide perovskites. This underscores the foundational significance of ionic octahedra in the construction of these materials. The lattice configuration of ABX_3 halide perovskites emerges from the intricate corner-sharing pattern exhibited by $[BX_6]^{4-}$ ionic octahedra. This structural framework has evolved to encompass a diverse array of materials derived from the $[BX_6]^{n-}$ ionic octahedral building blocks, showcasing various dimensionalities (including 3D, 2D, 1D, and 0D), connection modes (such as corner-sharing, edge-sharing, and face-sharing), and a spectrum of charges attributed to the central B^{n+} ions, which span oxidation states ranging from +1 to +5.

This diversity underscores the rich potential and versatility inherent in halide perovskite materials, offering a broad spectrum of applications across multiple disciplines.

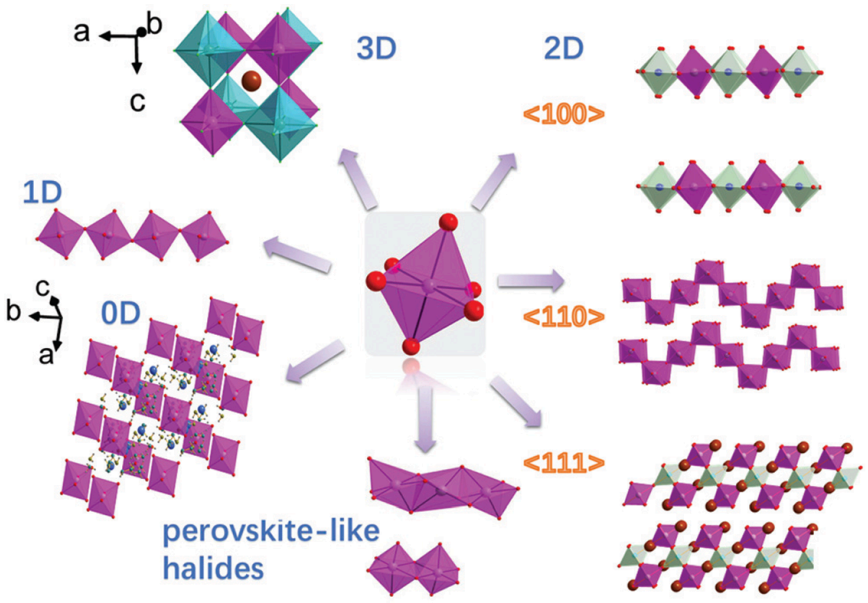

Figure 1.10. Halide perovskite structures constructed from metal halide ionic octahedral building blocks in 3D, 2D, 1D, and 0D.[20] Copyright © 2019, Royal Society of Chemistry.

1.3.2 Stabilization of the Halide Perovskite Building Blocks

By carefully manipulating the halide perovskite building blocks, we open up a new perspective for the rational design of novel perovskite structures. The first step in this endeavor involves the stabilization of these building blocks within solution to enable the bottom-up synthetic approach. Through solution stabilization, we gain the ability to exert precise control over the arrangement of the perovskite building blocks, enabling us to tailor their properties. This foundational manipulation paves the way for a systematic exploration of the vast design space of halide perovskites.

Our group recently discovered that a stable halide perovskite building block ink can be formed in solution[21]. This ink is created through the dissolution of vacancy-ordered double perovskite Cs_2TeX_6 ($X = Cl^-, Br^-, I^-$) crystals in polar aprotic solvents. This dissolution process leads to the stabilization of isolated $[TeX_6]^{2-}$ octahedral building blocks and free Cs^+ cations (**Figure 1.11**). By stabilizing the fundamental perovskite ionic octahedral building blocks in solution, multifunctional inks are formed, capable of reversible transformation between liquid ink and solid-state perovskite crystalline systems within minutes in ambient air.

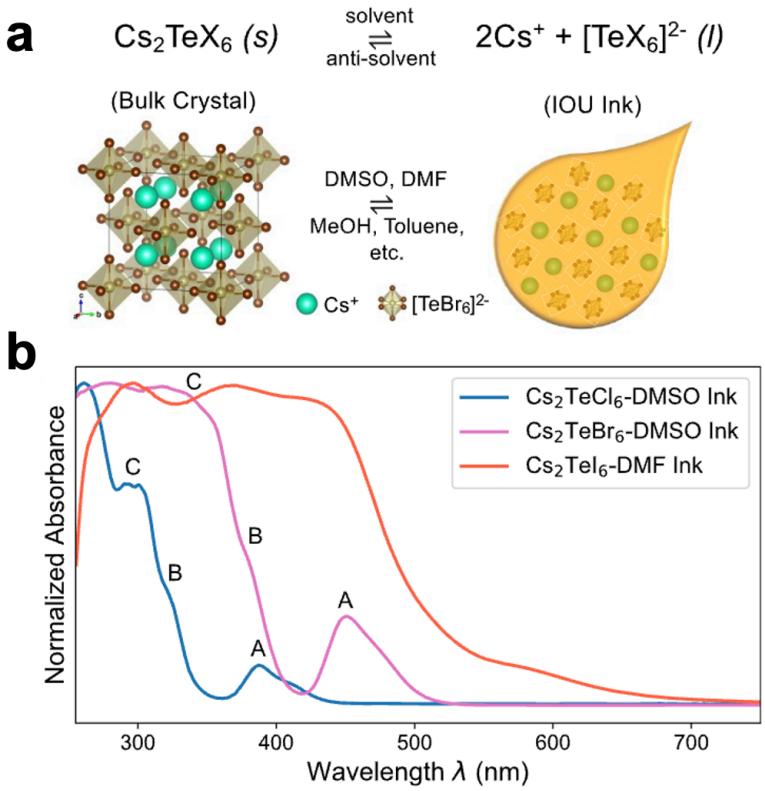

Figure 1.11. Stabilization of the halide perovskite building blocks in solution. (a) Schematic representation of the reversible reaction between the solid-state Cs_2TeX_6 bulk semiconductor and the liquid-phase Cs_2TeX_6 ionic octahedron unit (IOU) ink. The IOU ink is achieved by dissociating the bulk semiconductor in solvents such as DMSO or DMF, and the bulk semiconductor is reprecipitated by combining the IOU ink with an antisolvent such as methanol, toluene, etc. (b) Absorption spectra of the Cs_2TeCl_6-DMSO, Cs_2TeBr_6-DMSO, and Cs_2TeI_6-DMF inks. The characteristic absorbance features of molecular octahedral complexes (A, B, and C bands) are indicated for the Cs_2TeCl_6 and Cs_2TeBr_6 inks.[21] Copyright © 2021, American Chemical Society.

1.3.3 Assembly of the Halide Perovskite Building Blocks

The next stage for the manipulation of halide perovskite building blocks would be the assembly of them into a crystal structure. Since they can be stabilized in solution, our focus has shifted towards exploring the packing and interconnectivity of the building blocks, aiming to uncover novel varieties of halide perovskites. In this pursuit, we regard the ionic $[BX_6]$ octahedron as a superion or atom. Much like how diverse atoms and ions can assemble to create various crystal lattices, these ionic $[MX_6]$ octahedra possess the potential to organize into distinct types of negatively charged, extended ionic octahedral networks (IONs), both with and without corner sharing. Eventually, the crystalline structures of halide perovskites emerge when these negatively charged IONs are stabilized by counter cations[22] (**Figure 1.12**). This approach offers a novel perspective for the systematic exploration of halide perovskite structures, paving the way for the discovery of novel materials with tailored properties.

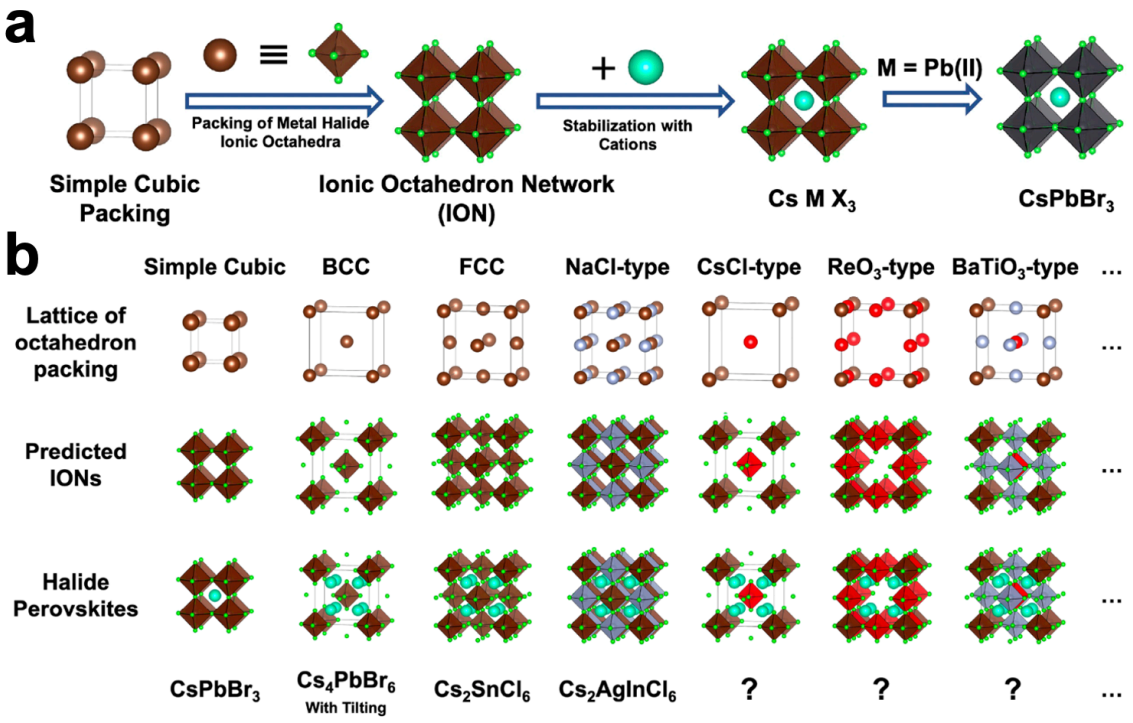

Figure 1.12. Schematic of the ionic octahedron network (ION). (a) Metal halide perovskites can be considered as extended ionic octahedron networks (IONs) stabilized with positively charged cations. (b) Seven different lattices of octahedron packing and the predicted IONs and metal halide perovskite structures.[22] Copyright © 2021, American Chemical Society.

1.4 Applications of Halide Perovskites

Halide perovskites have garnered significant attention in recent years due to their diverse range of potential applications across various fields.

(1) Solar cells

One prominent application lies in photovoltaics, where halide perovskite solar cells have emerged as promising alternatives to traditional silicon-based solar cells. Their high absorption coefficients, long carrier diffusion lengths, and tunable bandgaps make them suitable for efficient light harvesting. Moreover, their low-cost fabrication methods, including solution processing, offer scalability and affordability, paving the way for widespread adoption in renewable energy systems. In terms of power conversion efficiency (PCE), halide perovskites have achieved 25.7% in 2021 for single-junction architectures[23], and up to 29.8% in silicon-based tandem cells[24], surpassing the maximum efficiency of single-junction silicon solar cells. However, the stability of those materials and the large-scale device fabrication of these materials still have room for improvement[25].

(2) Light-emitting devices

Halide perovskites also exhibit remarkable properties in light-emitting devices. Their high PLQY, narrow emission linewidths, and tunable emission wavelengths make them attractive

candidates for light-emitting diodes (LEDs), displays, and solid-state lighting applications. Halide perovskite LEDs have already reached high external quantum efficiencies (EQE) of different color LEDs: 18.65% for blue[26], 28.9% for green[27], and 25.8% for red[28]. Researchers continue to explore methods to enhance the stability and efficiency of perovskite-based LEDs, aiming for commercial viability in the future.

(3) Photodetectors

Halide perovskites also hold promise in the field of photodetectors. They are highly sensitive to light across a broad spectral range, from UV-visible and near-infrared (NIR) light to high-energy radiations like X-ray and gamma-ray[29]. They also have fast response times, making them suitable for applications in imaging and sensing devices. Additionally, their solution processability enables the fabrication of large-area and flexible photodetector arrays, opening up opportunities for applications in wearable technology, biomedical imaging, and environmental monitoring.

(4) Catalysis

Furthermore, halide perovskites have demonstrated potential in catalysis, particularly in the field of photocatalysis for water splitting[30] and carbon dioxide reduction[31]. Their ability to efficiently absorb sunlight and generate charge carriers makes them effective photocatalysts for driving chemical reactions. By harnessing the unique properties of halide perovskites, researchers aim to develop sustainable energy conversion technologies and mitigate environmental challenges associated with fossil fuel consumption.

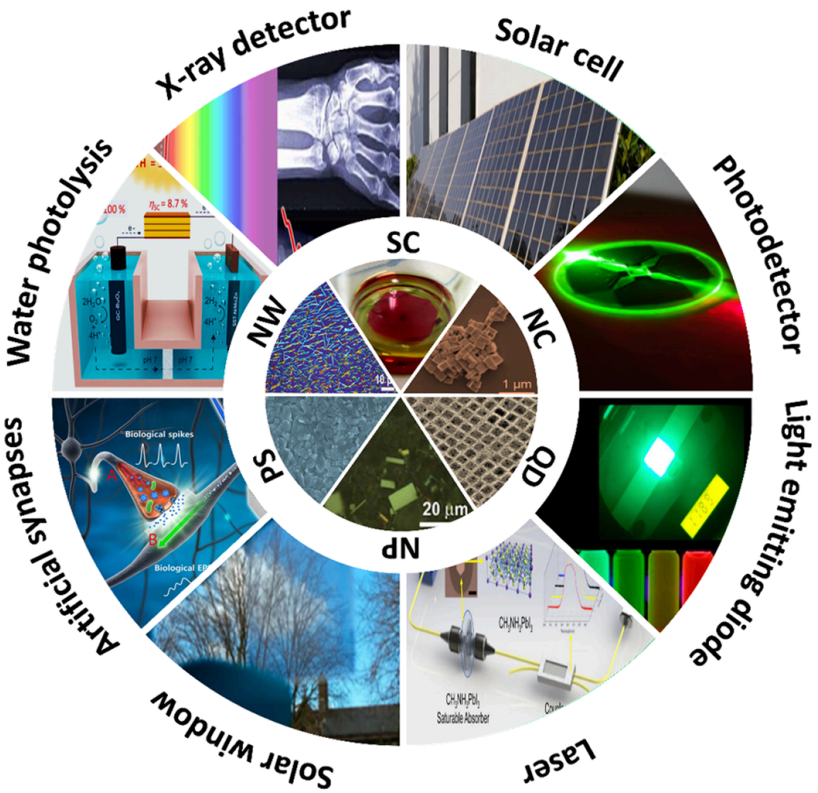

Figure 1.13. Schematic depiction of perovskite materials in different forms and their potential applications. (Acronyms: SC: single crystal, NC: nanocrystal, QD: quantum dot, NP: nano-plate, PS: polycrystal, NW: nanowire). [4] Copyright © 2019 Elsevier Ltd.

1.5 References

[1] A. R. B. M. Yusoff, M. K. Nazeeruddin, Organohalide lead perovskites for photovoltaic applications. J. Phys. Chem. Lett., 7, 851 (2016). doi: 10.1021/acs.jpclett.5b02893

[2] Q. A. Akkerman, L. Manna, What Defines a Halide Perovskite? ACS Energy Lett., 5 (2), 604–610 (2020). doi: 10.1021/acsenergylett.0c00039

[3] S. A. Veldhuis, P. P. Boix, N. Yantara, M. Li, T. C. Sum, N. Mathews, S. G. Mhaisalkar, Perovskite materials for light-emitting diodes and lasers. Adv. Mater., 28, 6804 (2016). doi: 10.1002/adma.201600669

[4] K. Wang, D. Yang, C. Wu, M. Sanghadasa, S. Priya, Recent progress in fundamental understanding of halide perovskite semiconductors. Prog. Mater. Sci. 106, 100580 (2019). doi: 10.1016/j.pmatsci.2019.100580

[5] V. Dolocan, A. Dolocan, V. O. Dolocan, Relation of inter-atomic forces in solids to bulk modulus, cohesive energy and thermal expansion. Mod. Phys. Lett. B, 22 (25), 2481–2492 (2008). doi: 10.1142/S0217984908017096

[6] S. Ozen, F. Iyikanat, M. Ozcan, G. E. Tekneci, I. Eren, Y. Sozen, H. Sahin, Orthorhombic CsPbI3 perovskites: thickness-dependent structural, optical and vibrational properties. Comput. Condens. Matter, 23, e00453 (2020). doi: 10.1016/j.cocom.2019.e00453

[7] M. Gao, Y. Zhang, Z. Lin, J. Jin, M. C. Folgueras, P. Yang, The Making of a Reconfigurable Semiconductor with a Soft Ionic Lattice. Matter, 4 (12), 3874–3896 (2021). doi: 10.1016/j.matt.2021.09.023

[8] J. S. Manser, J. A. Christians, P. V. Kamat, Intriguing Optoelectronic Properties of Metal Halide Perovskites. Chem. Rev., 116, 21, 12956–13008 (2016). doi: 10.1021/acs.chemrev.6b00136

[9] Q. A. Akkerman, G. Rainò, M. V. Kovalenko, L. Manna, Genesis, challenges and opportunities for colloidal lead halide perovskite nanocrystals. Nat. Mater. 17, 394–405 (2018). doi: 10.1038/s41563-018-0018-4

[10] L. Protesescu, S. Yakunin, M. I. Bodnarchuk, F. Krieg, R. Caputo, C. H. Hendon, R. X. Yang, A. Walsh, M. V. Kovalenko, Nanocrystals of Cesium Lead Halide Perovskites ($CsPbX_3$, X = Cl, Br, and I): Novel Optoelectronic Materials Showing Bright Emission with Wide Color Gamut. Nano Lett., 15, 3692−3696 (2015). doi: 10.1021/nl5048779

[11] F. D. Stasio, S. Christodoulou, N. Huo, G. Konstantatos, Near-unity photoluminescence quantum yield in CsPbBr3 nanocrystal solid-state films via postsynthesis treatment with lead bromide. Chem. Mater., 29 (18), 7663–7667 (2017). doi: 10.1021/acs.chemmater.7b02834

[12] Hanifi, D. A. et al. Redefining near-unity luminescence in quantum dots with photothermal threshold quantum yield. Science, 363, 6432, 1199–1202 (2019). doi: 10.1126/science.aat3803

[13] R. E. Brandt, J. R. Poindexter, P. Gorai, R. C. Kurchin, R. L. Z. Hoye, L. Nienhaus, M. W. B. Wilson, J. A. Polizzotti, R. Sereika, R. Zaltauskas, L. C. Lee, J. L. MacManus-Driscoll, M. Bawendi, V. Stevanovic, T. Buonassisi, Searching for "Defect-Tolerant" Photovoltaic Materials: Combined Theoretical and Experimental Screening. Chem. Mater., 29, 11, 4667–4674 (2017). doi: 10.1021/acs.chemmater.6b05496

[14] Y. Cho, H. R. Jung, W. Jo, Halide perovskite single crystals: growth, characterization, and stability for optoelectronic applications. Nanoscale, 14, 9248 (2022). doi: 10.1039/d2nr00513a

[15] F. P. García de Arquer, A. Armin, P. Meredith, E. H. Sargent, Solution-processed semiconductors for next-generation photodetectors. Nat. Rev. Mater., 2, 16100 (2017). doi: 10.1038/natrevmats.2016.100

[16] I. Moreels, K. Lambert, D. Smeets, D. De Muynck, T. Nollet, J. C. Martins, F. Vanhaecke, A. Vantomme, C. Delerue, G. Allan, Z. Hens, Size-dependent optical properties of colloidal PbS quantum dots. ACS Nano, 3, 3023−3030 (2009). doi: 10.1021/nn900863a

[17] L. Chouhan, S. Ghimire, C. Subrahmanyam, T. Miyasaka, V. Biju, Synthesis, optoelectronic properties and applications of halide perovskites. Chem. Soc. Rev., 49, 2869 (2020). doi: 10.1039/c9cs00848a

[18] Z. Xiao, W. Meng, J. Wang, D. B. Mitzi, Y. Yan, Searching for promising new perovskite-based photovoltaic absorbers: the importance of electronic dimensionality. Mater. Horiz., 4, 206 (2017). doi: 10.1039/c6mh00519e

[19] Y. Han, S. Yue, B.-B. Cui. Low-dimensional metal halide perovskite crystal materials: structure strategies and luminescence applications. Adv. Sci., 8, 2004805 (2021). doi: 10.1002/advs.202004805

[20] Z. Song, J. Zhao, Q. Liu, Luminescent perovskites: recent advances in theory and experiments. Inorg. Chem. Front., 6, 2969-3011 (2019). doi: 10.1039/C9QI00777F

[21] M. C. Folgueras, S. Louisia, J. Jin, M. Gao, A. Du, S. C. Fakra, R. Zhang, F. Seeler, K. Schierle-Arndt, P. Yang, Ligand-free processable perovskite semiconductor ink. Nano Lett., 21 (20), 8856−8862 (2021). doi: 10.1021/acs.nanolett.1c03308

[22] J. Jin, M. C. Folgueras, M. Gao, S. Yu, S. Louisia, Y. Zhang, L. N. Quan, C. Chen, R. Zhang, F. Seeler, K. Schierle-Arndt, P. Yang. A new perspective and design principle for halide perovskites: ionic octahedron network (ION). Nano Lett., 21(12), 5415−5421 (2021). doi: 10.1021/acs.nanolett.1c01897

[23] H. Min et al. Perovskite solar cells with atomically coherent interlayers on SnO_2 electrodes. Nature, 598, 7881, 444–450 (2021). doi: 10.1038/s41586-021-03964-8

[24] NREL. Best Research-cell Efficiency Chart. www.nrel.gov/pv/cell-efficiency.html.

[25] J. Tian, Q. Xue, Q. Yao, N. Li, C. J. Brabec, H.-L. Yip, Inorganic halide perovskite solar cells: progress and challenges. Adv. Energy Mater., 10, 23, 2000183 (2020). doi: 10.1002/aenm.202000183

[26] W. Zhou, Y. Shen, L.-X. Cao, Y. Lu, Y.-Y. Tang, K. Zhang, H. Ren, F.-M. Xie, Y.-Q. Li, J.-X. Tang, Manipulating ionic behavior with bifunctional additives for efficient sky-blue perovskite light-emitting diodes. Adv. Funct. Mater., 2301425 (2023). doi: 10.1002/adfm.202301425

[27] J. S. Kim, et al Ultra-bright, efficient and stable perovskite light-emitting diodes. Nature, 611, 7937, 688–694 (2022). doi: 10.1038/s41586-022-05304-w

[28] J. Jiang, Z. Chu, Z. Yin, J. Li, Y. Yang, J. Chen, J. Wu, J. You, X. Zhan, Red perovskite light-emitting diodes with efficiency exceeding 25% realized by co-spacer cations. Adv. Mater., 34, 36, 2204460 (2022). doi: 10.1002/adma.202204460

[29] H. Wu, Y. Ge, G. Niu, J. Tang. Metal halide perovskites for X-ray detection and imaging. Matter, 4, 1, 144–163 (2021). doi: 10.1016/j.matt.2020.11.015

[30] S. Singh, H. Chen, S. Shahrokhi, L. P. Wang, C. H. Lin, L. Hu, X. Guan, A. Tricoli, Z. J. Xu, T. Wu, Hybrid organic–inorganic materials and composites for photoelectrochemical water splitting. ACS Energy Lett., 5, 5, 1487–1497 (2020). doi: 10.1021/acsenergylett.0c00327

[31] X. Zhu, Y. Lin, J. San Martin, Y. Sun, D. Zhu, Y. Yan, Lead halide perovskites for photocatalytic organic synthesis. Nat. Commun. 2019, 10 (1), 2843. doi: 10.1038/s41467-019-10634-x

Chapter 2 A New Supramolecular Assembly Approach for Constructing Halide Perovskite Building Blocks

Parts of the content of this chapter were reprinted and adapted from the following publications with permission: Cheng Zhu, Jianbo Jin, Mengyu Gao, Alexander M. Oddo, Maria C. Folgueras, Ye Zhang, Chung-Kuan Lin, and Peidong Yang. "Supramolecular assembly of halide perovskite building blocks." Journal of the American Chemical Society, 2022, 144(27), 12450-12458. Copyright © 2022, American Chemical Society.

2.1 Introduction

The $[MX_6]^{n-}$ (M = Pb^{2+}[1-3], Sb^{3+}[4-6], Te^{4+}[7-9], Sn^{4+}[10,11], Pt^{4+}[11], etc.; X = Cl^-, Br^-, I^-) metal halide ionic octahedral units are the fundamental building blocks and functional units in metal halide perovskites. To this end, metal halide perovskites can be described as the extended assembly of those octahedra balanced by counter cations[12,13]. In this work, we introduce supramolecular cations as the counter cations for constructing the metal halide octahedron assembly. Crown ether can readily coordinate with alkali metals to form crown ether@alkali metal cations that have been widely used for supramolecular assembly[14,15]. Various assemblies of polyoxometalate clusters[16] and metal halide clusters, such as the five-coordinate $[SbX_5]^{2-}$ complex[17] or the four-coordinate $[FeCl_4]^-$[18] and $[MnBr_4]^{2-}$[19] complexes, can be achieved by employing different crown ether@alkali metal complexes. Here we show that the assembly of metal halide octahedron results in a family of unique dumbbell-shaped (crown ether@A)$_2$M(IV)X_6 (crown ether = 18-Crown-6 (18C6), 21-Crown-7 (21C7); A = Cs^+, Rb^+, K^+; M = Te^{4+}, Sn^{4+}, Se^{4+}, Ir^{4+}, Pt^{4+}, Zr^{4+}, Ce^{4+}; X = Cl^-, Br^-, I^-) structural units in solution, which can be further packed into various three-dimensional crystal structures. Moreover, the optoelectronic properties of the resulted assembly can be tuned through the supramolecular cations, providing an additional knob for the rational design of functional metal halide perovskites.

Previous works have shown, that upon dissolving bulk $A_2M(IV)X_6$ vacancy-ordered double perovskites in polar aprotic solvents, the ionic bond between the $[M(IV)X_6]^{2-}$ and the alkali metal cations (A^+) dissociates and the metal halide octahedral units can be stabilized in solution[20]. Additionally, when 18C6 was dissolved in solution, the strong electrostatic interaction between the alkali metal cations A^+ and the oxygen atoms of 18C6 favored $(18C6@A)^+$ cation formation[21,22]. Furthermore, we discovered that the $[M(IV)X_6]^{2-}$ octahedra and the $(18C6@A)^+$ cations in solution exist as a (18C6@A)$_2$M(IV)X_6 dumbbell structural unit, where each octahedron is sandwiched by two $(18C6@A)^+$ cations (**Figure 2.1**). This configuration lays the foundation for solid-state supramolecular assembly. Using the anti-solvent vapor assisted crystallization method, the dumbbell building blocks packed into a unique rhombohedral lattice (**Figure 2.1**), which was different from the face-centered cubic (FCC)-type lattice formed by $[M(IV)X_6]^{2-}$ and A^+ alone. This new, general synthetic strategy allows us to extend a family of new structures based upon these metal halide octahedral building blocks.

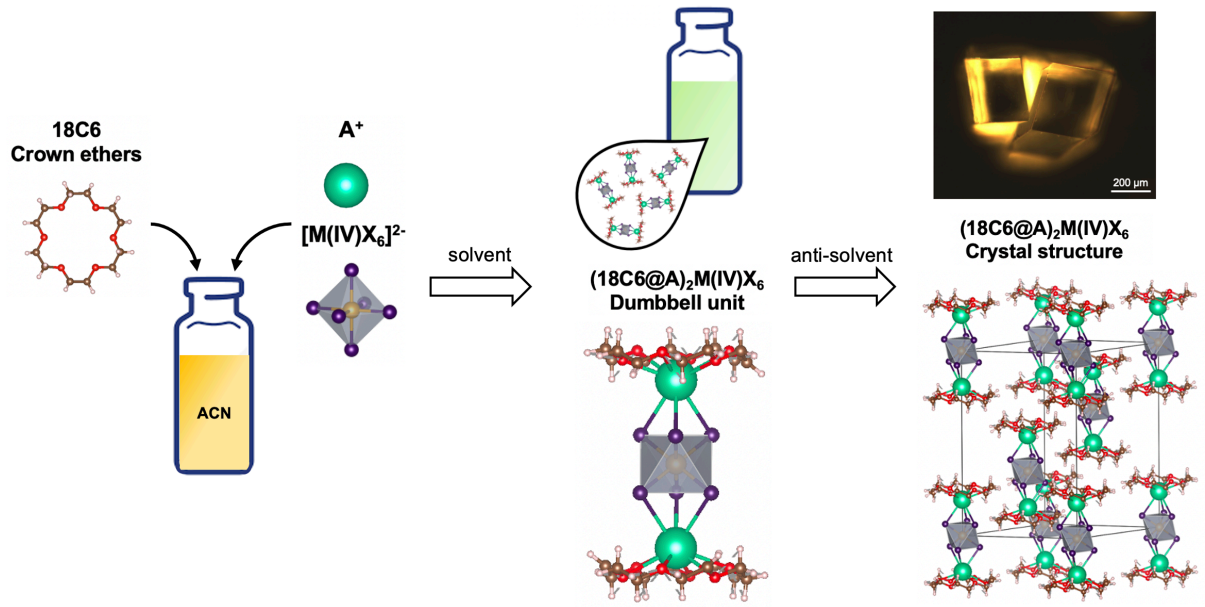

Figure 2.1. The supramolecular assembly strategy from $[M(IV)X_6]^{2-}$ octahedron to $(18C6@A)_2M(IV)X_6$. Dissolved alkali metal cation (A^+) and $[M(IV)X_6]^{2-}$ octahedron self-assemble into a dumbbell-shaped structural unit with crown ethers like 18-Crown-6 (18C6). The solution dispersed $(18C6@A)_2M(IV)X_6$ dumbbell structural units can further assemble into a rhombohedral packing single crystal. The dark field optical microscope image shows single crystals of $(18C6@Cs)_2Te(IV)Cl_6$.

2.2 The Supramolecular Assembly Approach

2.2.1 Dumbbell Structural Unit Formation in Solution

The charge-neutral $(18C6@A)_2M(IV)X_6$ dumbbell structural units formed by dissolving 18C6 and $A_2M(IV)X_6$ in acetonitrile (ACN). This has been proved by multiple solution-state characterization techniques, using $(18C6@Cs)_2TeBr_6$ as an illustrating example. The NMR-active ^1H, ^{79}Br, and ^{133}Cs nuclei in the dumbbell structural unit feel different magnetic fields compared to the dissociated nuclei (**Figure 2.2a-c**). The 24 homotopic protons on the 18C6 ring have identical NMR absorptions, at around 3.54 ppm in terms of chemical shift. If a Cs^+ is crowned, due to the partial removal of proton electron density by the cation, the protons will be deshielded and the chemical shift will increase to 3.59 ppm (**Figure 2.2a**), consistent with reports that $(18C6@Cs)^+$ exists in ACN [21]. However, with the addition of $[TeBr_6]^{2-}$ ionic octahedra, the chemical shift is further increased to 3.61 ppm. This increase indicated further withdrawal of electron density from the protons in the presence of $[TeBr_6]^2$, which implied attachment to the $(18C6@Cs)^+$ cations. ^{79}Br NMR revealed strong signals of free Br^- ions of CsBr in ACN, while the spin relaxation of ^{79}Br was quenched completely by Te^{4+} in Cs_2TeBr_6 (**Figure 2.2b**) under the same measurement conditions. $(18C6@Cs)_2TeBr_6$ in ACN showed the same quenching behavior as the Cs_2TeBr_6; the absence of ^{79}Br NMR signal confirmed that Br was coordinated to Te^{4+}.

To provide complete evidence that the dumbbell structural unit exists in ACN, ^{133}Cs NMR (**Figure 2.2c**) was also conducted since Cs is the bridging atom that directly coordinates to both, Br of $[TeBr_6]^{2-}$ and O of 18C6. The free Cs chemical shift of CsBr was located at 38.81 ppm, while it was located at 35.56 ppm for Cs_2TeBr_6 in ACN. The 3.25-ppm difference in these controls indicated that the presence of Te^{4+} in the solution caused the peak to shift to lower ppm values. In contrast, a pronounced shielding effect was observed when Cs^+ was crowned into $(18C6@Cs)^+$ in ACN, which suggested a withdrawal of electron density from the crown ether to Cs^+, consistent with the ^{1}H NMR results. Adding $[TeBr_6]^{2-}$ into $(18C6@Cs)^+$ in ACN changed the Cs chemical shift from 22.21 ppm to 22.92 ppm, which supported the formation of a new species, the dumbbell structural unit, distinct from its individual components. The dramatically broadened signal also supported the formation of the dumbbell, as dipole-dipole interactions are introduced in slowly tumbling large molecular weight species. UV-vis spectrum of $(18C6@Cs)_2TeBr_6$ precursors in ACN clearly shows the A, B and C characteristic absorption bands of $[TeBr_6]^{2-}$[20] (**Figure 2.2d**), indicating the presence of the $[TeBr_6]^{2-}$ in solution. With the comprehensive measurements in ^{1}H, ^{79}Br, and ^{133}Cs NMR and UV-vis spectroscopy, we characterized the species in the solution phase, confirming the integrity of the dumbbell structural unit in solution.

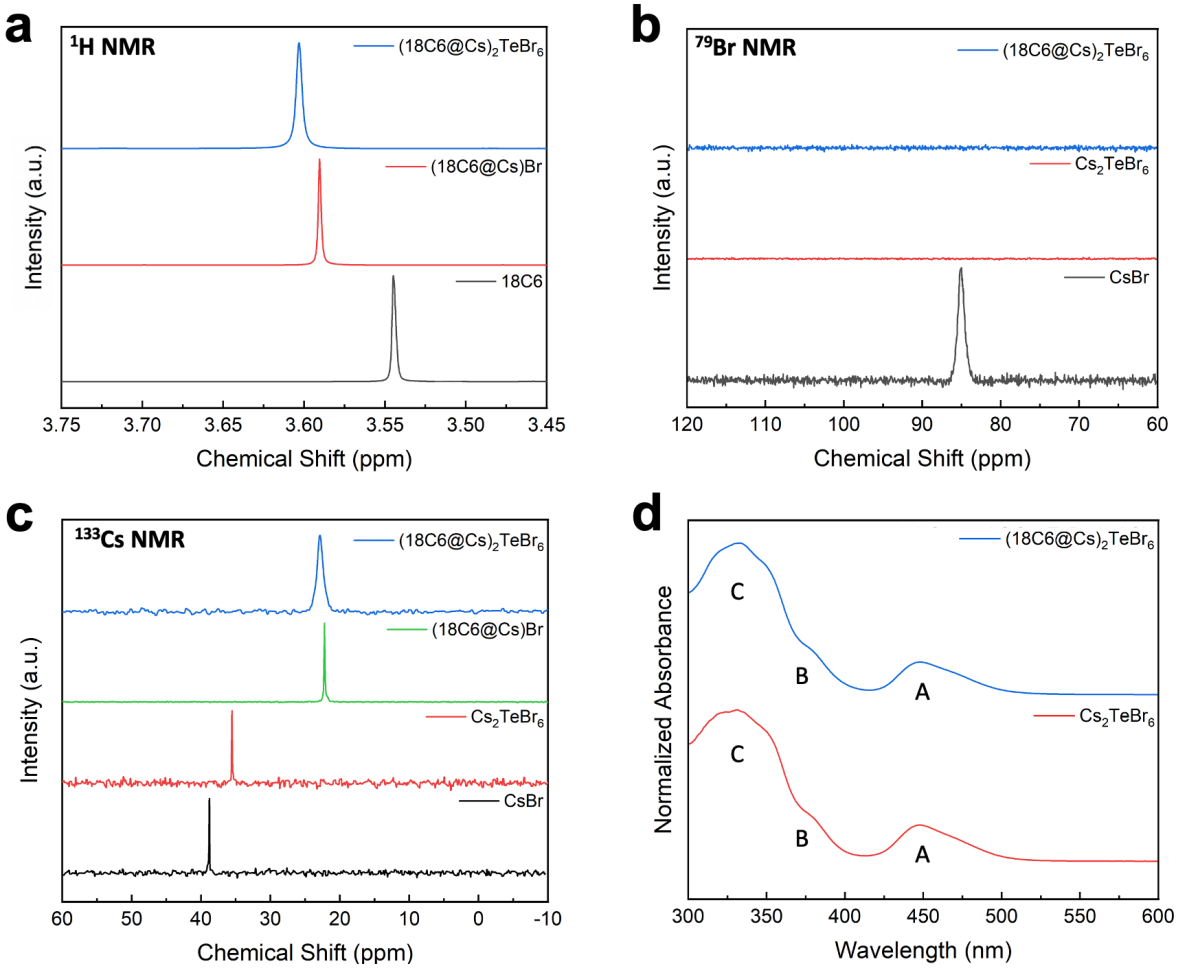

Figure 2.2. Evidence of the formation of $(18C6@A)_2M(IV)X_6$ dumbbell structural unit in solution. The composition of $(18C6@Cs)_2TeBr_6$ is applied as an illustrating example for the dumbbell structural unit, and acetonitrile (acetonitrile-d_3 for NMR) is used as the solvent. (a) ^1H NMR spectra for $(18C6@Cs)_2TeBr_6$ solution, and the control groups are (18C6@Cs)Br and 18C6 dissolved in solution; (b) ^{79}Br NMR spectra for $(18C6@Cs)_2TeBr_6$ solution, and the control groups are Cs_2TeBr_6 and CsBr dissolved in solution; (c) ^{133}Cs NMR spectra for $(18C6@Cs)_2TeBr_6$ solution, and the control groups are (18C6@Cs)Br, Cs_2TeBr_6 and CsBr dissolved in solution; and (d) UV-vis spectra comparison of $(18C6@Cs)_2TeBr_6$ solution and Cs_2TeBr_6 dissolved in solution.

2.2.2 Single-Crystal Formation and Characterization

With the suspension of $(18C6@A)_2M(IV)X_6$ in ACN solution, we successfully achieved the solid-state assembly, in the form of single crystals, with the introduction of antisolvents like diethyl ether. For example, the $(18C6@Cs)_2TeCl_6$ single crystals have a parallelepiped shape, consistent with crystallographic symmetry, with a lateral dimension of approximately 300 μm (**Figure 2.3**). The structural details were determined from single crystal X-ray diffractions (SCXRD). $(18C6@Cs)_2TeCl_6$ crystallized in the R-3 space group with lattice parameters of a = 13.9378 Å and c = 22.0396 Å (**Table 2.1**). The $(18C6@Cs)_2TeCl_6$ dumbbell structural unit belonged to the S_6 point group, where two Cs^+ cations and the Te^{4+} cation sit on the S_6 axis, and the six-fold symmetry of the 18C6 and S_6 axis of O_h-symmetric $[TeCl_6]^{2-}$ octahedron were perfectly aligned. In the $(18C6@Cs)_2TeCl_6$ dumbbell unit, the Te-Cl bond length was determined as 2.546 Å, which was comparable to that in the Cs_2TeCl_6 vacancy-ordered double perovskite (2.570 Å)[7]. The high symmetry of this dumbbell building block offered a unique rhombohedral packing of the octahedra at the macroscopic level. Each $[TeCl_6]^{2-}$ octahedron occupied the b Wyckoff position of space group R-3 and was surrounded by six nearest octahedra at a Te-Te distance of 10.9 Å, which was different from the FCC packing in Cs_2TeCl_6 with Te-Te distance of 7.7 Å[7]. These engineerable differences in the metal halide octahedron packing geometry may lead to differences in the overlap of molecular orbital wavefunctions, yielding unique electronic structures and optoelectronic properties that will be discussed later.

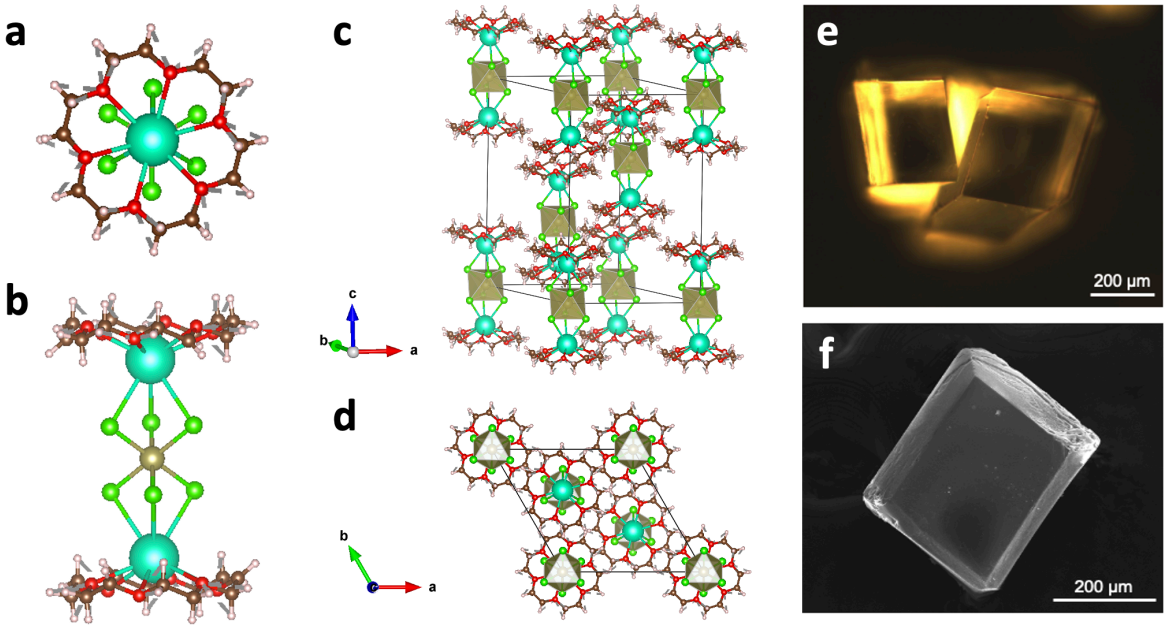

Figure 2.3. Crystal structure of one typical example: $(18C6@Cs)_2TeCl_6$. The atomic structure of the dumbbell $(18C6@Cs)_2TeCl_6$ structural unit from (a) top and (b) side view. $(18C6@Cs)_2TeCl_6$ single crystal is in rhombohedral R-3 space group: (c) oblique view and (d) top view. (e) Dark field optical image and (f) scanning electron microscope image of $(18C6@Cs)_2TeCl_6$ single crystal.

Table 2.1. Crystallographic tables for $(18C6@K)_2TeCl_6$, $(18C6@Rb)_2TeCl_6$, and $(18C6@Cs)_2TeCl_6$, single crystals.

Crystal	**$(18C6@K)_2TeCl_6$**	**$(18C6@Rb)_2TeCl_6$**	**$(18C6@Cs)_2TeCl_6$**
ICSD Number	2122205	2122204	2122203
Empirical formula	$C_{24}H_{48}Cl_6K_2O_{12}Te$	$C_{24}H_{48}Cl_6O_{12}Rb_2Te$	$C_{24}H_{48}Cl_6Cs_2O_{12}Te$
Formula weight	947.12	1039.86	1134.74
Temperature/K	293(2)	293(2)	293(2)
Crystal system	trigonal	trigonal	trigonal
Space group	R-3	R-3	R-3
a/Å	13.9266(6)	13.9737(6)	13.9400(3)
b/Å	13.9266(6)	13.9737(6)	13.9400(3)
c/Å	20.5594(8)	21.0360(9)	22.0991(6)
α/°	90	90	90
β/°	90	90	90
γ/°	120	120	120
Volume/Å^3	3453.3(3)	3557.3(3)	3719.04(19)
Z	3	3	3
ρ_{calc}mg/mm^3	1.366	1.456	1.520

μ/mm^{-1}	1.218	3.046	2.411
F(000)	1440.0	1548.0	1656.0
Crystal size/mm^3	0.51 × 0.388 × 0.194	0.185 × 0.155 × 0.136	0.273 × 0.174 × 0.082
Radiation	Mo Kα (λ = 0.71073)	Mo Kα (λ = 0.71073)	Mo Kα (λ = 0.71073)
2Θ range for data collection	5.85 to 58.914°	7.77 to 58.946°	8.05 to 58.982°
Index ranges	-15 ≤ h ≤ 16, -18 ≤ k ≤ 15, -25 ≤ l ≤ 27	-18 ≤ h ≤ 16, -17 ≤ k ≤ 19, -26 ≤ l ≤ 27	-18 ≤ h ≤ 19, -18 ≤ k ≤ 18, -30 ≤ l ≤ 30
Reflections collected	8381	8997	24112
Independent reflections	1857[R(int) = 0.0365]	1905[R(int) = 0.0329]	2130[R(int) = 0.0368]
Data/restraints/parameters	1857/0/69	1905/0/69	2130/0/69
Goodness-of-fit on F^2	1.043	1.100	1.108
Final R indexes [I>=2σ (I)]	R_1 = 0.0297, wR_2 = 0.0774	R_1 = 0.0450, wR_2 = 0.1206	R_1 = 0.0485, wR_2 = 0.1297
Final R indexes [all data]	R_1 = 0.0361, wR_2 = 0.0804	R_1 = 0.0572, wR_2 = 0.1272	R_1 = 0.0626, wR_2 = 0.1447
Largest diff. peak/hole / e $Å^{-3}$	1.01/-0.37	2.60/-0.85	3.87/-0.95

2.3 Compositional and Structural Tunability of the Dumbbell Structural Unit

To demonstrate the general applicability of our approach, we achieved various crystals through this supramolecular assembly strategy. In fact, the composition tunability of this new $(18C6@A)_2M(IV)X_6$ structure is as rich as the tunabilities on A, M, and X sites in $A_2M(IV)X_6$ double perovskites[23]. There are four compositional components in the $(18C6@Cs)_2TeCl_6$ dumbbell structural unit that can be tuned by virtue of the precursors: (a) octahedron cations (M), (b) halide anions (X), (c) alkali metal cations (A), and (d) crown ethers (**Figure 2.4**). Apart from the $[TeX_6]^{2-}$, various tetravalent center cation octahedra, such as $[SnX_6]^{2-}$, $[SeX_6]^{2-}$, $[IrX_6]^{2-}$, $[PtX_6]^{2-}$, $[ZrX_6]^{2-}$, $[CeX_6]^{2-}$[10,11,24-32], can also be assembled into similar dumbbell structural units with S_6 symmetry. For typical 3D-connected halide perovskites, such as low-T phase $CsPbI_3$[33], due to the geometrical constraint imposed by the ionic framework sizes, such as the tolerance factor and proper bonding directions, a mismatched ionic size will lead to the breakdown or instability of the perovskite structure[34]. In contrast, the isolated nature of the dumbbell structural units enables a more flexible control over the structure diversity without losing the prototypical crystal structure. Herein, we achieve a variety of unique dumbbell structures with our unique synthetic approach by simply changing the precursors. All structural details of the highly tunable $(18C6@A)_2M(IV)X_6$ dumbbell structural units were obtained by powder X-ray diffraction (PXRD) and SCXRD.

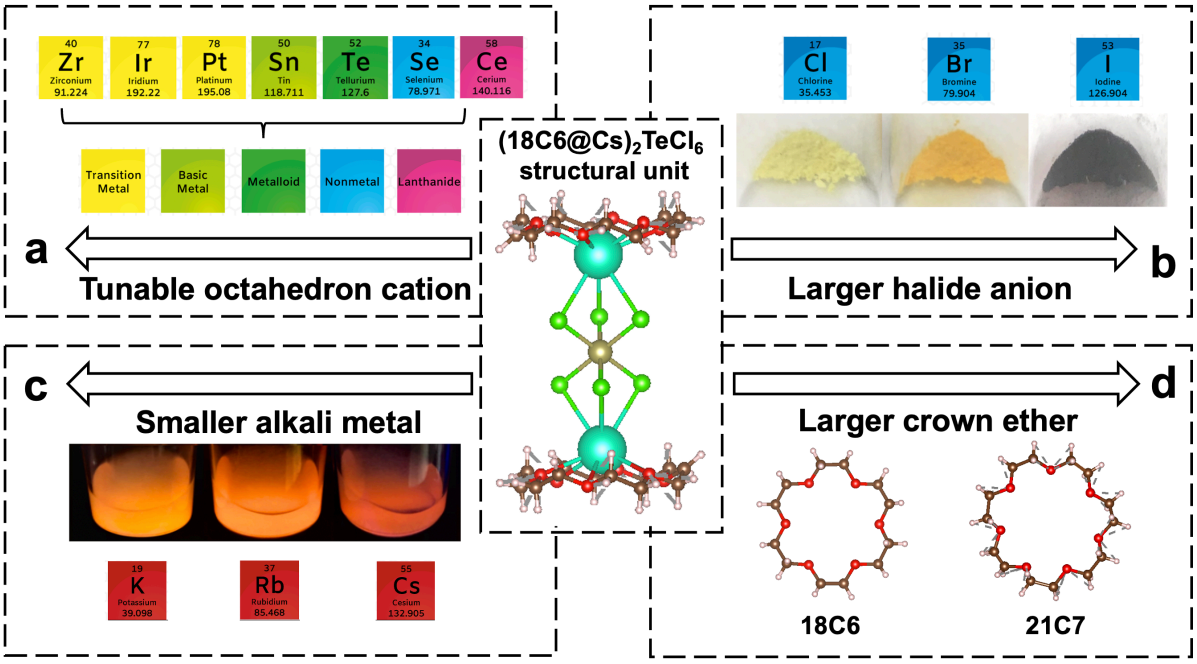

Figure 2.4. Synthetic tunability of the crown ether supramolecular approach. The four arrows represent the four dimensionalities in tuning the dumbbell structural unit from the initial $(18C6@Cs)_2TeCl_6$ structural unit: (a) seven tetravalent octahedra cations can be applied, including transition metal cations such as Zr^{4+}, Ir^{4+}, Pt^{4+}, basic metal cations such as Sn^{4+}, metalloid cations such as Te^{4+}, nonmetal cations such as Se^{4+}, and lanthanide cations such as Ce^{4+}; (b) tuning the halide anion from Cl^- to Br^- to I^-, and the optical images are the powders of $(18C6@Cs)_2TeX_6$ (X = Cl^-, Br^-, I^-) under ambient light; (c) modifying the alkali metal cation coupled with 18C6 from Cs^+ to Rb^+ to K^+, and the optical images are the powders of $(18C6@A)_2TeCl_6$ dispersed in an anti-solvent under UV lamp excitation; and (d) varying the size of the crown ether from 18C6 to 21C7.

The comparison of PXRD patterns for the seven different octahedron center cations (Te^{4+}, Sn^{4+}, Se^{4+}, Ir^{4+}, Pt^{4+}, Zr^{4+}, Ce^{4+}) is shown in **Figure 2.5a**. Despite size differences between the different metal halide octahedral units, represented by the M-Cl bond length (from 2.324 Å to 2.555 Å) summarized in **Figure 2.5b**, they all had similar hexagonal PXRD patterns, with strong and distinct (101) and (110) diffraction peaks. In order to better evaluate the geometry of the dumbbell structural unit with various composition, we used a simplified model made up with two cones and one octahedron. A larger halide anion (from Cl^- to Br^- to I^-) leads to a larger octahedron size (**Figure 2.6b**), and the length of the dumbbell structural unit increases in all three dimensions, reflected by the shifting of all diffraction peaks to lower 2θ values (**Figure 2.6a**). While the bromide version remained in the R-3 space group (**Table 2.2**), the iodide version deviated from the hexagonal symmetry and crystallized in the monoclinic crystal system with the space group of $P2_1/m$ (**Table 2.3**) due to the larger size of the iodide anion. On the contrary, we found that the M-X bonds were not influenced by the alkali metal cations, and the R-3 space group can be preserved. **Figure 2.7b** shows that the Te-Cl bond lengths were 2.546 Å, 2.548 Å, and 2.544 Å for the Cs-, Rb- and K-based assemblies, respectively. However, when using a smaller alkali cation, the height of the cone decreased (from ~2.4 Å to ~1.8 Å

when changing from Cs^+ to K^+), while the diameter of the cone remained nearly unchanged. This height decrease was consistent with a shift in the diffraction peaks related to the c lattice parameter (such as (101) and (104) planes) to larger 2θ values. In contrast, the diffraction of facets parallel to the c axis, such as the (110) plane, have almost no shift (**Figure 2.7a**).

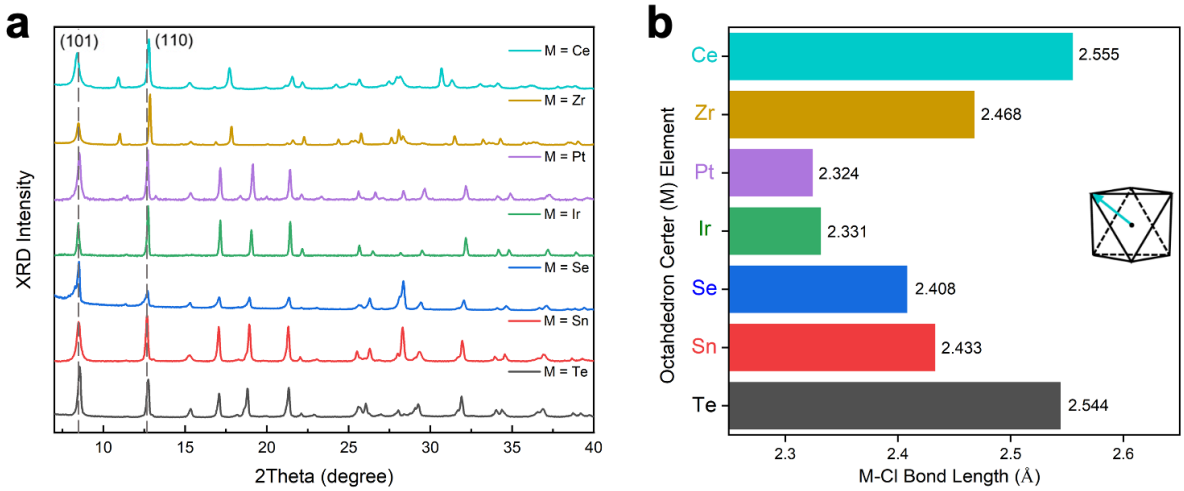

Figure 2.5. Systematic structural analysis of the family of $(18C6@A)_2M(IV)X_6$ crystals by tuning the octahedron center element (M) in $(18C6@A)_2M(IV)Cl_6$ (for M = Ce, Zr, A = Cs; for M = Pt, Ir, Se, Sn, Te, A = K). (a) Comparison of powder X-ray diffraction patterns; (b) the M-Cl bond length comparison of the structures with different octahedron center elements.

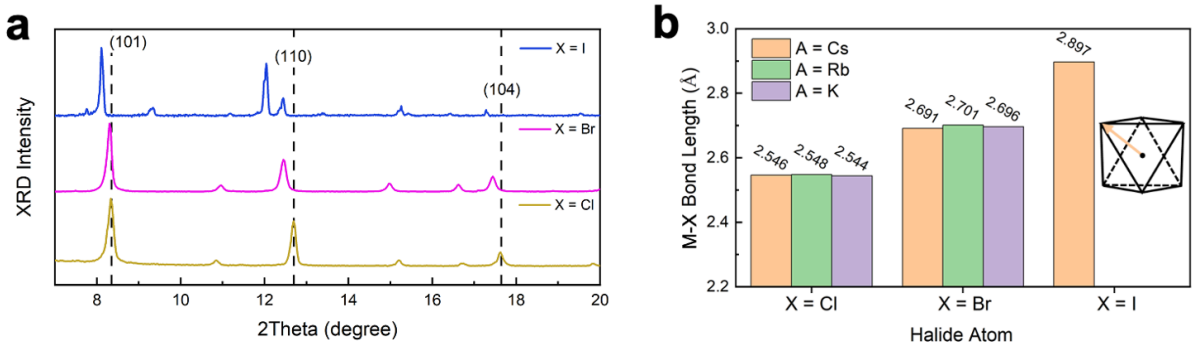

Figure 2.6. Systematic structural analysis of the family of $(18C6@A)_2M(IV)X_6$ crystals by changing the halide atom (X) in $(18C6@Cs)_2TeX_6$. (a) Comparison of powder X-ray diffraction patterns; (b) the M-X bond length increases with larger X.

Table 2.2. Crystallographic tables for $(18C6@K)_2TeBr_6$, $(18C6@Rb)_2TeBr_6$, and $(18C6@Cs)_2TeBr_6$, single crystals.

Crystal	**$(18C6@K)_2TeBr_6$**	**$(18C6@Rb)_2TeBr_6$**	**$(18C6@Cs)_2TeBr_6$**

ICSD Number	2122195	2122194	2122196
Empirical formula	$C_{24}H_{48}Br_6K_2O_{12}Te$	$C_{24}H_{48}Br_6O_{12}Rb_2Te$	$C_{24}H_{48}Br_6O_{12}Cs_2Te$
Formula weight	1213.88	1306.62	369.44
Temperature/K	293(2)	293(2)	293(2)
Crystal system	trigonal	trigonal	trigonal
Space group	R-3	R-3	R-3
a/Å	14.2030(6)	14.2117(7)	14.1941(3)
b/Å	14.2030(6)	14.2117(7)	14.1941(3)
c/Å	21.3516(10)	21.6941(12)	22.5099(5)
α/°	90	90	90
β/°	90	90	90
γ/°	120	120	120
Volume/Å^3	3730.1(4)	3794.6(4)	3927.53(19)
Z	3	3	44
ρ_{calc}mg/mm^3	1.621	1.715	6.873
μ/mm^{-1}	5.626	7.278	29.335
F(000)	1764.0	1872.0	6908.0
Crystal size/mm^3	0.283 × 0.235 × 0.159	0.264 × 0.205 × 0.16	0.242 × 0.094 × 0.09
Radiation	Mo Kα (λ = 0.71073)	Mo Kα (λ = 0.71073)	Mo Kα (λ = 0.71073)
2Θ range for data collection	6.894 to 58.626°	6.882 to 58.97°	6.872 to 59.14°
Index ranges	-17 ≤ h ≤ 19, -18 ≤ k ≤ 18, -26 ≤ l ≤ 27	-17 ≤ h ≤ 18, -18 ≤ k ≤ 18, -29 ≤ l ≤ 28	-19 ≤ h ≤ 19, -19 ≤ k ≤ 19, -27 ≤ l ≤ 31
Reflections collected	9333	9547	29928
Independent reflections	2005[R(int) = 0.0416]	2011[R(int) = 0.0377]	2260[R(int) = 0.0274]
Data/restraints/parameters	2005/0/69	2011/0/69	2260/0/69
Goodness-of-fit on F^2	1.045	0.956	1.062
Final R indexes [I>=2σ (I)]	R_1 = 0.0260, wR_2 = 0.0681	R_1 = 0.0184, wR_2 = 0.0425	R_1 = 0.0387, wR_2 = 0.1093
Final R indexes [all data]	R_1 = 0.0313, wR_2 = 0.0693	R_1 = 0.0241, wR_2 = 0.0433	R_1 = 0.0452, wR_2 = 0.1135
Largest diff. peak/hole / e Å^{-3}	0.38/-0.57	0.34/-0.34	3.79/-0.50

Table 2.3. Crystallographic tables for $(18C6@Cs)_2TeI_6$ single crystals.

Crystal	**$(18C6@Cs)_2TeI_6$**
ICSD Number	2122192

Empirical formula	$C_{27}Cs_2I_6NO_{13}Te$
Formula weight	1701.10
Temperature/K	293(2)
Crystal system	monoclinic
Space group	$P2_1/m$
a/Å	9.8064(2)
b/Å	14.6116(4)
c/Å	17.8497(4)
α/°	90
β/°	93.572(2)
γ/°	90
Volume/Å^3	2552.66(10)
Z	2
ρ_{calc}mg/mm^3	2.213
μ/mm^{-1}	5.661
F(000)	1506.0
Crystal size/mm^3	0.493 × 0.339 × 0.199
Radiation	Mo Kα (λ = 0.71073)
2Θ range for data collection	6.374 to 58.762
Index ranges	$-12 \le h \le 13$, $-19 \le k \le 18$, $-22 \le l \le 24$
Reflections collected	37382
Independent reflections	6491 [R_{int} = 0.1203, R_{sigma} = 0.0514]
Data/restraints/parameters	6491/0/248
Goodness-of-fit on F^2	1.098
Final R indexes [I>=2σ (I)]	R_1 = 0.0661, wR_2 = 0.1956
Final R indexes [all data]	R_1 = 0.0726, wR_2 = 0.2010
Largest diff. peak/hole / e Å^{-3}	1.48/-2.18

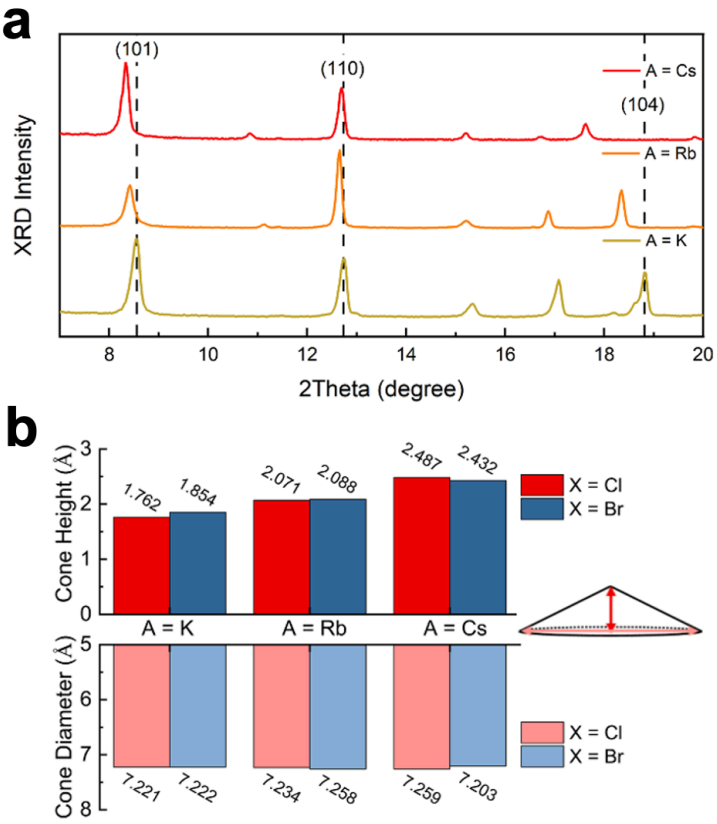

Figure 2.7. Systematic structural analysis of the family of $(18C6@A)_2M(IV)X_6$ crystals by varying the alkali metal atom (A) in $(18C6@A)_2TeCl_6$. (a) Comparison of powder X-ray diffraction patterns; (b) the height of the cone increases with larger A, while the diameter of the cone is insensitive to the change of A.

To further confirm the intact O_h symmetry of the metal halide octahedral building blocks, we used Raman spectroscopy to study the vibrational modes of the dumbbell structural unit. Previous Raman studies of the Cs_2TeCl_6 crystal system determined that the vibrational units in the single crystals were the isolated $[TeCl_6]^{2-}$ octahedra with O_h point group symmetry[7] (**Figure 2.8a**). All three characteristic Raman peaks were still observed in the $(18C6@A)_2TeCl_6$ single crystals (**Figure 2.8b**), confirming the O_h symmetry of the $[TeCl_6]^{2-}$ unit in the dumbbell building block.

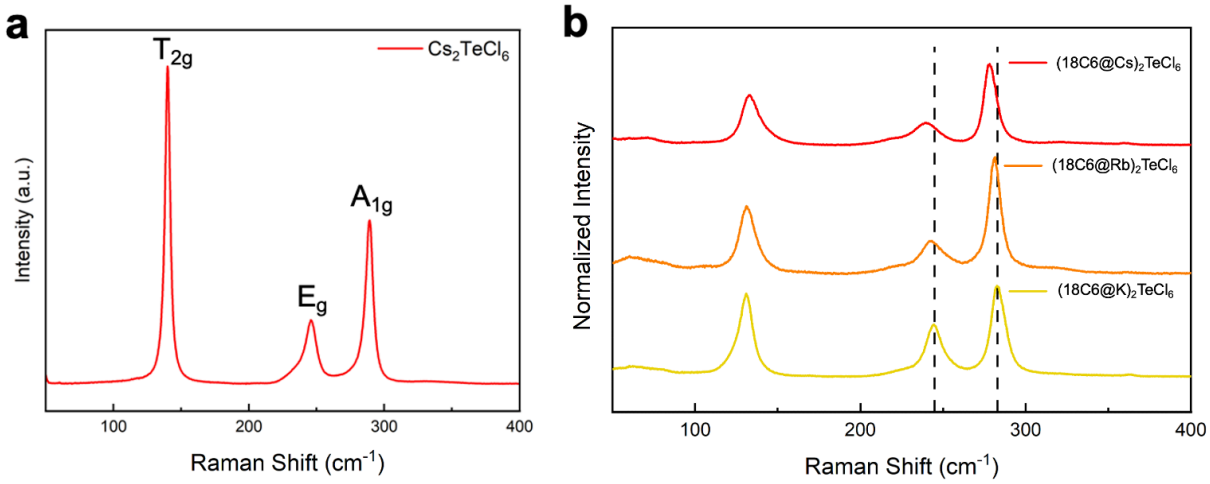

Figure 2.8. Raman spectrum of $[TeCl_6]^{2-}$ octahedra in various crystals. (a) Raman spectrum of Cs_2TeCl_6. (b) Normalized Raman spectra of $(18C6@A)_2TeCl_6$ ($A = Cs^+$, Rb^+, K^+) crystals.

The compatibility between the point groups of 18C6 and the metal halide octahedral units resulted in the rhombohedral R-3 space group of the assembled single crystals. By breaking the six-fold symmetry of the crown ether, the supramolecular approach can realize more packing geometries for these metal halide octahedral units. For example, the larger 21-Crown-7 (21C7) had to distort itself to coordinate with the center Cs^+ cation (**Figure 2.9a**). Such distortion of the dumbbell building block dramatically altered the packing geometry of those building blocks (**Figure 2.9b**). Single crystals of $(21C7@Cs)_2TeBr_6$ and $(21C7@Cs)_2TeI_6$ crystallized in an orthorhombic lattice with space group $Cmc2_1$ (**Table 2.4**). The $[TeBr_6]^{2-}$ units in $(21C7@Cs)_2TeBr_6$ dumbbell unit were still nearly perfect, but this distorted dumbbell structure was found to be horizontally packed into a 2D array form. In each $[TeBr_6]^{2-}$ octahedral plane, one octahedron had four nearest neighbors (Te-Te distance is 9.9 Å), with no solvent molecules or crown ether complexes in between. The interlayer spacing of the 2D octahedral sheets was about 13.7 Å. Consistent with a 2D structure, the (002) diffraction peak was much stronger than the other diffraction peaks (**Figure 2.10**). The single crystal had a planar shape with a width of over 400 μm and a thickness of only 35 μm (**Figure 2.11**). Therefore, the use of 21C7 introduced another new type of metal halide octahedral unit packing in supramolecular assemblies.

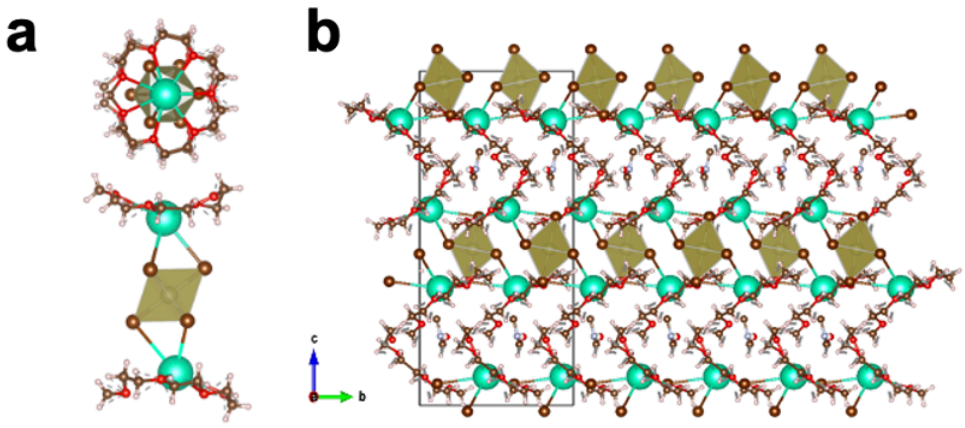

Figure 2.9. Single crystal XRD characterization of 21C7 assembled crystals. (a) The structure of the $(21C7@Cs)_2TeBr_6$ fundamental building block. (b) Crystal structure of $(21C6@Cs)_2TeBr_6$ viewed from the a axis.

Table 2.4. Crystallographic tables for $(21C7@Cs)_2TeBr_6$, and $(21C7@Cs)_2TeI_6$ single crystals.

Crystal	**$(21C7@Cs)_2TeBr_6$**	**$(21C7@Cs)_2TeI_6$**
ICSD Number	2122191	2122190
Empirical formula	$C_{31}H_{43}Br_6Cs_2NO_{15}Te$	$C_{30}H_{35}Cs_2I_6NO_{15}Te$
Formula weight	1542.54	1803.40
Temperature/K	293(2)	293(2)
Crystal system	orthorhombic	orthorhombic
Space group	$Cmc2_1$	$Cmc2_1$
a/Å	15.6291(6)	15.7635(11)
b/Å	12.0777(4)	12.3817(10)
c/Å	27.5528(18)	28.124(3)
α/°	90	90
β/°	90	90
γ/°	90	90
Volume/Å^3	5201.0(4)	5489.1(8)
Z	4	4
ρ_{calc}mg/mm^3	1.970	2.182
μ/mm^{-1}	21.138	5.274
F(000)	2912.0	3284.0
Crystal size/mm^3	0.091 × 0.051 × 0.05	0.157 × 0.103 × 0.045
Radiation	Cu Kα (λ = 1.54184)	Mo Kα (λ = 0.71073)
2Θ range for data collection	9.796 to 158.18	5.926 to 52.74
Index ranges	-19 ≤ h ≤ 19, -11 ≤ k ≤ 15, -34 ≤ l ≤ 34	-19 ≤ h ≤ 17, -14 ≤ k ≤ 15, -35 ≤ l ≤ 35
Reflections collected	53691	19078

Independent reflections	5669 [R_{int} = 0.1006, R_{sigma} = 0.0378]	5213 [R_{int} = 0.0863, R_{sigma} = 0.0757]
Data/restraints/parameters	5669/1/220	5213/1/169
Goodness-of-fit on F^2	1.048	1.016
Final R indexes [I>=2σ (I)]	R_1 = 0.0497, wR_2 = 0.1233	R_1 = 0.0505, wR_2 = 0.0955
Final R indexes [all data]	R_1 = 0.0668, wR_2 = 0.1320	R_1 = 0.0873, wR_2 = 0.1060
Largest diff. peak/hole / e $Å^{-3}$	0.56/-0.81	0.63/-0.83
Flack Parameter	-0.005(3)	0.08(5)

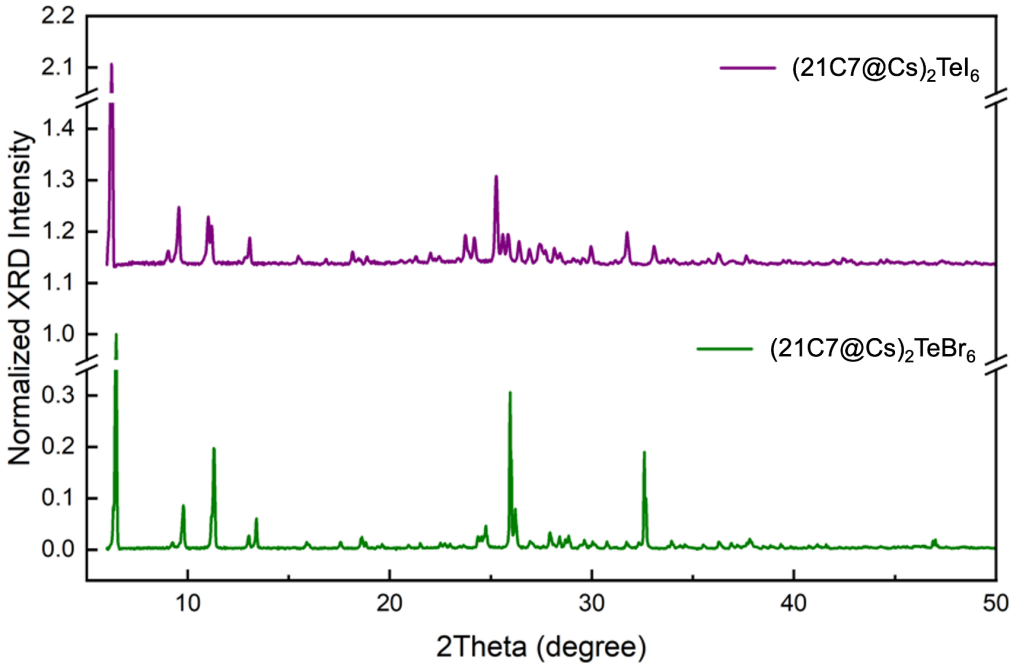

Figure 2.10. Powder X-ray diffraction pattern of $(21C7@Cs)_2TeX_6$ (X = Br^-, I^-).

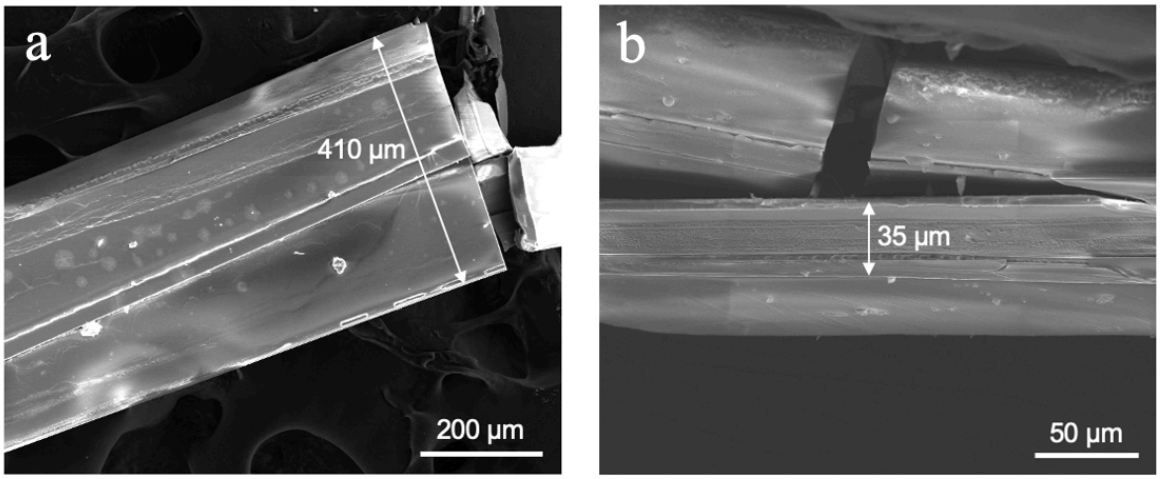

Figure 2.11. Scanning electron microscopy (SEM) image of the $(21C7@Cs)_2TeBr_6$ single crystal. (a) Top view and (b) side view.

2.4 Optoelectronic Properties of the Supramolecular Assemblies

2.4.1 Light Absorption Properties

The demonstrated synthetic flexibility and systematic control of the crystal structures assembled from the dumbbell structural unit have deep implications on their electronic properties. The electronic structure of the structural unit is primarily determined by the metal halide octahedral units[12]. For instance, by tuning the center metal cation of the $[M(IV)Cl_6]^{2-}$ (M = Sn^{4+}, Te^{4+}, Ce^{4+}, and Ir^{4+}) ionic octahedron, the optical absorption onset of the supramolecular assembled crystals varied from 660 nm for $[IrCl_6]^{2-}$, to 500 nm for $[CeCl_6]^{2-}$, to 460 nm for $[TeCl_6]^{2-}$, and to 310 nm for $[SnCl_6]^{2-}$ (**Figure 2.12**). The differences in absorption features for these four ionic octahedra are due to their different electronic configurations. Te^{4+} is a cation with ns^2 electronic configuration; the absorbance of $[TeCl_6]^{2-}$ octahedra was dominated by the molecular 5s to 5s5p transitions, represented as the A, B, and C bands[35]. Recent studies suggested that sharp absorption band in the UV range for $[SnCl_6]^{2-}$ can be assigned to a ligand-to-metal charge transfer (LMCT) transition[25,26]. The absorption band was also assigned to the LMCT transition for $[CeCl_6]^{2-}$[36]. For Ir, the subshells of the 5d-orbitals of Ir^{4+} in $[IrCl_6]^{2-}$ contributed to the weak optical transition bands and intense bands were due to metal-ligand interactions[37]. Changing the halide anions also contributed to different optical absorption. $(18C6@Cs)_2TeX_6$ (X = Cl^-, Br^-, I^-) structural units have vastly different optical absorption features due to shift of the atomic orbital energy levels of halide anions (**Figure 2.13**).

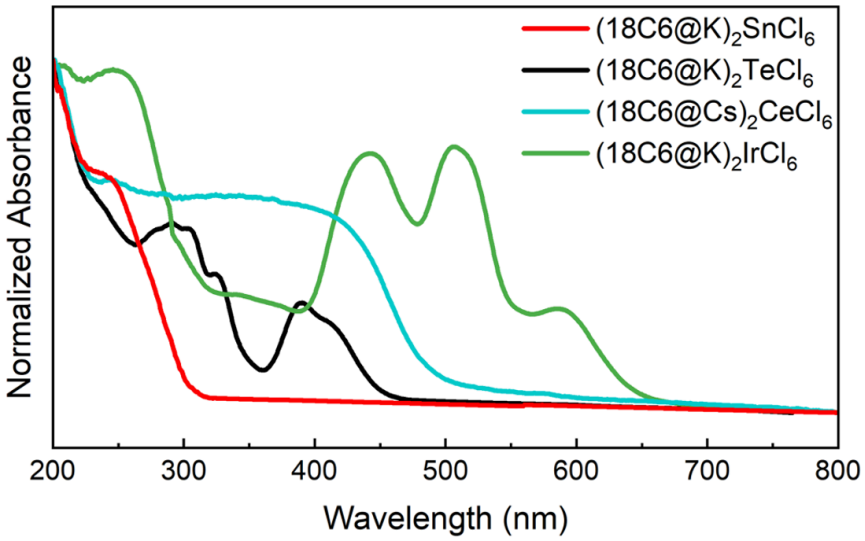

Figure 2.12. Normalized UV-vis absorption spectra of $(18C6@A)_2M(IV)Cl_6$ ($M = Sn^{4+}$, Te^{4+}, Ce^{4+}, Ir^{4+}) crystals.

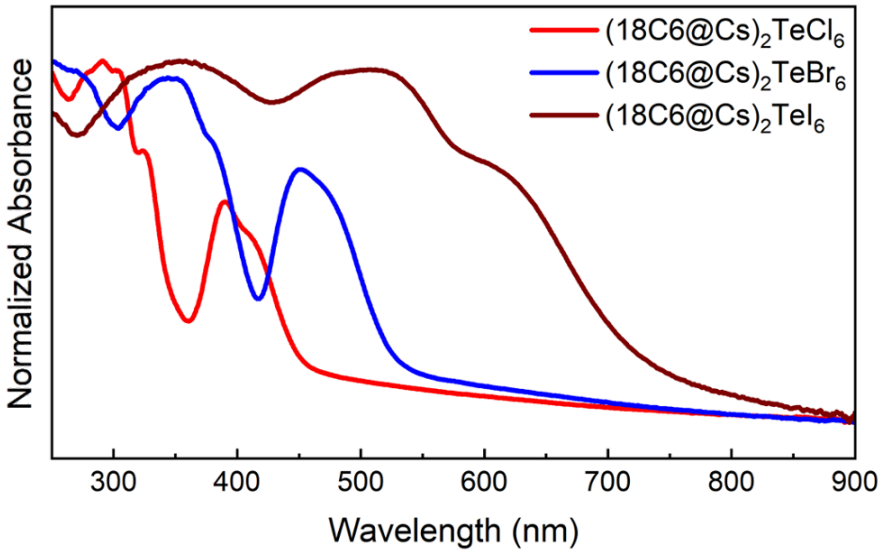

Figure 2.13. Normalized UV-vis absorption spectra of $(18C6@Cs)_2TeX_6$ ($X = Cl^-$, Br^-, I^-) crystals.

The optoelectronic tunability of the dumbbell unit can be achieved not only by incorporating various $[M(IV)X_6]^{2-}$ ionic octahedra, but also by changing the octahedral packing geometries and the surrounding coordination environment of the same metal-halide octahedra. The electronic interaction of these octahedral units has deep implications on the electronic structure of the crystal. According to the tight-binding model, the superposition of wave functions for isolated atoms will be greater when atoms are brought closer together in a solid, so the electronic bands will be more dispersive and the bandgap will decrease[38]. In the current materials system,

the individual octahedron can be viewed as a super ion/atom with specific molecular orbital levels. When the octahedra of these dumbbell units are closer to each other, their orbital wavefunctions will overlap to a greater extent. This was confirmed by our experimental observation. The UV-vis absorption spectra of four different packing geometries of $[TeBr_6]^{2-}$ octahedra are shown in **Figure 2.14**. As the $[TeBr_6]^{2-}$ octahedra were packed closer in a crystal by using different crown ether complexes, the A band absorption onset red shifted from 500 nm to 590 nm, causing the crystal to change color from orange [$(18C6@Cs)_2TeBr_6$ and $(21C7@Cs)_2TeBr_6$] to red [Cs_2TeBr_6].

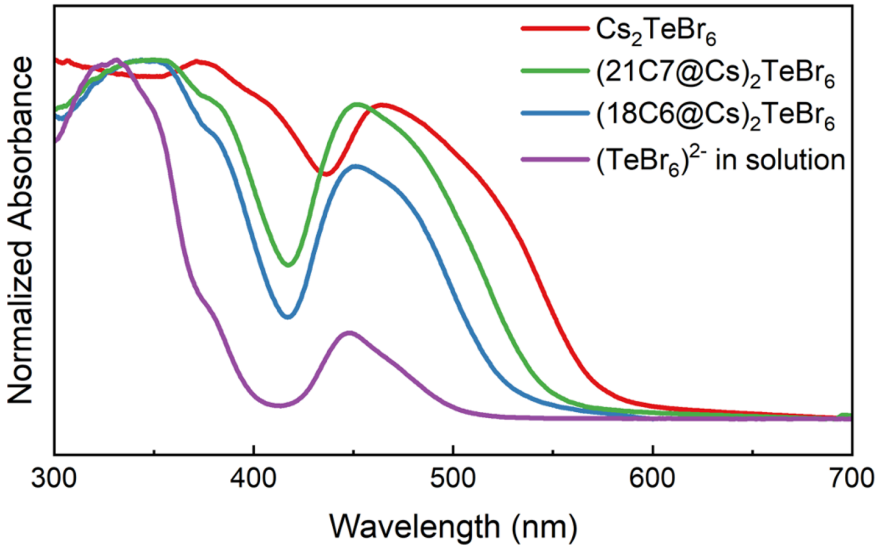

Figure 2.14. Normalized UV-vis absorption spectra of $[TeBr_6]^{2-}$ octahedra in four different packing geometries.

2.4.2 Light Emission Properties

The optical properties of the supramolecular assembled crystals were tunable, not only regarding the optical absorption, but also in terms of the photoluminescence (PL) properties. The strong coupling of the exciton with lattice vibrations is known in many isolated halide octahedra including $[TeX_6]^{2-}$, $[SnX_6]^{2-}$, and $[PtX_6]^{2-}$[9,27,28,39,40]. This exciton-phonon coupling effect will greatly lower the energy level of the exciton, forcing it into transient self-trapped exciton (STE) states with a range of self-trapped energy levels. $[TeCl_6]^{2-}$ octahedron was selected to study the STE emission of the dumbbell structural units. The PL spectra (**Figure 2.15**) of the $(18C6@A)_2TeCl_6$ ($A = K^+$, Rb^+, Cs^+) crystals had emission peak wavelengths at 604 nm, 642 nm, 659 nm, respectively. They all featured a large Stokes shift of 1.13 eV, 1.26 eV, 1.31 eV, respectively, and a very broadband emission. The PL full width at half maximum (FWHM) were as large as 0.44 eV, 0.54 eV, and 0.55 eV, respectively. The Stokes shift was larger than that of the Cs_2TeCl_6 crystal, with a value of 1.04 eV[7], which indicated greater exciton-phonon coupling effect[39,40]. Furthermore, the Stokes shift increased with increasing alkali metal cation size. This phenomenon was likely due to the difference in the alkali metal-

halide bond strength. A weaker or softer alkali metal-halide bond will force the excitonic state into deeper self-trapped levels.

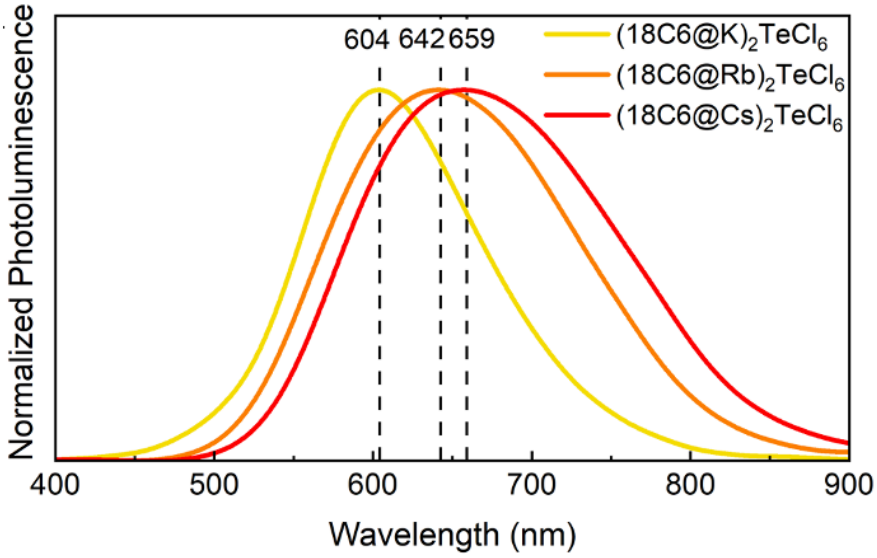

Figure 2.15. Normalized photoluminescence spectra of $(18C6@A)_2TeCl_6$ ($A = Cs^+, Rb^+, K^+$) crystals.

2.5 Experimental Methods

2.5.1 Materials Preparations

Chemicals. 18-Crown-6 (18C6, 99%, Sigma Aldrich), 21-Crown-7 (21C7, 97%, Alfa Chemistry), CsCl (99.999%, Sigma Aldrich), CsBr (99.999%, Sigma Aldrich), CsI (99.999%, Sigma Aldrich), RbCl (99.95%, Sigma Aldrich), RbBr (99.6%, Sigma Aldrich), RbI (99.9%, Sigma Aldrich), KCl (99%, Sigma Aldrich), KBr (99%, Sigma Aldrich), KI (99%, Sigma Aldrich), $TeCl_4$ (99.9%, Alfa Aesar), $TeBr_4$ (99.9%, Alfa Aesar), TeI_4 (99%, Alfa Aesar), $SnCl_4$ (99.9%, Alfa Aesar), $SnBr_4$ (99.9%, Alfa Aesar), K_2PtCl_6 (99.99%, Sigma Aldrich), K_2IrCl_6 (99.99%, Sigma Aldrich), $SeCl_4$ (35.0-36.5% Se basis, Sigma Aldrich), $ZrCl_4$ (99.99%, Sigma Aldrich), $(NH_4)_2Ce(NO_3)_6$ (99.99%, Sigma Aldrich), hydrochloric acid (HCl, 37%, Sigma Aldrich), hydrobromic acid (HBr, 48%, Sigma Aldrich), hydroiodic acid (HI, 57%, Sigma Aldrich), *N,N*-dimethylformamide (DMF, Fisher Scientific), acetone (Sigma Aldrich), acetonitrile (ACN, Sigma Aldrich), acetonitrile-d_3 (ACN-d_3, ≥99.8 atom % D, Sigma Aldrich) and diethyl ether (DEE, Sigma Aldrich) were used as received without further purification or modification.

Synthesis of A_2MX_6 ($A = Cs^+, Rb^+, K^+$; $M = Te^{4+}, Sn^{4+}, Zr^{4+}$; $X = Cl^-, Br^-, I^-$) Powders. Precursor powders AX and MX_4 were measured into a 20 ml vial based on the 2:1 stoichiometric ratio, and the precursors were dissolved in 5 ml of HX acid. Precipitates were filtered immediately and washed with HX acid. Precipitates were dried in a vacuum oven at 60°C overnight.

Synthesis of K_2SeCl_6 Powders. Precursor powders KCl and $SeCl_4$ were measured into a 20 ml vial based on the 2:1 stoichiometric ratio, and the precursors were dissolved in 5 ml of DMF on a hot plate at 100℃ for three hours in an argon glovebox. The supersaturated solution was filtered into a new 20 ml vial and 10 ml of DEE was added into the solution as anti-solvent. Precipitates were filtered, washed with acetone and dried in the vacuum oven at 60℃ overnight.

Synthesis of Cs_2CeCl_6 Powders. Cs_2CeCl_6 powders were synthesized using the same procedure as literature[41]. Precursor powders of CsCl and $(NH_4)_2Ce(NO_3)_6$ based on the 2:1 stoichiometric ratio were dissolved in 4 ml of HCl at 4℃. The precipitate was filtered immediately and washed with 1 ml of cooled HCl. The precipitate was dried in vacuum oven at room temperature overnight.

Synthesis of $(18C6@A)_2M(IV)X_6$ ($A = Cs^+, Rb^+, K^+$; $M = Te^{4+}, Sn^{4+}, Se^{4+}, Ir^{4+}, Pt^{4+}, Zr^{4+}, Ce^{4+}$; $X = Cl^-, Br^-, I^-$). Powders of A_2MX_6 and 18C6 were measured into a 20 ml vial based on the 1:2 stoichiometric ratio, and the precursors were dissolved in 10 ml of ACN or DMF on a hot plate at 100℃ with vigorous stirring for three hours. The supersaturated solution was filtered into a new 20 ml vial. $(18C6@A)_2M(IV)X_6$ powders were obtained by adding 10 ml of the supersaturated solution into 20 ml of DEE anti-solvent in a 50 ml centrifuge tube. The mixtures were centrifuged at 4000 rpm for 5 minutes to separate the powders and the solution. The powders were dried in a vacuum oven at 50℃ overnight. Se^{4+} and Zr^{4+}versions were hydroscopic, and an argon glovebox was used to avoid air exposure during the whole process. using the solution-based anti-solvent vapor method. $(18C6@A)_2M(IV)X_6$ single crystals were grown using an anti-solvent diffusion method. 1 ml of the abovementioned supersaturated solution was added into a 4 ml vial, which was placed into a 20 ml vial with 4 ml of DEE. After approximately two days, single crystals were formed on the bottom and the wall of the 4 ml vial. Single crystals were washed 3 times with acetone and stored in an argon glovebox for future use.

Synthesis of $(21C7@Cs)_2TeX_6$ ($X = Br^-, I^-$). $(21C7@Cs)_2TeX_6$ ($X = Br^-, I^-$) powders and single crystals were synthesized using methods similar as the $(18C6@A)_2M(IV)X_6$ but replacing 18C6 with 21C7.

2.5.2 Materials Characterizations

Single-Crystal X-ray Diffraction (SCXRD). The SCXRD data were collected at the Small Molecule X-ray Crystallography Facility (CheXray) in College of Chemistry, UC Berkeley. SCXRD were measured with a Rigaku XtaLAB P200 instrument equipped with a MicroMax-007 HF microfocus rotating anode and a Pilatus 200K hybrid pixel array detector using monochromated Mo Kα radiation (λ = 0.71073 Å). All crystal datasets were collected at room temperature (298 K). CrysAlisPro[42] was used for data collection and data processing, including a multi-scan absorption correction applied using the SCALE3 ABSPACK scaling algorithm within CrysAlisPro. Using Olex2[43], the structures were solved with the SHELXT[44] structure solution program using Intrinsic Phasing and refined with the SHELXL[45] refinement package using Least Squares minimization. Due to the occupation of disordered solvent molecules in the crystal voids, solvent masks were used during the refinement. All reflections where [error/esd] > 5 were omitted, as the existence of disordered molecules will result in high error/esd values in low d-spacing diffractions.

Ambient Condition Powder X-ray Diffraction. Powder X-ray diffraction (PXRD) data of $(18C6@A)_2MX_6$ (A = Cs^+, Rb^+, K^+; M = Te^{4+}, Sn^{4+}, Ir^{4+}, Pt^{4+}, Zr^{4+}, Ce^{4+}; X = Cl^-, Br^-, I^-) and $(21C7@Cs)_2TeX_6$ (X = Br^-, I^-) were collected using a Bruker D8 laboratory diffractometer with a Cu Kα radiation source in ambient condition. Data was collected from $2\theta = 7° - 50°$. The single crystals were ground into powders and transferred onto glass for measurements.

Inert Atmosphere Powder X-ray Diffraction. PXRD of $(18C6@K)_2SeCl_6$ was collected using a Rigaku Miniflex 6G Benchtop Powder XRD with a Cu Kα radiation source and an inert atmosphere sample holder. The powder samples were loaded onto the sample holder inside an argon glovebox.

Optical Microscope Imaging. An unpolarized, white-light optical microscope was used to visualize single crystals under either a 20× or a 50× microscope objective. The single crystals were observed under dark-field imaging. The single crystals were dispersed onto glass for measurement.

Scanning Electron Microscopy. A field-emission SEM (FEI Quanta 3D FEG SEM/FIB) was used to visualize single crystal morphologies at the QB3-Berkeley Biomolecular Nanotechnology Center (BNC).

Nuclear Magnetic Resonance Spectroscopy. All the NMR experiments were conducted in UC Berkeley's NMR facility in the College of Chemistry (CoC-NMR). The ^1H and ^{79}Br solution NMR were performed by Bruker AV600 and ^{133}Cs solution NMR was performed by Bruker AV500. Acetonitrile-d_3 was used as solvent for all the measurements.

Raman Spectroscopy. The Raman spectra of Cs_2TeCl_6, $(18C6@A)_2TeBr_6$, $(18C6@A)_2SnCl_6$, and $(18C6@A)_2SnBr_6$ (A = K^+, Rb^+, Cs^+) samples were measured by a confocal Raman microscope system (Horiba LabRAM HR800 Evolution). The single crystals were dispersed onto glass microscope slides for measurement. A continuous-wave (cw) 633 nm laser was focused onto a crystal facet at a constant power density set by neutral density filters. The Raman signal from the sample was collected using a microscope objective in a backscattering geometry (100×, NA 0.6). High-resolution Raman spectra were measured with a charge-coupled device (CCD) detector equipped with a diffraction grating of 1800 gr/mm and a long pass filter (80 cm^{-1}) to remove the Rayleigh scattering line from the signal.

Ultralow-Frequency (ULF) Raman Spectroscopy. The Raman spectra of the $(18C6@A)_2TeCl_6$ (A = K^+, Rb^+, Cs^+) samples were measured by a confocal Raman microscope system (Horiba LabRAM HR Evolution) at the Stanford Nano Shared Facilities (SNSF). The powders were dispersed onto glass microscope slides for measurement. A continuous-wave 633 nm laser was focused onto the powder, thin film, or coating surfaces at a constant power density set by neutral density filters. The Raman signal from the sample was collected using a microscope objective in a back-scattering geometry (100X, NA 0.6). High-resolution Raman spectra were measured with an Andor Newton DU970P BVF EMCCD detector equipped with a diffraction grating of 1800 gr/mm and an ULF filter package (10 cm^{-1}) to remove the Rayleigh scattering line from the signal.

PL Spectroscopy. Photoluminescence measurements were collected with a home-built PL microscope system. The single crystals were dispersed onto glass for measurement. A continuous-wave solid-state 375 nm laser (Coherent OBIS 375LX) was focused obliquely onto

the sample with a constant power density in visible wavelength measurements and infrared wavelength measurements, which was set by neutral density filters. The PL signal from the sample was collected using a microscope objective (50×) coupled to a long-pass filter (390 nm) in visible wavelength measurements and to a long-pass filter (800 nm) in infrared wavelength measurements to remove the laser line from the signal. Visible wavelength PL spectra were collected under a 1 s exposure time with a Si CCD detector cooled to -120℃ via liquid nitrogen and equipped with a diffraction grating of 150 gr/mm. The PL imaging was taken under bright-field conditions.

UV-Visible Absorption Spectroscopy. The absorption spectra of the samples were measured by a UV-visible spectrophotometer (Shimadzu UV-2600). Data was collected in absorption mode over a wavelength range of 200 nm and 900 nm with a medium scanning rate. The powder samples were widely dispersed on quartz glass. The solution samples were placed into a quartz cell with a 0.1 mm path length.

2.6 Conclusion

In conclusion, we demonstrated a general synthetic strategy for a library of new supramolecular building blocks (crown-ether@A)$_2$M(IV)X$_6$, constructed from ionic halide perovskite octahedral units and crown ether. The great tunability of (crown-ether@A)$_2$M(IV)X$_6$ can be explored along: (1) changing the octahedron cation, (2) tuning the halide anion, (3) modifying the alkali metal cation coupled with the crown ether, and (4) varying the size of the crown ether. In the future, based on the structural diversity of the supramolecular assembly approach, we expect to extend to 1D and 2D electronic dimensionality solid assembly with connected $[MX_6]^{n-}$ octahedra. Also, with all these synthetic possibilities, a more in-depth study of the optoelectronic properties of the ionic octahedral building blocks can be conducted. We expect that this new assembly strategy of the supramolecular building blocks could bring a new general method for halide perovskite materials discovery.

2.7 References

[1] Kovalenko, M. V.; Protesescu, L.; Bodnarchuk, M. I. Properties and Potential Optoelectronic Applications of Lead Halide Perovskite Nanocrystals. Science 2017, 358 (6364), 745-750.

[2] Zhang, Y.; Saidaminov, M. I.; Dursun, I.; Yang, H.; Murali, B.; Alarousu, E.; Yengel, E.; Alshankiti, B. A.; Bakr, O. M.; Mohammed, O. F. Zero-Dimensional Cs_4PbBr_6 Perovskite Nanocrystals. J. Phys. Chem. Lett. 2017, 8, 961-965.

[3] Noel, N. K.; Abate, A.; Stranks, S. D.; Parrott, E. S.; Burlakov, V. M.; Goriely, A.; Snaith, H. J. Enhanced Photoluminescence and Solar Cell Performance via Lewis Base Passivation of Organic Inorganic Lead Halide Perovskites. ACS Nano 2014, 8 (10), 9815-9821.

[4] Morad, V.; Yakunin, S.; Benin, B. M.; Shynkarenko, Y.; Grotevent, M. J.; Shorubalko, I.; Boehme, S. C.; Kovalenko, M. V. Hybrid 0D Antimony Halides as Air-Stable Luminophores for High Spatial-Resolution Remote Thermography. Adv. Mater. 2021, 33 (9), 2007355.

[5] Boopathi, K. M.; Karuppuswamy, P.; Singh, A.; Hanmandlu, C.; Lin, L.; Abbas, S. A.; Chang, C. C.; Wang, P. C.; Li, G.; Chu, C. W. Solution-Processable Antimony-Based Light-Absorbing Materials Beyond Lead Halide Perovskites. J. Mater. Chem. A 2017, 5, 20843-20850.

[6] Sedakova, T. V.; Mirochnik, A. G.; Karasev, V. E. Structure and Luminescence Properties of Antimony(III) Complex Compounds. Opt. Spectrosc. 2008, 105, 517-523.

[7] Folgueras, M.; Jin, J.; Gao, M.; Quan, L.; Steele, J.; Srivastava, S.; Ross, M.; Zhang, R.; Seeler, F.; Schierle-Arndt, K.; Asta, M.; Yang, P. Lattice Dynamics and Optoelectronic Properties of Vacancy-Ordered Double Perovskite Cs_2TeX_6 (X = Cl^-, Br^-, I^-) Single Crystals. J. Phys. Chem. C, 2021, 125, 25126-25139.

[8] Ju, D. X.; Zheng, X. P.; Yin, J.; Qiu, Z. W.; Turedi, B.; Liu, X. L.; Dang, Y. Y.; Cao, B. Q.; Mohammed, O. F.; Bakr, O. M.; Tao, X. T. Tellurium-Based Double Perovskites A_2TeX_6 with Tunable Band Gap and Long Carrier Diffusion Length for Optoelectronic Applications. ACS Energy Letters 2019, 4 (1), 228-234.

[9] Nicholas, A. D.; Walusiak, B. W.; Garman, L. C.; Huda, M. N.; Cahill, C. L. Impact of Noncovalent Interactions on Structural and Photophysical Properties of Zero-Dimensional Tellurium(IV) Perovskites. J. Mater. Chem. C 2021, 9, 3271-3286.

[10] Zhou, J.; Luo, J.; Rong, X.; Wei, P.; Molokeev, M. S.; Huang, Y.; Zhao, J.; Liu, Q.; Zhang, X.; Tang, J.; Xia, Z. Lead-Free Perovskite variant $Cs_2SnCl_{6-x}Br_x$ Single Crystals for Narrowband Photodetectors. Adv. Opt. Mater. 2019, 7, 1900139.

[11] Yin, H.; Chen, J.; Guan, P.; Zheng, D.; Kong, Q.; Yang, S.; Zhou, P.; Yang, B.; Pullerits, T.; Han, K. Controlling Photoluminescence and Photocatalysis Activities in Lead-Free $Cs_2Pt_xSn_{1-x}Cl_6$ Perovskites via Ion Substitution. Angew Chem. 2021, 60, 22693-22699.

[12] Jin, J.; Folgueras, M. C.; Gao, M.; Yu, S.; Louisia, S.; Zhang, Y.; Quan, L. N.; Chen, C.; Zhang, R.; Seeler, F.; Schierle-Arndt, K.; Yang, P. A New Perspective and Design Principle for Halide Perovskites: Ionic Octahedron Network (ION). Nano Lett. 2021, 21 (12), 5415-5421.

[13] Gao, M.; Zhang, Y.; Lin, Z.; Jin, J.; Folgueras, M. C.; Yang, P. The Making of a Reconfigurable Semiconductor with a Soft Ionic Lattice. Matter 2021, 4 (12), 3874−3896.

[14] Cram, D. J. The Design of Molecular Hosts, Guests, and Their Complexes. Angew. Chem., Int. Ed. Engl. 1988, 27, 1009-1112.

[15] Pedersen, C. J. The Discovery of Crown Ethers. Angew. Chem. 1988, 100, 1053-1059.

[16] Akutagawa, T.; Endo, D.; Noro, S. I.; Cronin, L.; Nakamura, T. Directing Organic–Inorganic Hybrid Molecular-Assemblies of Polyoxometalate Crown-Ether Complexes with Supramolecular Cations. Coord. Chem. Rev. 2007, 251, 2547-2561.

[17] Morad, V.; Yakunin, S.; Kovalenko, M. V. Supramolecular Approach for Fine-Tuning of the Bright Luminescence from Zero Dimensional Antimony(III) Halides. ACS Mater. Lett. 2020, 2, 845-852.

[18] Rogers, R. D.; Song, Y. The Crystal Structure of a Heterobimetallic crown ether complex: [Na(dibenzo-18-crown-6)]-[$FeCl_4$]. J. Chem. Crystallogr. 1995, 25, 579-582.

[19] Hausmann, D.; Kuzmanoski, A.; Feldmann, C. $MnBr_2$/18- crown-6 Coordination Complexes Showing High Room Temperature Luminescence and Quantum Yield. Dalton Trans. 2016, 45, 6541-6547.

[20] Folgueras, M. C.; Louisia, S.; Jin, J.; Gao, M.; Du, A.; Fakra, S. C.; Zhang, R; Seeler, F; Schrierle-Arndt, K.; Yang, P. Ligand-Free Processable Perovskite Semiconductor Ink. Nano Lett. 2021, 21 (20), 8856-8862.

[21] Hopkins Jr, H. P.; Norman, A. B. Conductance and Infrared Studies on Acetonitrile Solutions Containing Crown Ethers and Alkali Metal Salts. J. Phys. Chem., 1980, 84 (3), 309-314.

[22] Shamsipur, M.; Saeidi, M. Conductance Study of Binding of Some Rb^+ and Cs^+ Ions by Macrocyclic Polyethers in Acetonitrile Solution. J. Solut. Chem., 2000, 29 (12), 1187-1198.

[23] Maughan, A. E.; Ganose, A. M.; Scanlon, D. O.; Neilson, J. R. Perspectives and Design Principles of Vacancy-Ordered Double Perovskite Halide Semiconductors. Chem. Mater. 2019, 31 (4), 1184-1195.

[24] Faizan, M.; Bhamu, K.C.; Murtaza, G.; He, X.; Kulhari, N.; AL-Anazy, M.M.; Khan, S.H. Electronic and Optical Properties of Vacancy Ordered Double Perovskites A_2BX_6 (A= Rb, Cs; B= Sn, Pd, Pt; and X= Cl, Br, I): a First Principles Study. Sci. Rep. 2021 11 (1), 1-9.

[25] BelhajSalah, S.; Abdelbaky, M.S.; Garcia-Granda, S.; Essalah, K.; Nasr, C.B.; Mrad, M.L. Crystal Structure, Hirshfeld Surfaces Computational Study and Physicochemical Characterization of the Hybrid Material $(C_7H_{10}N)_2[SnCl_6]\cdot H_2O$. J. Mol. Struct. 2018, 1152, 276-286.

[26] Mathlouthi, M.; Valkonen, A.; Rzaigui, M.; Smirani, W. Structural Characterization, Spectroscopic, Thermal, AC Conductivity and Dielectric Properties and Antimicrobial Studies of $(C_8H_{12}N)_2[SnCl_6]$. Phase Transitions 2017, 90, 399-414.

[27] Tan, Z.; Chu, Y.; Chen, J.; Li, J.; Ji, G.; Niu, G.; Gao, L.; Xiao, Z.; Tang, J. Lead-Free Perovskite Variant Solid Solutions $Cs_2Sn_{1-x}Te_xCl_6$: Bright Luminescence and High Anti-Water Stability. Adv. Mater. 2020, 32, 2002443.

[28] Li, M.; Xia, Z. Recent Progress of Zero-Dimensional Luminescent Metal Halides. Chem. Soc. Rev. 2021, 50 (4), 2626-2662.

[29] Hesse, K.; Gliemann, G. Magnetic Field Effect on the Luminescence of Octahedral Hexachloroselenate (IV). Evidence For the Vibronic Nature of the Low-Temperature Emission. J. Phys. Chem. 1991, 95 (1), 95-98.

[30] Kaatz, T.; Marcovich, M. The Crystal Structure of the Compound Cs_2CeCl_6. Acta Crystallogr. 1966, 21 (6), 1011-1011.

[31] Saeki, K.; Fujimoto, Y.; Koshimizu, M.; Yanagida, T.; Asai, K. Comparative Study of Scintillation Properties of Cs_2HfCl_6 and Cs_2ZrCl_6. Appl. Phys. Express 2016, 9 (4), 042602.

[32] Khan, N.; Prishchenko, D.; Skourski, Y.; Mazurenko, V. G.; Tsirlin, A. A. Cubic Symmetry and Magnetic Frustration on the FCC Spin Lattice in K_2IrCl_6. Phys. Rev. B 2019, 99 (14), 144425.

[33] Lin, Z.; Zhang, Y.; Gao, M.; Steele, J. A.; Louisia, S.; Yu, S.; Quan, L. N.; Lin, C.-K.; Limmer, D. T.; Yang, P. Kinetics of Moisture-Induced Phase Transformation in Inorganic Halide Perovskite. Matter 2021, 4, 2392-2402.

[34] Goldschmidt, V. M. Die Gesetze der Krystallochemie. Naturwissenschaften 1926, 14, 477-485.

[35] Vogler, A.; Nikol, H. The Structures of s^2 Metal Complexes in the Ground and sp Excited States. Comments Inorg. Chem. 1993, 14, 245-261.

[36] Yin, H.; Jin, Y.; Hertzog, J. E.; Mullane, K. C.; Carroll, P. J.; Manor, B. C.; Anna, J. M.; Schelter, E. J. The Hexachlorocerate(III) Anion: A Potent, Benchtop Stable, and Readily Available Ultraviolet A Photosensitizer for Aryl Chlorides. J. Am. Chem. Soc. 2016, 138, 16266-16273.

[37] Machmer, P. On the Correlation of ^{35}Cl Nuclear Quadrupole Coupling Constants with $\pi \rightarrow \gamma 3$ and $\pi \rightarrow \gamma 5$ Optical Electron Transfer Bands of Transition Metal Complexes and its Significance in Pi-Bonding. Z. Naturforsch. B. 1969, 24 (2), 193-199.

[38] Boyer-Richard, S.; Katan, C.; Traore, B.; Scholz, R.; Jancu, J.-M.; Even, J. Symmetry-Based Tight Binding Modeling of Halide Perovskite Semiconductors. J. Phys. Chem. Lett. 2016, 7, 3833-3840.

[39] Biswas, A.; Bakthavatsalam, R.; Bahadur, V.; Biswas, C.; Mali, B. P.; Raavi, S. S. K.; Gonnade, R. G.; Kundu, J. Lead-Free Zero Dimensional Tellurium(IV) Chloride-Organic Hybrid with Strong Room Temperature Emission as a Luminescent Material. J. Mater. Chem. C 2021, 9 (12), 4351-4358.

[40] Steele, J. A.; Puech, P.; Keshavarz, M.; Yang, R.; Banerjee, S.; Debroye, E.; Kim, C. W.; Yuan, H.; Heo, N. H.; Vanacken, J.; Walsh, A.; Hofkens, J.; Roeffaers, M. B. J. Giant Electron-Phonon Coupling and Deep Conduction Band Resonance in Metal Halide Double Perovskite. ACS Nano 2018, 12, 8081-8090.

[41] Madarasz, J; Leskela, T; Pokol, G; Niinisto, L. Thermally induced changes in the oxidation state of cerium (IV). A study of carbonate and chloro complexes. J Therm Anal Calorim. 49, 1347-55 (1997d).

[42] CrysAlisPro 1.171.39.45f.

[43] Dolomanov, O. v; Bourhis, L. J.; Gildea, R. J.; Howard, J. A. K.; Puschmann, H. OLEX2: a complete structure solution, refinement and analysis program. J. Appl. Crystallogr. 42 (2), 339-341 (2009).

[44] Sheldrick, G. M. SHELXT - Integrated space-group and crystal-structure determination. Acta Crystallogr. A 71 (1), 3-8 (2015).

[45] Sheldrick, G. M. Crystal structure refinement with SHELXL. Acta Crystallogr. C 71 (1), 3-8 (2015).

Chapter 3 Supramolecular Assembly of Halide Perovskite Blue and Green Emitters with Near-Unity Photoluminescence

Parts of the content of this chapter were reprinted and adapted from the following publications with permission: Cheng Zhu, Jianbo Jin, Zhen Wang, Zhenpeng Xu, Maria C. Folgueras, Yuxin Jiang, Can B. Uzundal, Han K. D. Le, Feng Wang, Xiaoyu Zheng, and Peidong Yang. "Supramolecular assembly of blue and green halide perovskites with near-unity photoluminescence." Science, 2024, 383, 86-93. Reprinted with permission from AAAS.

3.1 Introduction

Blue and green emission with high photoluminescence quantum yield (PLQY) is at the forefront of solid-state lighting and color display research, and promising candidates have emerged. Inorganic semiconductors[1-4], such as epitaxial-grown GaN films, were developed and led to the 2014 Nobel Prize in Physics[5]. For instance, Si and Zn co-doped GaN can exhibit a PLQY of 90%[6]. Nevertheless, those covalent semiconductors require high purity to prevent the rapid non-radiative recombination through various crystal structure defects[1-4] and rely on solid-state synthesis at elevated temperatures near 1000°C[7]. As an alternative to covalent semiconductors, ionic halide perovskites have received much attention owing to their impressive optoelectronic properties, such as a high optical absorption coefficient[8], tunable bandgap[9-11], high defect tolerance[12,13], and efficient photo/electroluminescence[14,15]. For example, the blue and green emissive colloidal $CsPbCl_xBr_{3-x}$ quantum dots have shown PLQY values around 80%[16,17]. In addition, low-dimensional halide perovskites like the Ruddlesden-Popper phase $(C_6H_5CH_2NH_3)_2PbBr_4$ show a blue emission with a PLQY of 79%[18]. Despite the remarkable optoelectronic properties of lead-based halide perovskites, the toxicity of lead and the complex colloidal synthesis complicate their large-scale real-world applications. Moreover, suitable ligands are still being explored to prevent those low-dimensional nanostructures from aggregating during usage[19]. However, recent studies have revealed that the fascinating optoelectronic properties of halide perovskites stem from the $[MX_6]^{n-}$ (M = metal cation, X = halide anion) fundamental building blocks in the crystal structure[20-22], and given the ionic nature and high chemical tunability of halide perovskite structures[23], a vast array of different compositions and packing geometries of $[MX_6]^{n-}$ can be explored as candidates for future light-emission applications.

Exploring along this direction, a few $[MX_6]^{n-}$ octahedral complexes have been discovered to possess high PLQY when surrounded and charge-balanced by organic or inorganic cations in the crystal structure. For instance, $(C_4N_2H_{14}Br)_4SnBr_6$ and $(C_4N_2H_{14}I)_4SnI_6$ exhibit a yellow emission with ~95% and ~75% PLQY, respectively[24]. Sb^{3+} doped Rb_3InCl_6 has a bluish-green emission with ~90% PLQY[25], and $(C_{11}H_{13}N_2)_3SbCl_6$ has a green emission with ~87% PLQY[26]. However, emission of high PLQY with shorter wavelengths are still very rare. The isolated nature of the octahedra introduce strong coupling of the exciton with lattice vibrations, which will greatly lower the energy level of the exciton, forcing it into transient self-trapped exciton (STE) states with a range of self-trapped energy levels[27,28]. As a result, materials systems with isolated $[MX_6]^{n-}$ octahedral complexes generally have a broadband emission with

a large Stokes shift, making it more challenging to create blue and green emissions with near-unity PLQY.

Octahedra with Hf^{4+}/Zr^{4+} centers, especially $[HfBr_6]^{2-}$ and $[ZrBr_6]^{2-}$ octahedra, have rarely been the subject of research[29,30], even though they are promising for highly emissive blue and green emitters. Cs_2HfBr_6 crystals have a blue emission with the PL peak at 435 nm[29], and colloidal Cs_2ZrBr_6 nanocrystals have been demonstrated to have a green emission with a PLQY of 45%[30]. The reasons why they are less explored are mainly the following: 1) it has been shown theoretically[31] and experimentally[32] that the Hf^{4+} and Zr^{4+} metal centers are extremely air/moisture-sensitive in the A_2MX_6 phase; 2) they can only be synthesized via the vertical Bridgman-Stockbarger method at ~1000°C in sealed quartz ampoules[30,33,34]; and 3) it is very challenging to achieve high-purity samples without a secondary impurity (such as CsBr)[30]. A new methodology to enable the formation of more stabilized and purer solid phases containing the $[Hf/ZrBr_6]^{2-}$ octahedra is of high interest to further explore their promising light-emitting properties.

As we introduced in **Chapter 2.2**, we proposed a general crown ether-assisted supramolecular assembly approach for tetravalent metal octahedra[35]. Two crown ether@alkali metal complexes can readily sandwich a tetravalent metal octahedron in solution into a unique (crown ether@A)$_2MX_6$ dumbbell structural unit. The composition of the dumbbell structural unit is proven to be highly tunable as we discussed in **Chapter 2.3**, with crown ether = 18-Crown-6 (18C6), 21-Crown-7 (21C7); A = Cs^+, Rb^+, K^+; M = Te^{4+}, Sn^{4+}, Se^{4+}, Ir^{4+}, Pt^{4+}, Zr^{4+}, Ce^{4+}; X = Cl^-, Br^-, I^-. The facile solution-based synthesis and high compositional tunability of the supramolecular approach enables us to access the promising optoelectronic properties of Hf and Zr centered octahedra.

In this work, we discover that a new structure with formula $(18C6@K)_2HfBr_6$ features high-purity blue emission with a near-unity (96.22%) PLQY. Moreover, an efficient green emission can also be achieved due to the large composition tunability of the (crown ether@A)$_2MX_6$ dumbbell structural unit. $(18C6@K)_2ZrCl_4Br_2$ demonstrates green emission with 82.69% PLQY. The chemical tunability has also been tested by partially substituting the $[HfBr_6]^{2-}$ octahedra by $[ZrBr_6]^{2-}$ octahedra in the structure with precise Zr/Hf molar ratio control. We have discovered that 6% Zr^{4+} doped $(18C6@K)_2HfBr_6$ powders demonstrate a bright green emission with a PLQY value of 51.41%. By studying the photophysics of the supramolecular assembled samples, we have proved that the emission is attributed to STE emission, and a very strong electron-phonon coupling constant (represented by the Huang-Rhys parameter) over 90 is identified in $(18C6@K)_2HfBr_6$. Besides, the supramolecular assembled samples have significantly longer PL lifetimes (in the microsecond timescale) compared to other halide perovskite systems, signifying a low rate of nonradiative recombination. The $(18C6@K)_2ZrCl_4Br_2$ green emitter also exhibit excitation wavelength dependent PL emission. The Zr^{4+} doped $(18C6@K)_2HfBr_6$ compositions enable the study of the energy transfer between various octahedra in the supramolecular assembled crystal structure. We discovered that the emission is most likely a combination of (1) intrinsic $[HfBr_6]^{2-}$ and $[ZrBr_6]^{2-}$ emission and (2) Förster resonance energy transfer from $[HfBr_6]^{2-}$ to lower energy $[ZrBr_6]^{2-}$. The supramolecular assembled solid powders also have a wide range of light-emitting applications. The structural integrity and impressive optical properties of the supramolecular assembled solid powders can be further maintained by generating a powder suspension in a non-polar organic solvent such as dichloromethane (DCM), thus creating an ink system. Polystyrene (PS) polymer is dissolved

into the ink to further increase the solution processability. We have demonstrated that the inks can be utilized for thin film fabrication upon the fast evaporation of DCM solvent. Excitingly, with a digitally controlled excitation source, the $(18C6@K)_2HfBr_6$/PS composite thin film becomes a display with bright color and fast response time. Moreover, starting from a solution processable ink, the powders can be 3D-printed into various light-emitting architectures. Not only blue and green emitting structures can be achieved, but the microstructures can demonstrate dual-color emission with precise control.

3.2 Supramolecular Assembly of Hf and Zr Octahedral Complexes

A new solution-based supramolecular synthetic route has been explored for $[HfBr_6]^{2-}$ octahedra. 18C6 can greatly increase the solubility of the KBr and $HfBr_4$ precursors in polar organic solvents, making facile low-temperature solution-based synthesis accessible. A clear precursor solution can be obtained using acetonitrile (ACN) as the solvent at 80°C. According to our previous study about the supramolecular assembly process of tetravalent metal octahedra[35], a unique $(18C6@K)_2HfBr_6$ dumbbell structural unit is formed in the ACN solution. $(18C6@K)_2HfBr_6$ powders and single crystals are grown using the anti-solvent crystallization method. The all-inorganic K_2HfBr_6 powders are also synthesized using a modified solid-state synthesis method for future comparison. We increase the purity and decrease the synthesis temperature to 500°C by combining mechanical forces with heat to facilitate solid-state diffusion. Details of the synthesis for $(18C6@K)_2HfBr_6$ and K_2HfBr_6 can be found in the **Chapter 3.5**.

$(18C6@K)_2HfBr_6$ single crystals have a parallelepiped shape, and up to a few tens of micrometers in all three dimensions, as shown under the bright-field optical microscope (**Figure 3.1a**). The crystal structure and composition of $(18C6@K)_2HfBr_6$ is determined from single crystal X-ray diffraction (SCXRD) experiments. $(18C6@K)_2HfBr_6$ crystallizes in the R-3 space group with lattice parameters of a = 14.1332 Å and c = 21.0189 Å (**Figure 3.1b**, **Table 3.1**). The $(18C6@K)_2HfBr_6$ dumbbell structural unit belongs to the S_6 point group, where two K^+ cations and the Hf^{4+} cation sit on the S_6 axis. The six-fold symmetry of the 18C6 and the S_6 axis of O_h-symmetric $[HfBr_6]^{2-}$ octahedron are perfectly aligned (**Figure 3.1c**). The separation of the first-nearest-neighbor octahedra is 10.7550 Å. The crystal structure of K_2HfBr_6 is found to be face-centered cubic (FCC) (**Figure 3.2a**)[36,37], same to the other reported $Cs_2M(IV)X_6$ vacancy-ordered double perovskites, where the $[HfBr_6]^{2-}$ ionic octahedra are charge balanced by the surrounding K^+ cations (**Figure 3.2b**). The purity of the $(18C6@K)_2HfBr_6$ and K_2HfBr_6 powders are investigated using powder X-ray diffraction (PXRD) (**Figure 3.3**). The PXRD pattern of the $(18C6@K)_2HfBr_6$ powders matches perfectly with the calculated pattern generated from the single crystal structure, suggesting that the powders are a pure-phase system, with no visible extra diffraction peaks. The quality of the PXRD pattern for the K_2HfBr_6 powders is much poorer due to their extreme air-sensitivity. The measurement must be collected in 5 minutes in an inert atmosphere sample holder to prevent the degradation of the powders and measurement of the degradation product. Even if the quality of the K_2HfBr_6 PXRD pattern is not ideal, the most dominant peaks of the FCC K_2HfBr_6 phase are still identifiable. Moreover, no $HfBr_4$ or KBr diffraction peaks are present (**Figure 3.3**), proving that all the precursors are transformed into the K_2HfBr_6 phase. Raman spectrum of K_2HfBr_6 further confirms the presence of the $[HfBr_6]^{2-}$ octahedra in the crystal structure (**Figure 3.4**). The crown-ether assisted

supramolecular approach enable much more facile synthesis of the $[HfBr_6]^{2-}$ octahedra with higher purity.

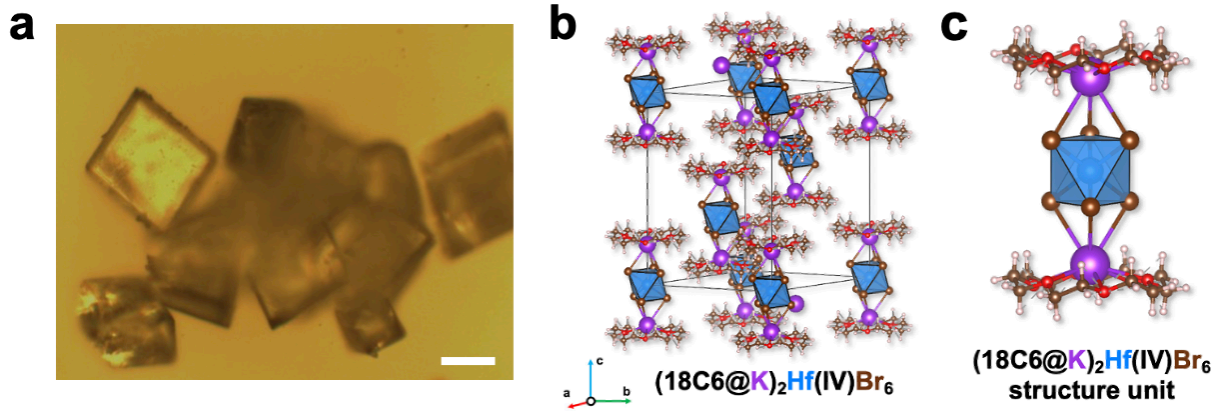

Figure 3.1. $(18C6@K)_2HfBr_6$ single crystals. (a) Bright-field optical microscope imaging of $(18C6@K)_2HfBr_6$ single crystals. The scale bar is 20 μm. (b) The rhombohedral unit cell and (c) the dumbbell-shaped structure unit of $(18C6@K)_2HfBr_6$.

Table 3.1. Crystallographic tables for $(18C6@K)_2HfBr_6$ and $(18C6@K)_2ZrBr_6$.

Crystal	**$(18C6@K)_2HfBr_6$**	**$(18C6@K)_2ZrBr_6$**
ICSD Number	2225998	2225999
Empirical formula	$C_{24}H_{48}Br_6K_2O_{12}Hf$	$C_{24}H_{48}Br_6K_2O_{12}Zr$
Formula weight	1264.77	1177.50
Temperature/K	293(2)	293(2)
Crystal system	trigonal	trigonal
Space group	R-3	R-3
a/Å	14.13320(10)	14.13940(10)
b/Å	14.13320(10)	14.13940(10)
c/Å	21.0819(2)	21.0727(2)
α/°	90	90
β/°	90	90
γ/°	120	120
Volume/Å^3	3635.98(6)	3648.49(6)
Z	3	3
ρ_{calc}mg/mm^3	1.733	1.608
μ/mm^{-1}	11.670	9.517
F(000)	1824.0	1728.0
Crystal size/mm^3	0.15 × 0.12 × 0.108	0.09 × 0.07 × 0.06
Radiation	Cu Kα (λ = 1.54184 Å)	Cu Kα (λ = 1.54184 Å)
2Θ range for data collection	12.526 to 157.206°	8.325 to 157.42°

Index ranges	$-17 \leq h \leq 17, -17 \leq k \leq 17, -24 \leq l \leq 26$	$-17 \leq h \leq 17, -17 \leq k \leq 17, -25 \leq l \leq 26$
Reflections collected	26285	26501
Independent reflections	1737[R(int) = 0.0268]	1753[R(int) = 0.0387]
Data/restraints/parameters	1737/0/70	1753/0/70
Goodness-of-fit on F^2	1.103	1.106
Final R indexes [I>=2σ (I)]	$R_1 = 0.0171$, $wR_2 = 0.0496$	$R_1 = 0.0183$, $wR_2 = 0.0500$
Final R indexes [all data]	$R_1 = 0.0171$, $wR_2 = 0.0496$	$R_1 = 0.0183$, $wR_2 = 0.0503$
Largest diff. peak/hole/e $Å^{-3}$	0.34/-0.43	0.48/-0.26

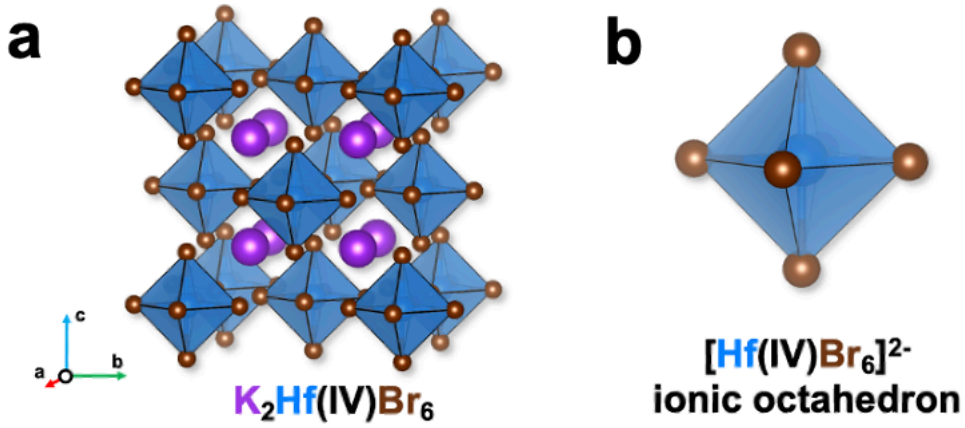

Figure 3.2. K_2HfBr_6 crystal structure. (a) The Fm-3m unit cell (from OQMD database (*36*, *37*)) and (b) the isolated $[HfBr_6]^{2-}$ ionic octahedron building block of K_2HfBr_6.

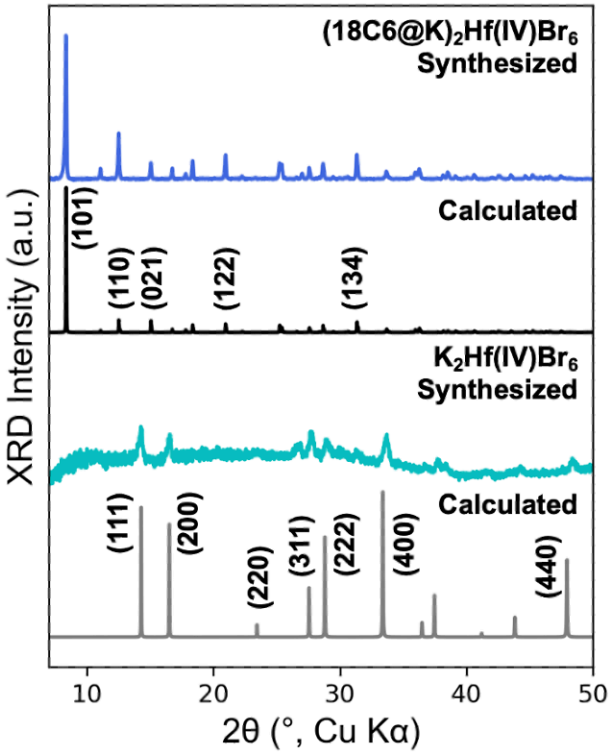

Figure 3.3. The powder X-ray diffraction (PXRD) patterns for synthesized $(18C6@K)_2HfBr_6$ and K_2HfBr_6 powders and the calculated diffraction patterns.

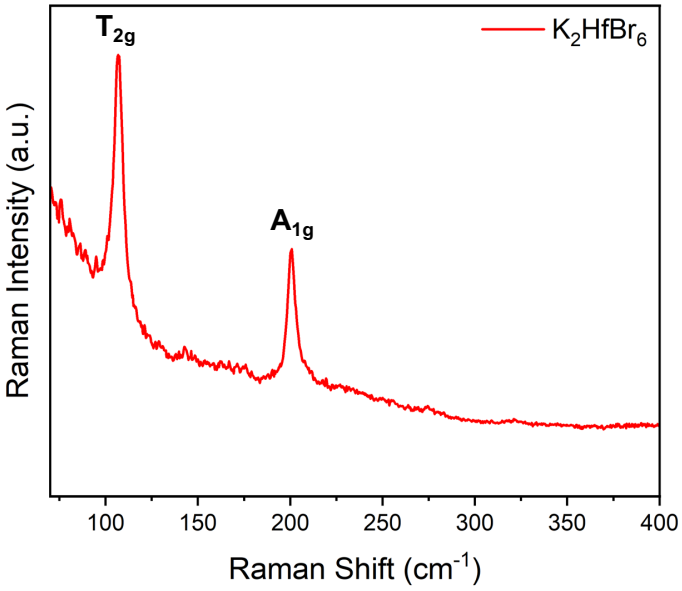

Figure 3.4. Raman spectroscopy of the K_2HfBr_6 powder measured in inert atmosphere. The asymmetric bending mode (T_{2g}) and symmetric stretching mode (A_{1g}) of the O_h-symmetric vibrating $[HfBr_6]^{2-}$ are identified. The baseline appears to be noisy due to the low Raman intensity of the powder sample and the signal loss coming from the cover glass on the inert-atmosphere sample holder.

The crown ether-assisted supramolecular approach can be generalized to other emissive centers. For instance, $(18C6@K)_2ZrBr_6$ single crystals have been successfully synthesized using the same method, and the same crystallographic symmetry as $(18C6@K)_2HfBr_6$ has been achieved according to SCXRD determination (**Figure 3.5**, **Table 3.1**). The size of the $(18C6@K)_2ZrBr_6$ single crystal (**Figure 3.6**) is larger than its Hf counterpart due to larger solubility of the $ZrBr_4$ precursor in ACN. Extremely phase pure $(18C6@K)_2ZrBr_6$ powders can also be obtained according to PXRD (**Figure 3.7**). For later optical properties comparison, K_2ZrBr_6 powders are also synthesized using the same solid-state methods as K_2HfBr_6.

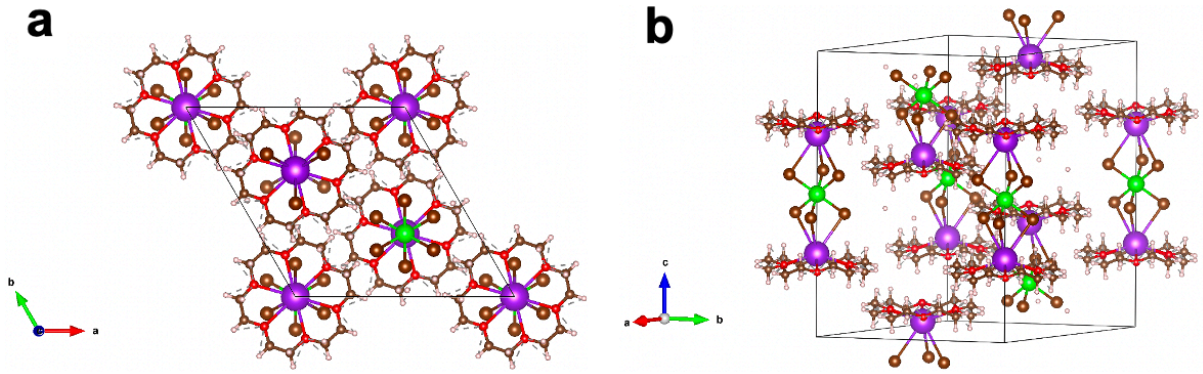

Figure 3.5. Crystal structure of $(18C6@K)_2ZrBr_6$ determined by single crystal X-ray diffraction. (a) The unit cell viewed along the c axis direction. (b) The unit cell viewed along the direction perpendicular to the c axis.

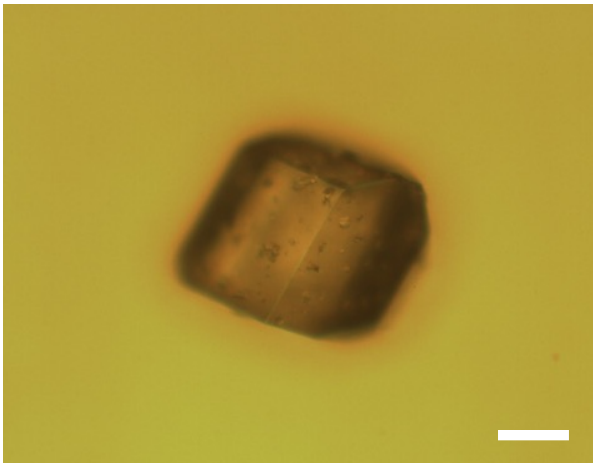

Figure 3.6. Bright-field optical microscope imaging of a $(18C6@K)_2ZrBr_6$ single crystal. The scale bar is 100 μm.

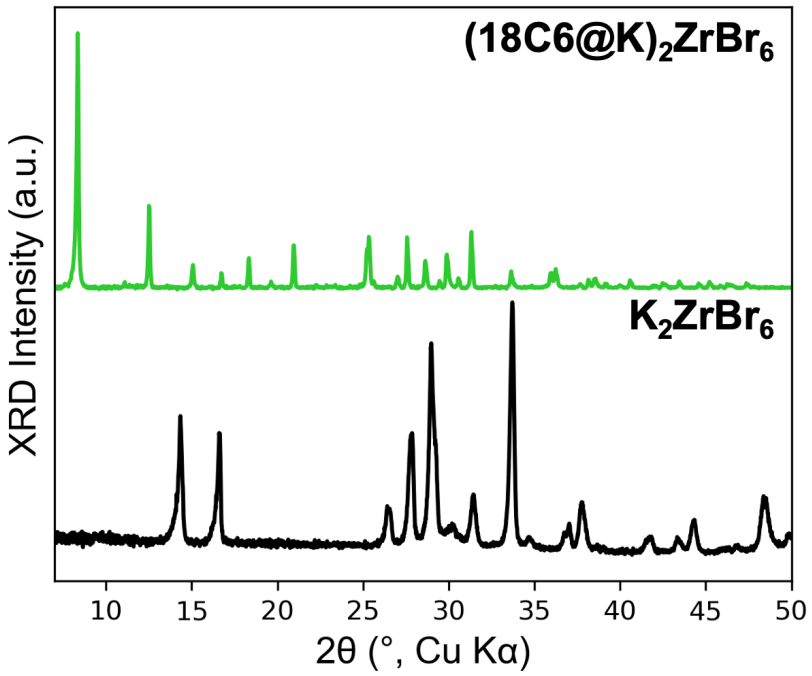

Figure 3.7. Normalized PXRD patterns of $(18C6@K)_2ZrBr_6$ and K_2ZrBr_6 powders.

The $(18C6@K)_2Hf/ZrBr_6$ dumbbell building blocks are not only the structural units but also the electronic units of the new crystal. To elucidate the effect of 18C6 on the electronic structures of the assembled $[HfBr_6]^{2-}$ octahedra, density functional theory (DFT) calculations are performed on $(18C6@K)_2HfBr_6$ (**Figure 3.8a**) and K_2HfBr_6 (**Figure 3.8b**) for their electronic band structures and the partial electronic density of states (pDOS). As a comparison, the electronic bands of $(18C6@K)_2HfBr_6$ are less dispersive compared to K_2HfBr_6 due to the $[HfBr_6]^{2-}$ octahedra being more separated in $(18C6@K)_2HfBr_6$. The conduction band (CB) of $(18C6@K)_2HfBr_6$ is composed of Hf 5d and Br 4p orbitals, as is the CB of K_2HfBr_6. However, the valence band (VB) compositions are quite different in these two materials. The VB of K_2HfBr_6 is mainly composed of the Br 4p orbital, but 18C6 contributes significantly to the VB of $(18C6@K)_2HfBr_6$. This demonstrates that the 18C6 molecules are electronically correlated to the $[HfBr_6]^{2-}$ octahedra, indicating that the entire $(18C6@K)_2HfBr_6$ dumbbell building block is the new electronic unit. DFT calculations of $(18C6@K)_2ZrBr_6$ show the contribution from 18C6 to the VB and that the band structures are more discrete than K_2ZrBr_6 (**Figure 3.9**).

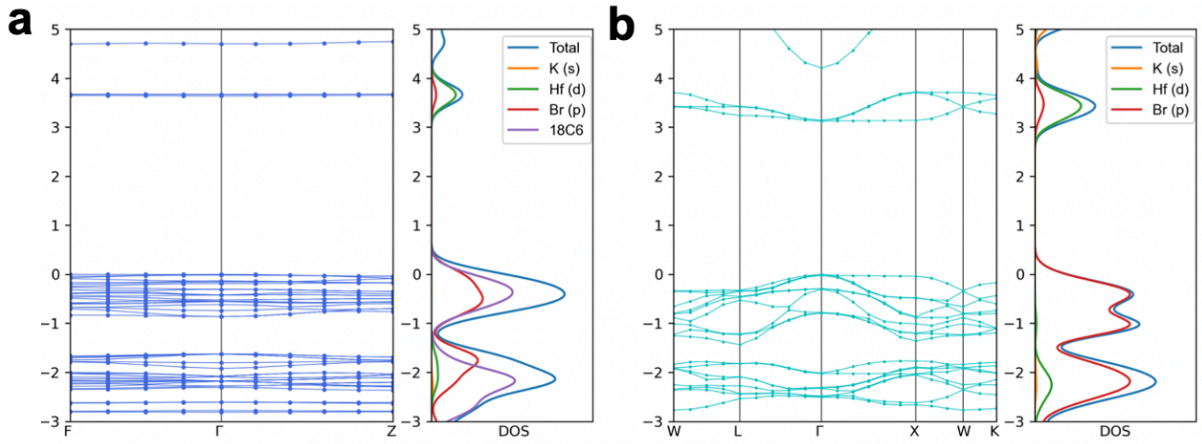

Figure 3.8. Band structure and corresponding total partial density of states (pDOS) of (a) $(18C6@K)_2HfBr_6$ and (b) K_2HfBr_6. When $[HfBr_6]^{2-}$ octahedra are assembled in the supramolecular approach, the dispersion of the bands decreases and 18C6 contributes significantly to the valence band.

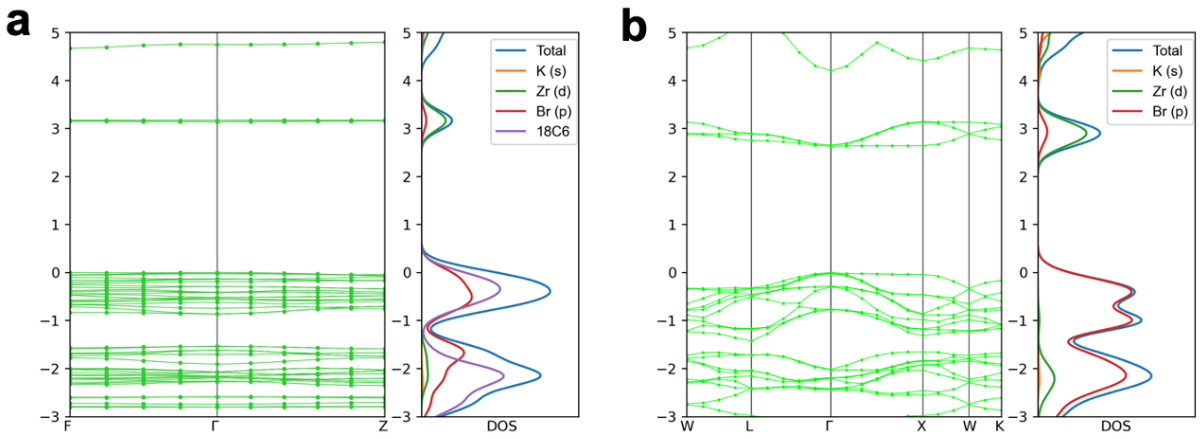

Figure 3.9. Band structure and corresponding total partial density of states (pDOS) of (a) $(18C6@K)_2ZrBr_6$ and (b) K_2ZrBr_6.

3.3 Optical Observations and Study

Compared to K_2HfBr_6, $(18C6@K)_2HfBr_6$ features greatly enhanced emission intensity. **Figure 3.10a** shows the extremely bright blue emission of $(18C6@K)_2HfBr_6$ powders under 254 nm UV lamp excitation. The photoluminescence (PL) spectrum of $(18C6@K)_2HfBr_6$ powders is measured at 275 nm excitation (**Figure 3.10b**). The powders have a blue emission centered at 445 nm. The full width at half maximum (FWHM) of the emission is 0.73 eV. According to the photoluminescence excitation (PLE) spectrum, the emission features a large Stokes shift (1.35 eV). To quantify the emission intensity of the $(18C6@K)_2HfBr_6$ powders, PLQY measurements are conducted. A near-unity PLQY value of 96.22% is observed for the $(18C6@K)_2HfBr_6$ powders over 6 measurements from 2 different batches of samples. The

specific value for each measurement is illustrated in **Table 3.2**. In contrast, the PLQY for K_2HfBr_6 is much lower at 12.79%, making it less appealing for blue emission applications. Furthermore, the color purity of the emission from the $[HfBr_6]^{2-}$ octahedra is also enhanced by the supramolecular approach. K_2HfBr_6 has an even larger Stokes shift and broader emission, with peak emission wavelength of 457 nm and a FWHM of 0.90 eV (**Figure 3.11**). **Figure 3.12** shows the emission color of $(18C6@K)_2HfBr_6$ and K_2HfBr_6 powders on the CIE 1931 chromaticity diagram. $(18C6@K)_2HfBr_6$ has a much purer emission color than K_2HfBr_6, which makes it more preferable for display applications.

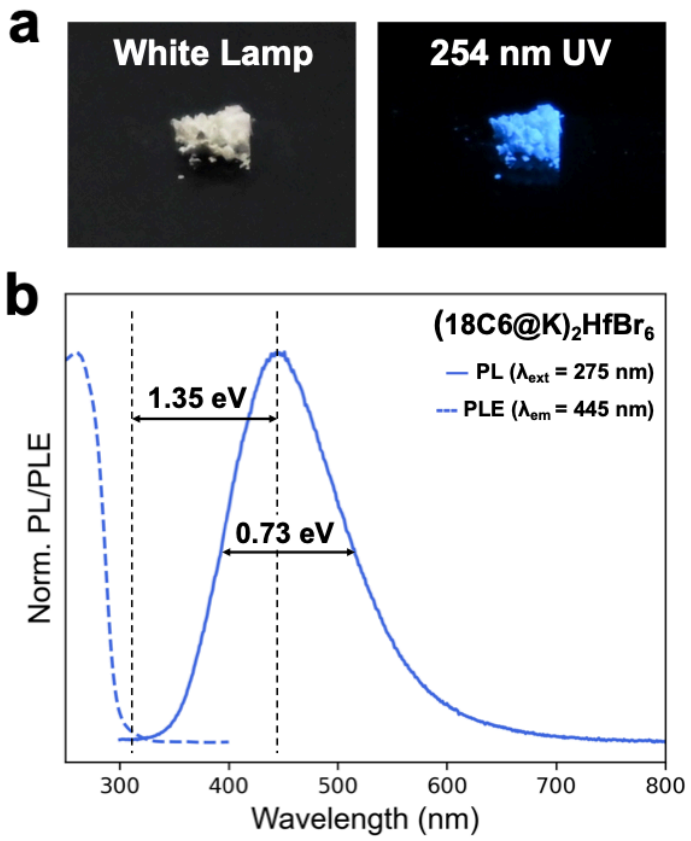

Figure 3.10. Blue emission with near-unity PLQY (96.22%) from $(18C6@K)_2HfBr_6$ powders. (a) $(18C6@K)_2HfBr_6$ powders under white lamp and 254 nm UV lamp excitation. (b) PL and PLE spectra of $(18C6@K)_2HfBr_6$ powders with 275 nm excitation.

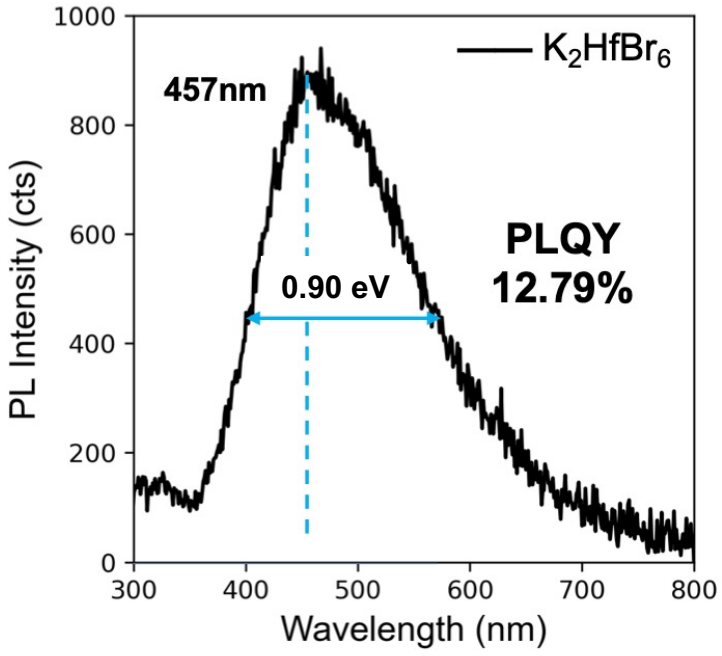

Figure 3.11. PL spectrum of K_2HfBr_6 powder with 275 nm excitation. The spectrum appears to be noisy due to the poor stability of K_2HfBr_6 powder in the air, and the therefore high measuring speed.

Table 3.2. A summary of the photoluminescence quantum yield (PLQY) determination results of two different batches and three measurements per batch of the $(18C6@K)_2HfBr_6$ powders.

	Measurement 1	Measurement 2	Measurement 3	Average
Batch 1	97.31%	97.57%	100.67%	98.52%
Batch 2	93.46%	94.89%	93.38%	93.91%

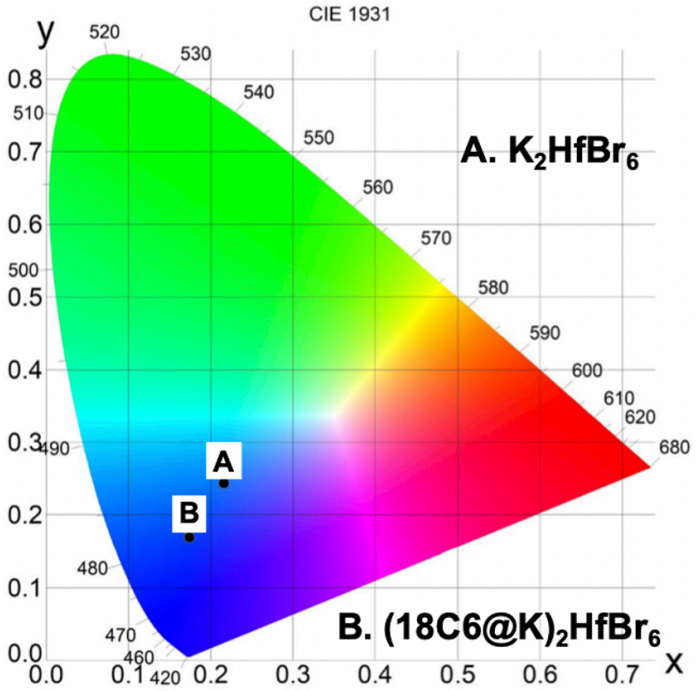

Figure 3.12. The CIE 1931 chromaticity diagram for the emissions of K_2HfBr_6 powder and $(18C6@K)_2HfBr_6$ powder. The coordinates for the emission color of K_2HfBr_6 are (0.21603, 0.24368), and the coordinates for the emission color of $(18C6@K)_2HfBr_6$ are (0.17438, 0.16922).

The supramolecular approach can render high PLQY for $[ZrBr_6]^{2-}$ units as well. Upon 290 nm excitation, $(18C6@K)_2ZrBr_6$ has a PL peak emission wavelength of 547 nm and a FWHM of 0.69 eV (**Figure 3.13a**). As a comparison, using the same excitation wavelength, the PL peak emission wavelength of K_2ZrBr_6 is at 560 nm, and the FWHM is 0.70 eV (**Figure 3.13b**). The PLQY of $(18C6@K)_2ZrBr_6$ is 49.75%, which is slightly enhanced compared to the PLQY of K_2ZrBr_6 (46.31%). Although the peak position of the PL spectrum is in the green region, simply analyzing the peak emission wavelength is not enough given the broadness of the STE-based emission, which really produces a yellow-green emission color (**Figure 3.14**).

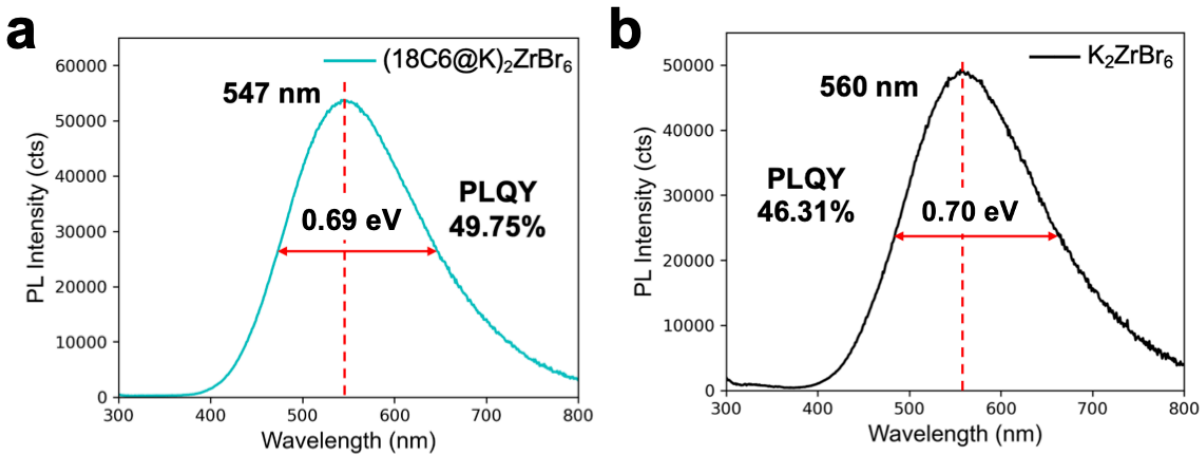

Figure 3.13. PL spectrum of (a) $(18C6@K)_2ZrBr_6$ powder with 290 nm excitation and (b) K_2ZrBr_6 powder with 290 nm excitation.

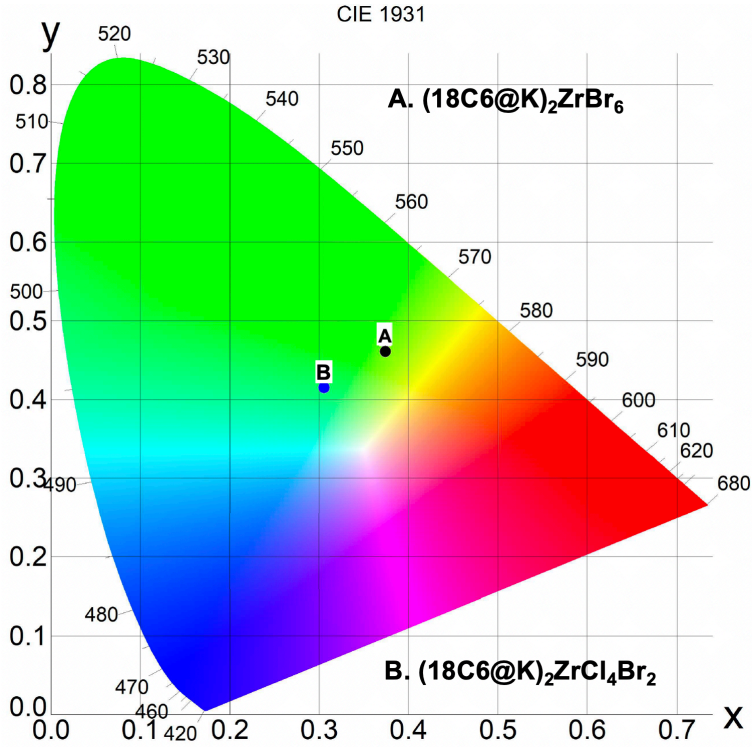

Figure 3.14. The CIE 1931 chromaticity diagram for the emissions of $(18C6@K)_2ZrBr_6$ powder and $(18C6@K)_2ZrCl_4Br_2$ powder. The coordinates for the emission color of $(18C6@K)_2ZrBr_6$ powder are (0.37601, 0.45927), and the coordinates for the emission color of $(18C6@K)_2ZrCl_4Br_2$ powder are (0.30597, 0.41533).

Given the great chemical tunability of the dumbbell structural unit, an alloying approach at the halide site is proposed to achieve a purer green emission with near-unity PLQY emission. It has been demonstrated that for $CsPbX_3$ (X = Cl, Br, I) nanocrystals that the PL color is easily

controllable by tuning the halide composition[38] and introducing Cl^- in the halide site may generate a shorter wavelength emission color. By carefully tuning the KCl/KBr and $ZrCl_4/ZrBr_4$ precursor ratio in the synthesis, the Cl/Br ratio in the obtained $(18C6@K)_2ZrX_6$ dumbbell structural unit can be precisely controlled. As expected, a larger Cl/Br ratio creates a more blue-shifted PL (**Figure 3.15**). For example, $(18C6@K)_2ZrCl_3Br_3$ and $(18C6@K)_2ZrCl_4Br_2$ have green emissions with PL centered at 534 nm and 530 nm, respectively. Continue increasing the Cl content to a composition of $(18C6@K)_2ZrCl_{4.5}Br_{1.5}$ starts to push the PL color to the cyan (bluish-green) color. The established halide-site alloying approach can not only generate a purer green emission color, but also boost the PLQY of the emission to near-unity. By increasing the Cl/Br ratio from 1:1 to 2:1 to 3:1, the PLQYs of their emissions are 69.14%, 82.69%, and 86.95%, respectively. Since the 2:1 Cl/Br ratio composition has both pure-green emission color and high PLQY, the composition of $(18C6@K)_2ZrCl_4Br_2$ was selected as the focus for the green emission.

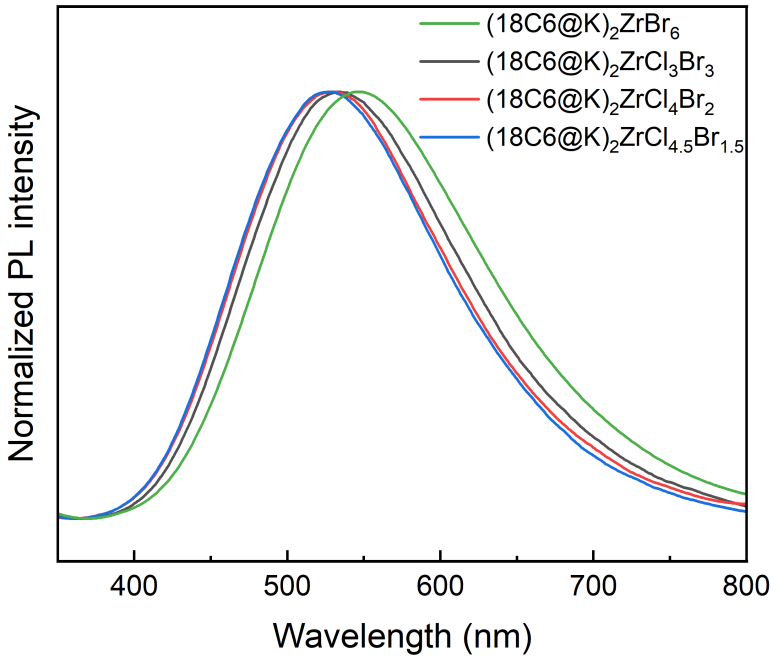

Figure 3.15. Normalized PL spectra of different Cl/Br ratio $(18C6@K)_2ZrCl_xBr_{6-x}$ powders.

$(18C6@K)_2ZrCl_4Br_2$ single crystals (**Figure 3.16a**) can be synthesized by controlling the Cl/Br precursor ratio to be 2:1. The formula of $(18C6@K)_2ZrCl_4Br_2$ has been proved by SCXRD (Cl:Br = 4.3:1.7, **Figure 3.16b, c**, **Table 3.3**) and EDX elemental mapping (Cl:Br = 4.1:1.9), and the Cl and Br atoms are proved to be perfectly miscible in the crystal structure (**Figure 3.17**). PXRD of the $(18C6@K)_2ZrCl_4Br_2$ powder (**Figure 3.18a**) also indicates the alloying composition is a phase-pure system. The (101) and (110) diffraction peaks of $(18C6@K)_2ZrCl_4Br_2$ are slightly shifted to large 2θ values compared to the corresponding PXRD peaks of $(18C6@K)_2ZrBr_6$, suggesting smaller lattice constants (**Figure 3.18b**). **Figure**

3.19a shows the bright green emission of $(18C6@K)_2ZrCl_4Br_2$ powder under 302 nm UV lamp excitation. The PL spectrum of $(18C6@K)_2ZrCl_4Br_2$ powders is measured at 295 nm excitation (**Figure 3.19b**). The green emission has very similar Stokes shift (1.36 eV versus 1.35 eV) and FWHM (0.80 eV versus 0.73 eV) to the blue emission of the $(18C6@K)_2HfBr_6$ powder, suggesting similar emission properties of the Hf and Zr metal centers in the supramolecular assembly materials system. The PLQY of the emission from $(18C6@K)_2ZrCl_4Br_2$ powders is 82.69%, which is determined through the measurement of 4 samples from 2 different batches (**Table 3.4**). Therefore, we have achieved highly emissive powders with blue and green emission colors by the supramolecular assembly approach. The blue and green colors of the emissions from $(18C6@K)_2HfBr_6$ and $(18C6@K)_2ZrCl_4Br_2$, respectively, are summarized in the CIE 1931 diagram (**Figure 3.20**).

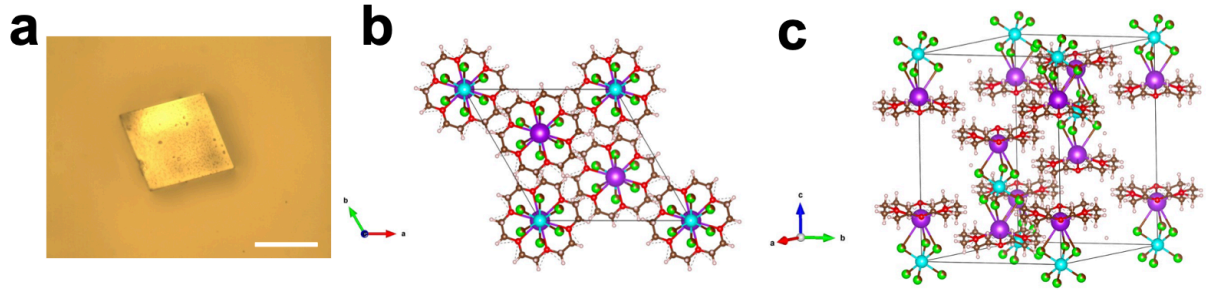

Figure 3.16. $(18C6@K)_2ZrCl_4Br_2$ single crystal. (a) Bright-field optical microscope imaging of a $(18C6@K)_2ZrCl_4Br_2$ single crystal. The scale bar is 100 μm. Crystal structure of $(18C6@K)_2ZrCl_4Br_2$ determined by single crystal X-ray diffraction. (b) The unit cell viewed along the c axis direction. (c) The unit cell viewed along the direction perpendicular to the c axis. The molar ratio of Cl:Br is determined to be 4.3:1.7 according to the electron density calculation.

Table 3.3. Crystallographic tables for $(18C6@K)_2ZrCl_4Br_2$.

Crystal	**$(18C6@K)_2ZrCl_4Br_2$**
ICSD Number	2292758
Empirical formula	$C_{24}H_{48}Cl_{4.3}Br_{1.7}K_2O_{12}Zr$
Formula weight	986.47
Temperature/K	293(2)
Crystal system	trigonal
Space group	R-3
a/Å	14.0091(6)
b/Å	14.0091(6)
c/Å	20.6138(11)
α/°	90
β/°	90
γ/°	120

Volume/Å^3	3503.6(4)
Z	3
ρ_{calc}mg/mm^3	1.403
μ/mm^{-1}	2.159
F(000)	1496.0
Crystal size/mm^3	0.08 × 0.06 × 0.04
Radiation	Mo Kα (λ =0.71073 Å)
2Θ range for data collection	7.002 to 59.562°
Index ranges	-17 ≤ h ≤ 18, -18 ≤ k ≤ 17, -27 ≤ l ≤ 22
Reflections collected	9250
Independent reflections	1973[R(int) = 0.0168]
Data/restraints/parameters	1973/0/70
Goodness-of-fit on F^2	1.086
Final R indexes [I>=2σ (I)]	R_1 = 0.0302, wR_2 = 0.1163
Final R indexes [all data]	R_1 = 0.0334, wR_2 = 0.1180
Largest diff. peak/hole / e Å^{-3}	1.71/-0.39

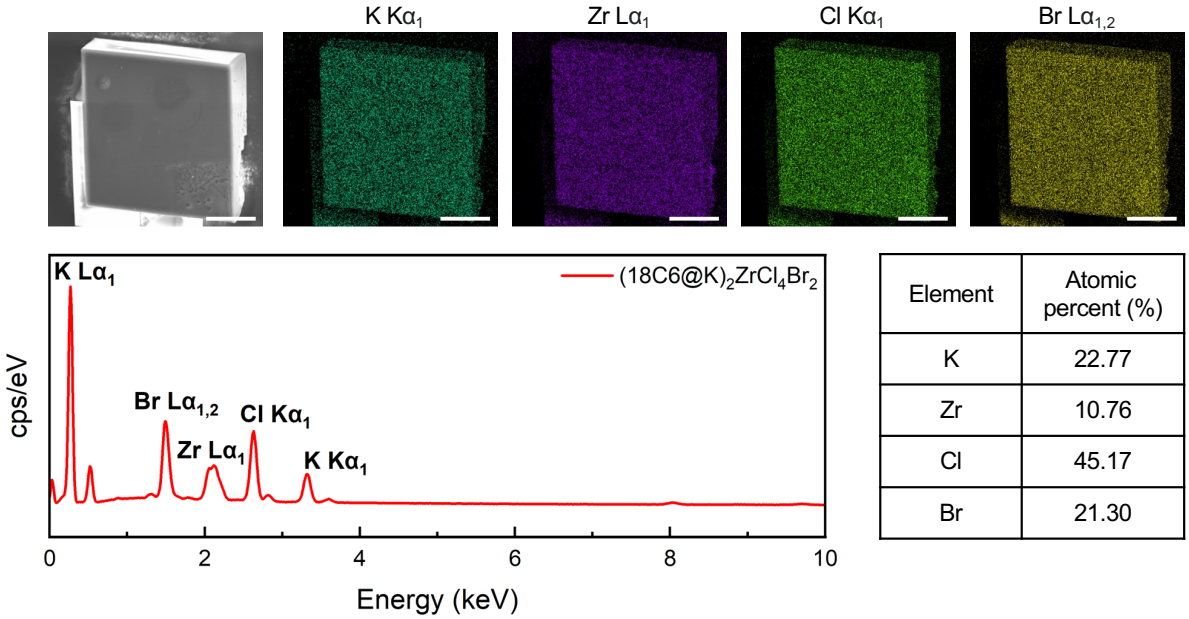

Element	Atomic percent (%)
K	22.77
Zr	10.76
Cl	45.17
Br	21.30

Figure 3.17. SEM-EDX results of a (18C6@K)$_2$ZrCl$_4$Br$_2$ single crystal, including SEM image, EDX elemental mapping, EDX spectrum and the corresponding atomic percentages. The EDX spectrum shows non-overlapping characteristic X-ray signals for K Lα$_1$ (0.260 keV), K Kα$_1$ (3.314 keV), Zr Lα$_1$ (2.042 keV), Cl Kα$_1$ (2.622 keV), Br Lα$_{1,2}$ (1.480 keV). Integration of the K, Zr, Cl, and Br emission lines confirms the atomic ratio of K:Zr:Cl:Br to be approximately 2:1:4:2. The scale bars are 25 μm.

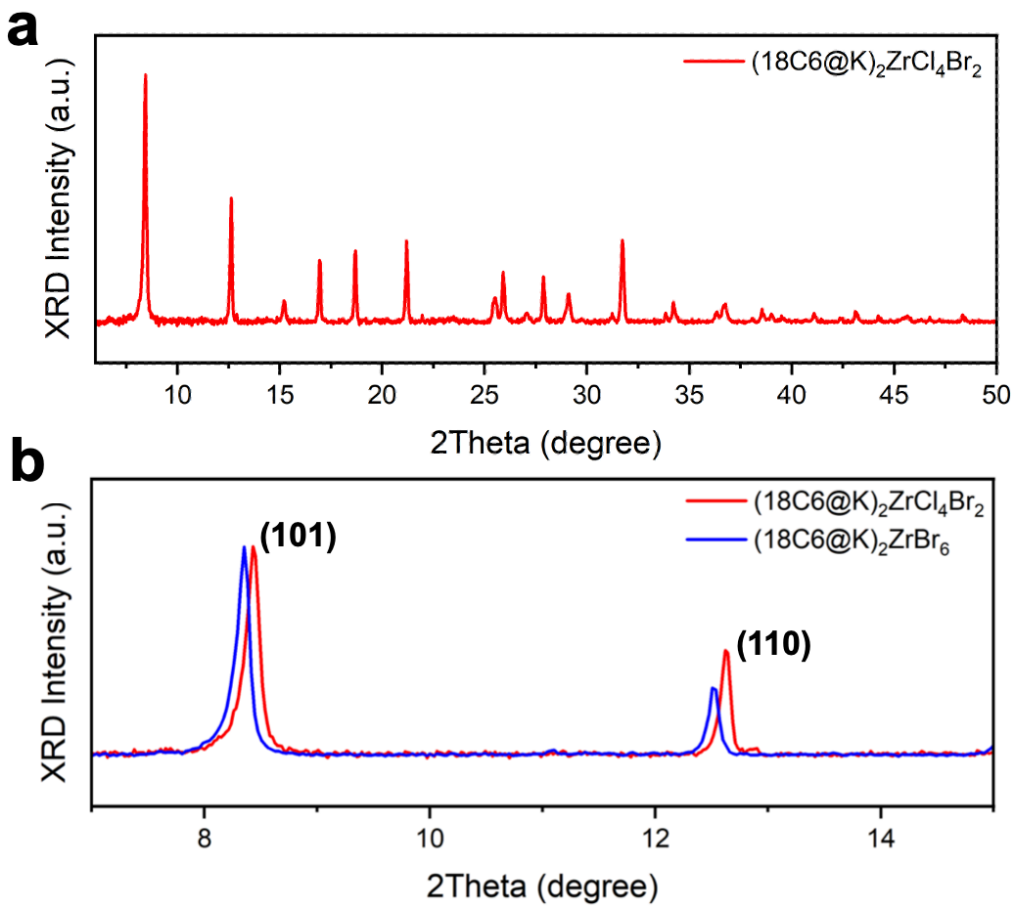

Figure 3.18. (a) PXRD of $(18C6@K)_2ZrCl_4Br_2$ powder. (b) PXRD comparison of $(18C6@K)_2ZrCl_4Br_2$ powder and $(18C6@K)_2ZrBr_6$ powder at 2Theta values between 7 to 15 degrees. Both the (101) and (110) diffraction peaks of $(18C6@K)_2ZrCl_4Br_2$ are shifted to larger degree values.

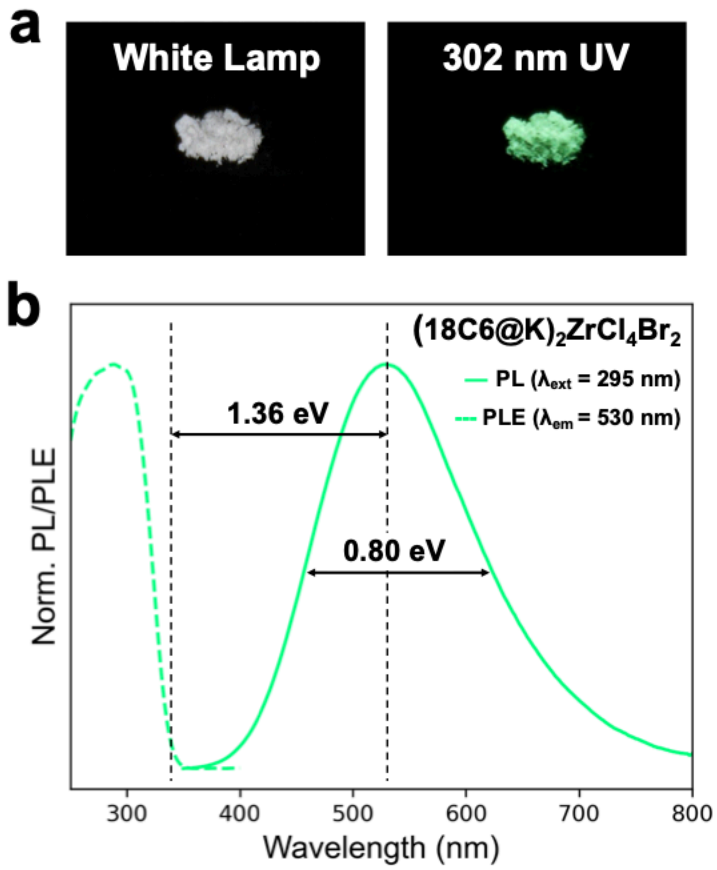

Figure 3.19. Green emission with a PLQY of 82.69% from $(18C6@K)_2ZrCl_4Br_2$ powders. (a) $(18C6@K)_2ZrCl_4Br_2$ powders under white lamp and 302 nm UV lamp excitation. (b) PL and PLE spectra of $(18C6@K)_2ZrCl_4Br_2$ powders with 295 nm excitation.

Table 3.4. A summary of the photoluminescence quantum yield (PLQY) determination results of two different batches and three measurements per batch of the $(18C6@K)_2ZrCl_4Br_2$ powders.

	Measurement 1	Measurement 2	Average
Batch 1	80.29%	82.76%	81.53%
Batch 2	84.92%	82.77%	83.85%

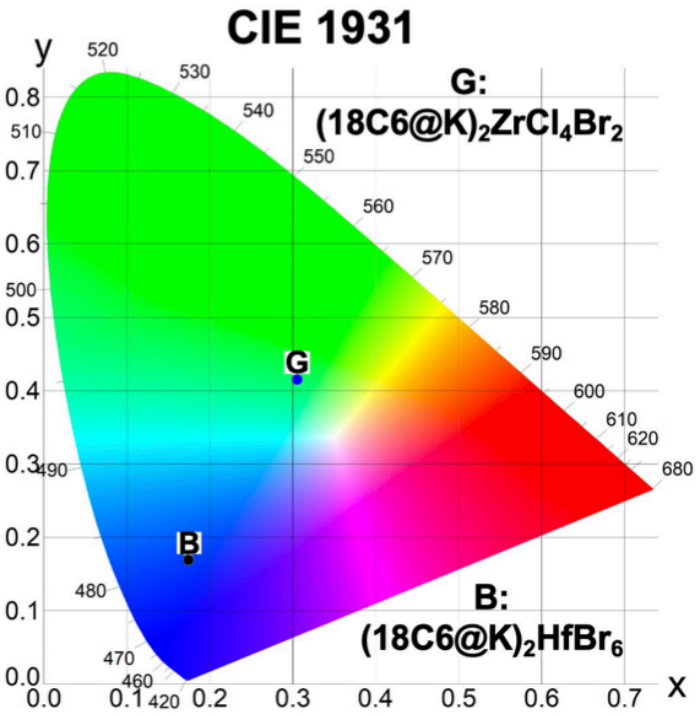

Figure 3.20. The CIE 1931 chromaticity diagram for $(18C6@K)_2HfBr_6$ and $(18C6@K)_2ZrCl_4Br_2$. "B" stands for the blue emission of $(18C6@K)_2HfBr_6$, and "G" stands for the green emission of $(18C6@K)_2ZrCl_4Br_2$.

Apart from the halide-site alloying approach, the high compositional tunability of the dumbbell structural unit promises a second strategy to create purer green emission. Since $(18C6@K)_2HfBr_6$ has an emission at a shorter wavelength, and the FWHM of the emission is smaller than the Zr counterpart, we speculate that a Hf^{4+}/Zr^{4+} alloy version may generate a purer green emission color. By simply mixing the $(18C6@K)_2HfBr_6$ and $(18C6@K)_2ZrBr_6$ precursor solutions prior to crystallization, Zr^{4+} doped $(18C6@K)_2HfBr_6$ powders with a highly controllable molar ratio can be obtained. Inductively coupled plasma atomic emission spectroscopy (ICP-AES) shows that the doping/alloying ratio can be accurately tuned from 6%, 12%, 20%, to 33% by changing the Hf^{4+}/Zr^{4+} ratio in the precursor solution (**Table 3.5**). We confirm that the Zr^{4+} doped $(18C6@K)_2HfBr_6$ structure is a single phase by PXRD (**Figure 3.21a**), and it has very similar lattice parameter to $(18C6@K)_2HfBr_6$ and $(18C6@K)_2ZrBr_6$ (**Figure 3.21b**). Most interestingly, 6% Zr^{4+}: $(18C6@K)_2HfBr_6$ shows a much purer green emission than $(18C6@K)_2ZrBr_6$. The color comparison of the emissions from $(18C6@K)_2ZrBr_6$ and 6% Zr^{4+}: $(18C6@K)_2HfBr_6$ are summarized in the CIE 1931 diagram (**Figure 3.22**). Under the 302 nm UV lamp excitation, the powders show a very bright green emission. The PL peak position (548 nm) remains very close to that of the non-doped $(18C6@K)_2ZrBr_6$ powder (547 nm), but the FWHM is decreased slightly from 0.69 eV in the non-doped version to 0.67 eV in the doped version (**Figure 3.23**). In addition, the PLQY of 6% Zr^{4+}: $(18C6@K)_2HfBr_6$ is slightly increased to 51.41%.

Table 3.5. ICP-AES concentrations of Hf and Zr in the Zr^{4+} doped $(18C6@K)_2HfBr_6$ crystals synthesized from respective Hf to Zr precursor ratios.

Zr^{4+} doped $(18C6@K)_2HfBr_6$	ICP-AES Concentration (ppm)		
Hf : Zr Precursor Molar Ratio	Hf	Zr	Hf : Zr Molar Ratio
2:1	28.83 ± 1.21	7.275 ± 0.156	2.03
4:1	58.02 ± 1.93	6.405 ± 0.409	4.63
8:1	88.28 ± 1.37	5.744 ± 0.284	7.85
16:1	64.86 ± 2.29	2.203 ± 0.022	15.05

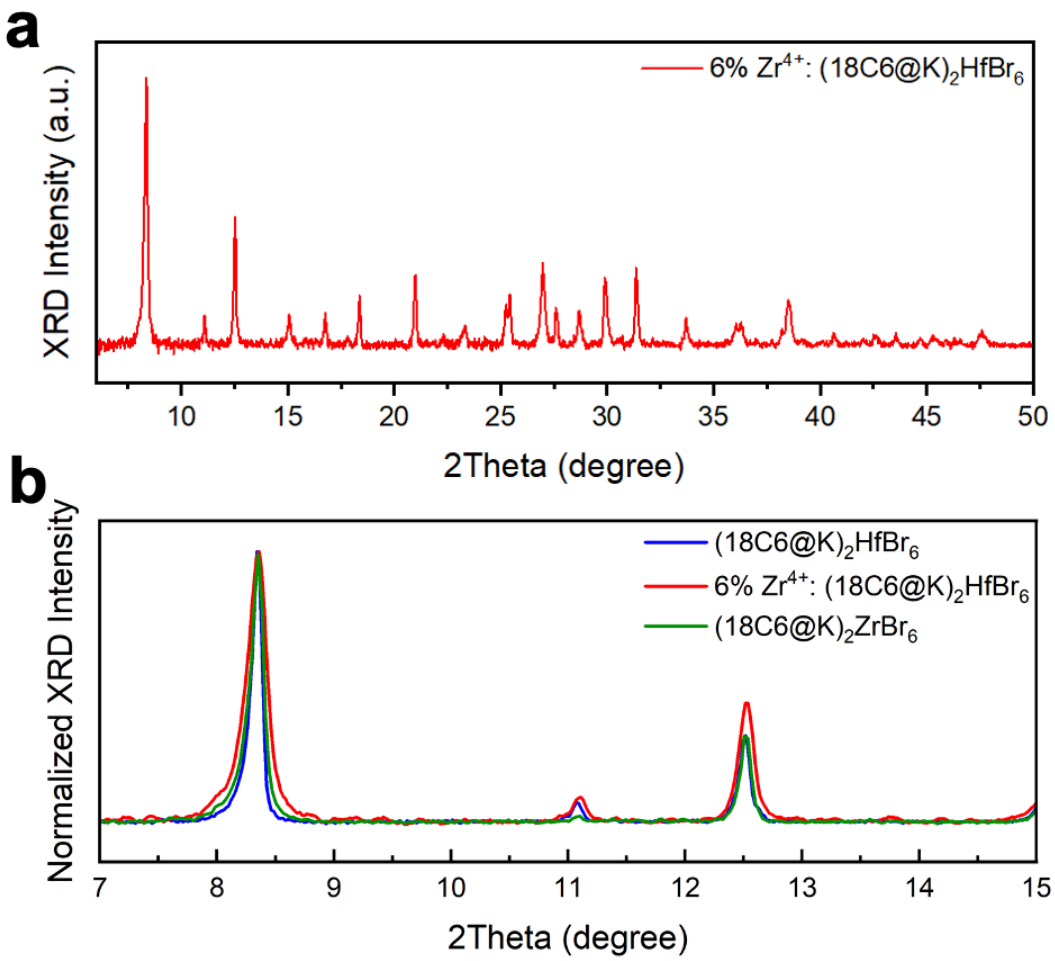

Figure 3.21. (a) PXRD of 6% Zr^{4+}: $(18C6@K)_2HfBr_6$ powder. (b) PXRD spectra of $(18C6@K)_2HfBr_6$, 6% Zr^{4+}: $(18C6@K)_2HfBr_6$, and $(18C6@K)_2ZrBr_6$ powders at 2Theta values between 7 to 15 degrees.

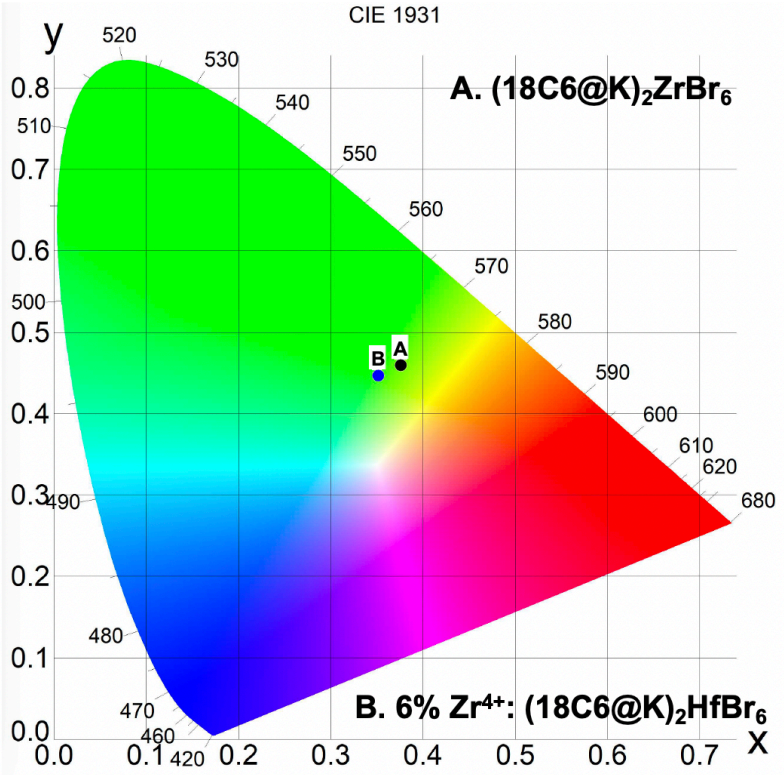

Figure 3.22. The CIE 1931 chromaticity diagram for the emissions of 6% Zr^{4+}: $(18C6@K)_2HfBr_6$ powder and $(18C6@K)_2ZrBr_6$ powder. The coordinates for the emission color of 6% Zr^{4+}: $(18C6@K)_2HfBr_6$ powder are (0.35159, 0.44648), and the coordinates for the emission color of $(18C6@K)_2ZrBr_6$ powder are (0.37601, 0.45927).

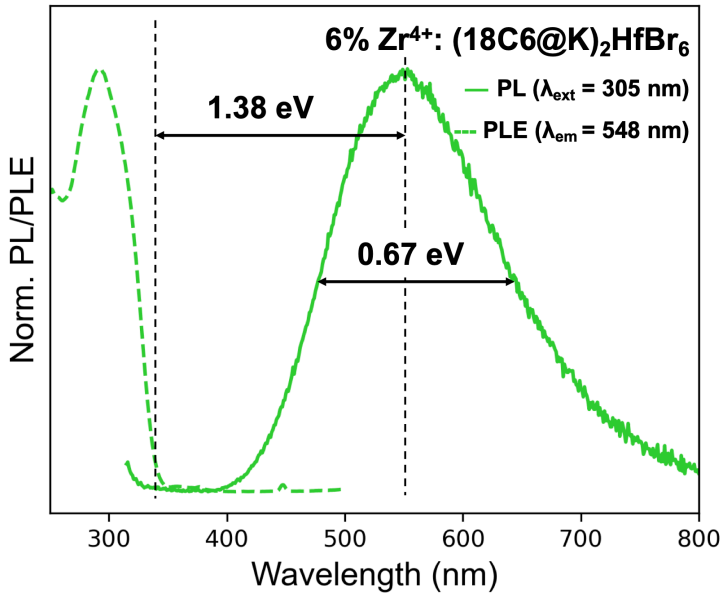

Figure 3.23. PL and PLE spectra of 6% Zr^{4+}: $(18C6@K)_2HfBr_6$ powder with 305 nm excitation.

Applying the Hf and Zr metal centers in the supramolecular assembly approach, and using various alloying/doping strategies, we have demonstrated high-color-purity blue and green emissions with near-unity PLQY. Nevertheless, more in-depth analysis is still needed to illustrate the mechanisms behind these fascinating emission properties.

Since the Hf/Zr halide octahedra in the supramolecular assembled samples are fully isolated and the PL spectra are broad and feature large stokes shifts, we hypothesize that the emission mechanism is an STE-based mechanism, similar to other $[MX_6]^{n-}$ octahedra separated by organic/inorganic cations. We have conducted a comprehensive photophysics analysis to confirm and gain deeper insights into the STE emission mechanism that underlies the blue and green emissions. The distinctive features of STE emissions, including their large Stokes shift and broadband nature, are primarily attributed to the electron-phonon coupling effect. Therefore, to unravel the STE emission mechanism, we have performed low-temperature PL measurements to examine the electron-phonon coupling in $(18C6@K)_2HfBr_6$. By doing so, we can better comprehend the underlying photophysics of the STE emission mechanism in this compound. With increasing temperatures, the PL peak is gradually broadened, and the peak is slightly red-shifted, indicating more significant phonon participation at higher temperatures (**Figure 3.24a**). It is worth mentioning that a small shoulder peak at ~550 nm is present, which is especially distinct at lower temperatures. It is verified that this additional peak is due to the Zr impurity in the $HfBr_4$ precursor, which has also been observed in previous literature[29]. ICP-AES further shows that there is ~0.5% $ZrBr_4$ impurity in the as-obtained $HfBr_4$ precursor, and that there is ~0.6% Zr^{4+} impurity in the synthesized $(18C6@K)_2HfBr_6$ (**Table 3.6**). The impurity atomic percentage is too low to be precisely detected by the previous SCXRD and EDX measurements. To deconvolve the emission from $(18C6@K)_2ZrBr_6$ impurities, a two-peak Gaussian fitting is applied to the PL spectrum at each temperature. **Figure 3.25** shows an example at 4 K. The FWHMs of the $(18C6@K)_2HfBr_6$ peaks are obtained from the Gaussian fittings and summarized in **Table 3.7**. The temperature dependence of the FWHM of the emission peak can be modeled using the theory of Toyozawa[39]. The theory applies a configuration coordinate model to explain the broadening of the emission originating from electron-phonon coupling. The FWHM depends on the effective phonon energy E_{ph}, the temperature T, and the Huang-Rhys electron-phonon coupling parameter S[40]:

$$FWHM = 2.36\sqrt{S}E_{ph}\sqrt{coth\frac{E_{ph}}{2K_BT}} \quad (1)$$

The relationship between FWHM and temperature is shown in **Figure 3.34b**. Analyzing the data according to equation 1 yields a coupling factor $S_1 = 92.2 \pm 3.6$ and an effective phonon energy $E_{ph1} = 21.4 \pm 0.5$ meV. This phonon mode corresponds to the asymmetric stretching mode (E_g) of the $[HfBr_6]^{2-}$ octahedra, which is observed at 20.4 meV (164.5 cm^{-1}) in the Raman spectrum (**Figure 3.26**). However, this phonon mode is only responsible for STE formation until 190 K. After 190 K, a higher energy phonon mode dominates STE formation. Shifting the zero temperature of equation 1 by 190 K, a second fit can be obtained with a coupling factor $S_2 = 108.8 \pm 12.4$ and an effective phonon energy $E_{ph2} = 25.8 \pm 1.6$ meV. This phonon mode corresponds to the symmetric stretching mode (A_{1g}) of the $[HfBr_6]^{2-}$ octahedra at 25.1 meV (202.5 cm^{-1}). The huge Huang-Rhys factor S in both scenarios indicates a very strong electron-phonon coupling in this material. As references, the S for $CsPbX_3$ (X = Br or I) is less than 1[41],

and the S for double perovskite $Cs_2AgBiBr_6$ is only ~12[42]. Self-trapping exciton behavior is closely related to the octahedra packing dimensionality. Through our supramolecular approach, the $[HfBr_6]^{2-}$ octahedra are more isolated by the bulky $(18C6@K)^+$ complexes, leading to stronger self-trapping behaviors with larger S values.

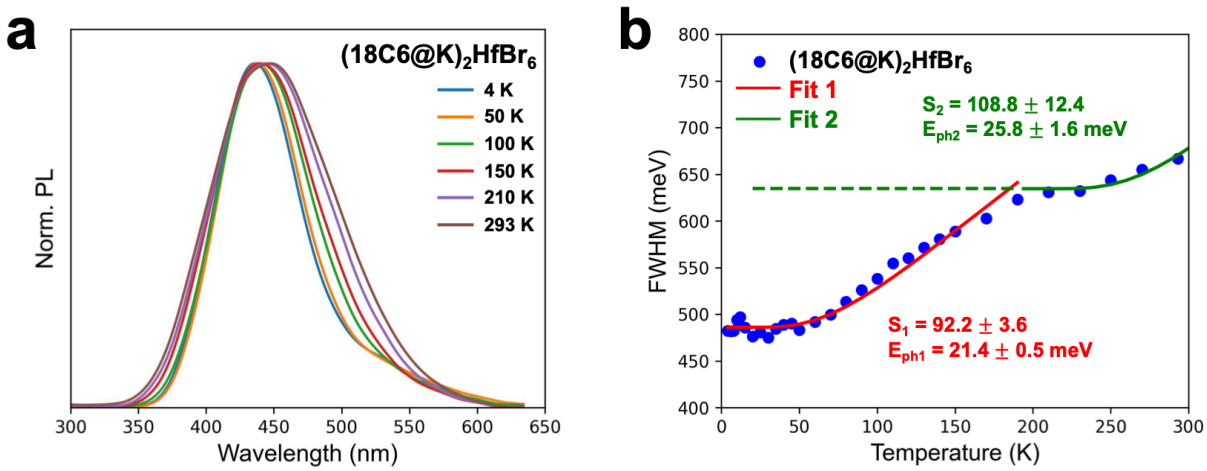

Figure 3.24. Low-T PL of $(18C6@K)_2HfBr_6$. (a) PL spectra of $(18C6@K)_2HfBr_6$ at 4 K, 50 K, 100 K, 150 K, 210 K, and 293 K. (b) Full width at half maximum (FWHM) of the PL spectra of $(18C6@K)_2HfBr_6$ at different temperatures, with the red and green solid lines denoting the least square fit to equation (1) at low temperature range (4 K to 150 K) and high temperature range (170 K to 293 K), respectively.

Table 3.6. ICP-AES concentrations of Hf and Zr in $HfBr_4$ precursor and $(18C6@K)_2HfBr_6$.

	ICP-AES Concentration (ppm)		
Sample Composition	Hf	Zr	Atomic Percent of Zr
$HfBr_4$	92.89 ± 3.36	0.226 ± 0.016	0.474%
$(18C6@K)_2HfBr_6$	124.9 ± 4.69	0.405 ± 0.008	0.630%

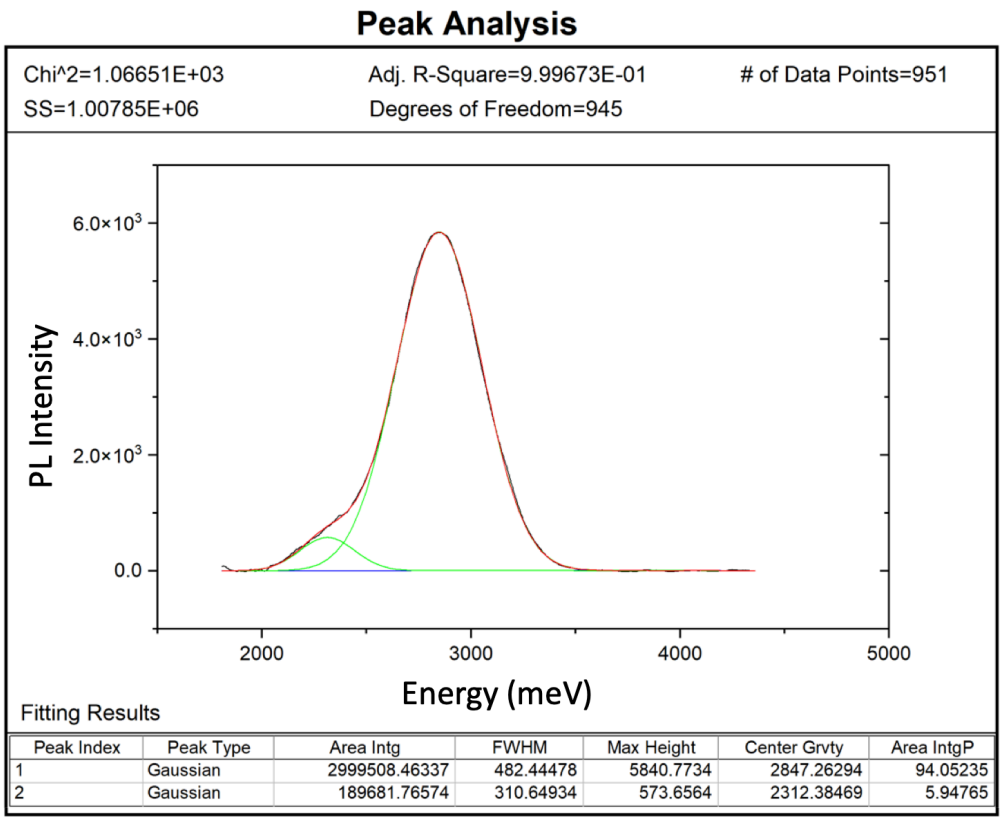

Figure 3.25. Gaussian peak fitting of the PL spectrum of $(18C6@K)_2HfBr_6$ powder measured at 4 K. The shoulder peak at ~2.3 eV comes from the ~0.6 atomic % Zr impurity in Hf.

Table 3.7. FWHM of the PL spectra of $(18C6@K)_2HfBr_6$ from 4 K to 293 K.

Temperature (K)	FWHM (meV)	Temperature (K)	FWHM (meV)
4	482.4	80	513.5
6	481.8	90	526.0
8	482.2	100	538.3
10	494.2	110	554.6
12	496.9	120	560.1
15	485.9	130	571.4
20	476.2	140	580.7
25	480.5	150	588.8
30	474.9	170	602.7
35	484.3	190	623.1
40	488.9	210	630.7
45	490.2	230	632.3
50	483.0	250	643.9
60	492.0	270	654.9
70	499.5	293	666.6

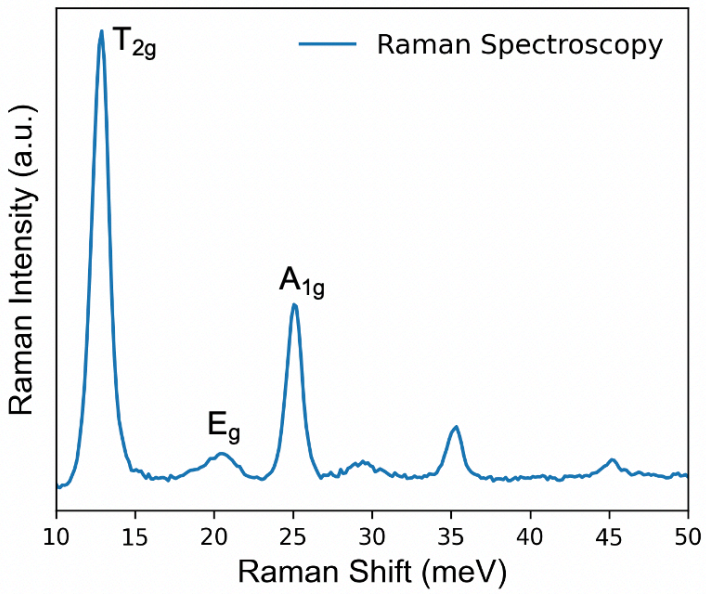

Figure 3.26. Raman spectroscopy of $(18C6@K)_2HfBr_6$ powder. Three distinct Raman-active modes including the low-frequency asymmetric bending mode T_{2g}, the asymmetric stretching mode E_g, the high-frequency symmetric stretching mode A_{1g} corresponding to the O_h-symmetric vibrating $[HfBr_6]^{2-}$.

Time-resolved PL (TRPL) studies on the supramolecular assembled single crystals have unveiled unique PL decay characteristics. In particular, the PL decay of the $(18C6@K)_2ZrBr_6$ single crystal exhibits a mono-exponential decay profile, and a PL lifetime of 6.80 µs is identified (**Figure 3.27**). Contrasting this, prior TRPL examinations on Cs_2ZrBr_6 manifest shorter PL lifetimes. Cs_2ZrBr_6 bulk crystal features a triple-exponential PL decay, yielding decay time constants of 40 ns (8.9%), 0.99 µs (24%), and 4.6 µs (68%)[29]. Additionally, colloidally synthesized Cs_2ZrBr_6 nanocrystals have similar time constants (0.78 µs and 4.5 µs) but show a double-exponential PL decay[30]. The PLQY is related to both the radiative and non-radiative decay rates (equation 2), so a more sluggish radiative decay does not necessarily correlate to a lower PLQY. Remarkably, the PLQY of $(18C6@K)_2ZrBr_6$ (49.75%) is higher than that of K_2ZrBr_6 powders (46.31%, from our measurement) and Cs_2ZrBr_6 nanocrystals (~44%)[30]. This observation suggests that the non-radiative decay rate of the supramolecular sample is slower than that of the vacancy-ordered double perovskite phases, potentially indicating a lower defect density in our assembled crystals. PL decay of $(18C6@K)_2ZrCl_4Br_2$ single crystal can also be fit using a single exponential function, with an even longer PL lifetime (12.08 µs) (**Figure 3.28**). Cs_2ZrCl_6 has a slightly longer PL lifetime (7.5 µs) than Cs_2ZrBr_6[43], but still smaller than $(18C6@K)_2ZrCl_4Br_2$. This further proves that the supramolecular materials system has longer PL lifetime and slower non-radiative decay rate. Moreover, the PL decay with mono-exponentially profile indicates that a single, dominant relaxation process is occurring in the supramolecular assembled crystals.

$$PLQY = \frac{k_{rad}}{k_{rad} + \Sigma k_{non-rad}} \quad (2)$$

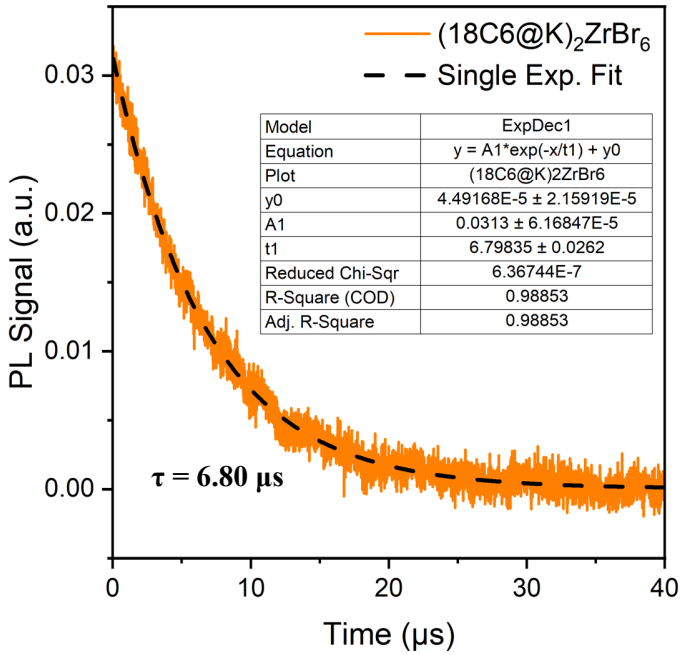

Figure 3.27. Time-resolved PL spectrum of $(18C6@K)_2ZrBr_6$ single crystal under 330 nm pulsed excitation source. The dashed line is the fit using a single-exponential decay function.

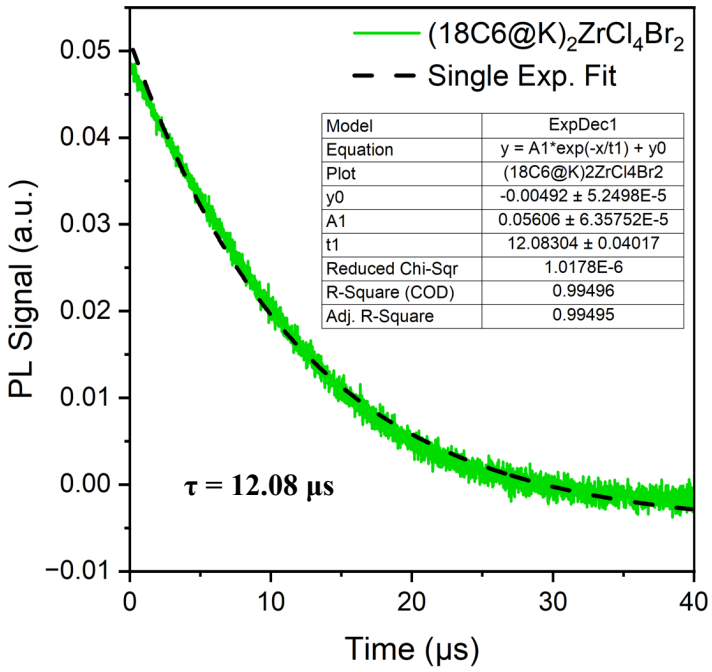

Figure 3.28. Time-resolved PL spectrum of $(18C6@K)_2ZrCl_4Br_2$ single crystal under 310 nm pulsed excitation source. The dashed line is the fit using a single-exponential decay function.

3.4 Photostability of the New Blue and Green Emitters

In this study, we also evaluate the photostability of these highly emissive blue and green emitters, a critical parameter directly influencing the performance and lifespan of various devices made from these materials. Notably, previous research in the OLED community has utilized a xenon lamp to simulate solar irradiation, dissolving Ir-complexes in deuterated toluene for measurements[44,45]. To ensure a fair comparison, we apply identical irradiation energy density (62 mW/cm^2) and temperature (35°C), and deuterated toluene is used to disperse the $(18C6@K)_2HfBr_6$ and $(18C6@K)_2ZrCl_4Br_2$ powders. **Figure 3.29** shows the PL intensity decay of the $(18C6@K)_2HfBr_6$ and $(18C6@K)_2ZrCl_4Br_2$ samples under continuous irradiation. Both decay trends are accurately described by the integrated rate law for the first-order reaction ($ln(I_t/I_0)=-kt$). The rate constant of photodegradation was estimated to be 5.1×10^{-3} h^{-1} and 3.0×10^{-3} h^{-1} for $(18C6@K)_2HfBr_6$ and $(18C6@K)_2ZrCl_4Br_2$, respectively. Remarkably, even under stringent irradiation conditions, the PL intensities of $(18C6@K)_2HfBr_6$ and $(18C6@K)_2ZrCl_4Br_2$ decrease to 80% after 43 hours and 73 hours, respectively. These findings underscore the superior photostability of the supramolecular assembled samples compared to most Ir-complexes, rivaling the best-reported green-emitting fac-[Ir(ppy)$_3$] reference ($k = 2.6 \times 10^{-3}$ h^{-1}) [44,45]. Previous studies on the photodegradation of the Ir-complexes, such as Ir(ppy)$_3$ and Ir(piq)$_3$, have identified singlet oxygen attack and interaction of the excited-state molecule with its local environment as primary degradation pathways[46]. However, the specific mechanisms for $(18C6@K)_2HfBr_6$ and $(18C6@K)_2ZrCl_4Br_2$ photodegradation require further investigation, extending beyond the scope of this paper.

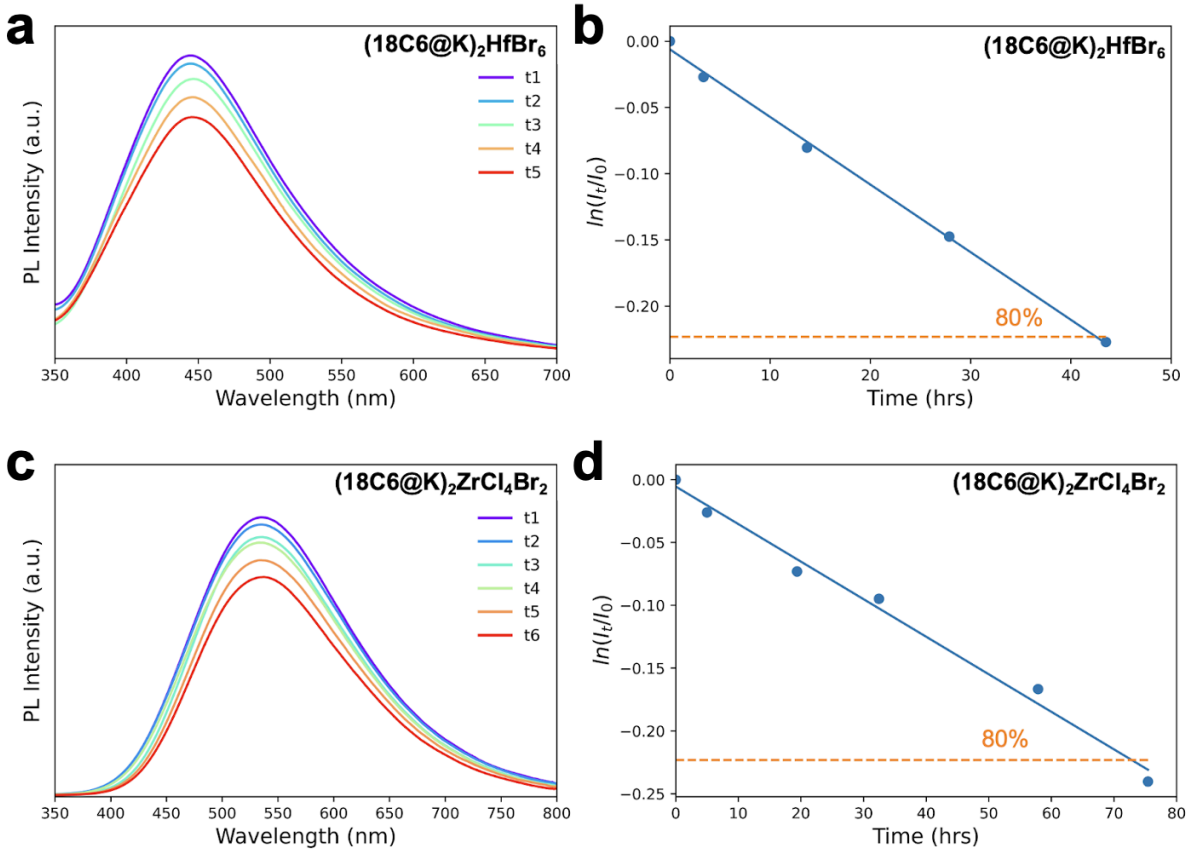

Figure 3.29. Photo-degradation responses of $(18C6@K)_2HfBr_6$ and $(18C6@K)_2ZrCl_4Br_2$ powders. The powders were dispersed in deuterated toluene, placed in an argon-filled UV cuvette, and subjected to irradiation with a xenon lamp at 62 mW/cm^2 and 35°C. (a) PL spectra of the $(18C6@K)_2HfBr_6$ sample measured at five different times during the continuous irradiation. (b) The PL intensity decay of the $(18C6@K)_2HfBr_6$ sample over irradiation time. (c) PL spectra of the $(18C6@K)_2ZrCl_4Br_2$ sample measured at six different times during the continuous irradiation. (d) The PL intensity decay of the $(18C6@K)_2ZrCl_4Br_2$ sample over irradiation time.

3.5 Application of the New Blue and Green Emitters

3.5.1 Display/Projection Demonstration with the Highly Emissive Blue and Green Semiconductor Inks

The high PLQY of the blue and green emission colors in the powders can be further preserved in the form of thin films, making it advantageous for various optoelectronic device applications[47-49]. A facile solution processable approach is proposed to achieve the thin film fabrication. Due to the good stability of those powders in non-polar organic solvents, they can be evenly dispersed in non-polar organic solution without losing the preferable high PLQY properties. Dichloromethane (DCM) is used as the solvent due to its low boiling point (39.6°C). The high volatility of the solvent guarantees that the inks can be easily converted within minutes in ambient conditions to form solid products. Furthermore, polystyrene (PS) polymers are also added to the solution to facilitate the thin film fabrication and patterning process. PS can form very uniform thin films with a second phase component by drop casting, spin coating, etc., under simple conditions[50,51]. As illustrated in **Figure 3.30**, the extremely emissive powders and PS polymer are dispersed in DCM solvent to form the inks. DCM can fully dissolve the polymer while maintaining the structural integrity of the powders. As shown in the image of the $(18C6@K)_2HfBr_6$/PS in DCM ink under a white lamp (**Figure 3.31a**), a uniform white suspension is achieved, which shows a bright blue emission under 254 nm UV lamp excitation. Solution PL confirms that the emission is solely from the $(18C6@K)_2HfBr_6$ powders in the ink, as the shape of the PL spectrum is the same as the powder's PL shape (**Figure 3.32**). The solution PLQY is 90.77%, which is only 5.45% lower than the powder PLQY. The slight reduction in PLQY is reasonable since DCM and PS do not absorb strongly in the blue color wavelength region (**Figure 3.33**), and some emission might be lost due to the scattering by the suspended powders in the ink. $(18C6@K)_2ZrCl_4Br_2$/PS in DCM ink also preserves the green emission of the $(18C6@K)_2ZrCl_4Br_2$ powders, and the solution PLQY is 75.01% (**Figure 3.31b**).

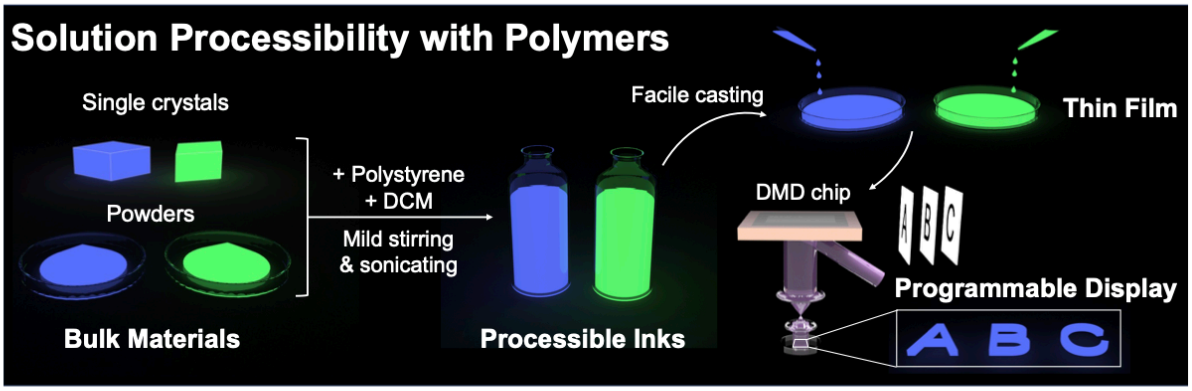

Figure 3.30. Schematic illustrating the thin film fabrication method and the programmable display application. The inks are formed by mixing $(18C6@K)_2HfBr_6$ or $(18C6@K)_2ZrCl_4Br_2$ powders and polystyrene (PS) in dichloromethane (DCM). Thin films can be obtained by drop casting in a petri dish, and the thin films demonstrate programmable display capability.

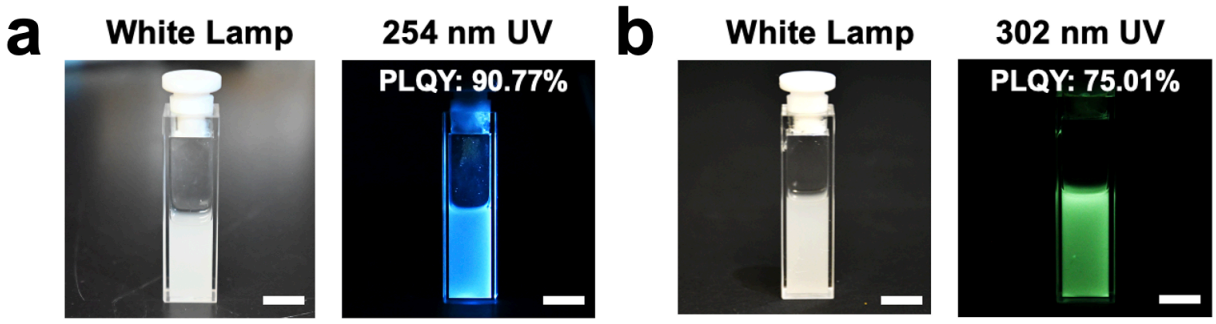

Figure 3.31. Schematic illustrating the thin film fabrication method and the programmable display application. The inks are formed by mixing $(18C6@K)_2HfBr_6$ or $(18C6@K)_2ZrCl_4Br_2$ powders and polystyrene (PS) in dichloromethane (DCM). Thin films can be obtained by drop casting in a petri dish, and the thin films demonstrate programmable display capability. The scale bars are 1 cm.

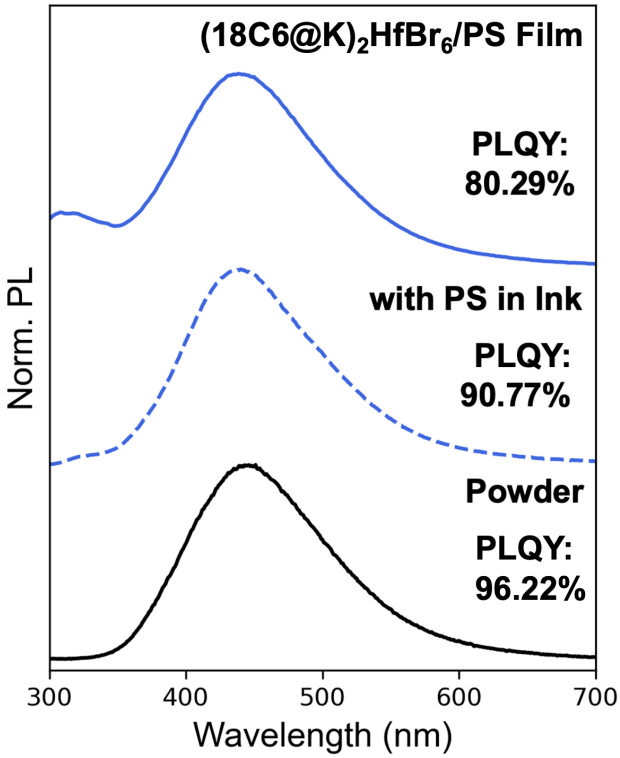

Figure 3.32. PL comparison of $(18C6@K)_2HfBr_6$/PS composite film, $(18C6@K)_2HfBr_6$ in PS ink, and $(18C6@K)_2HfBr_6$ powder.

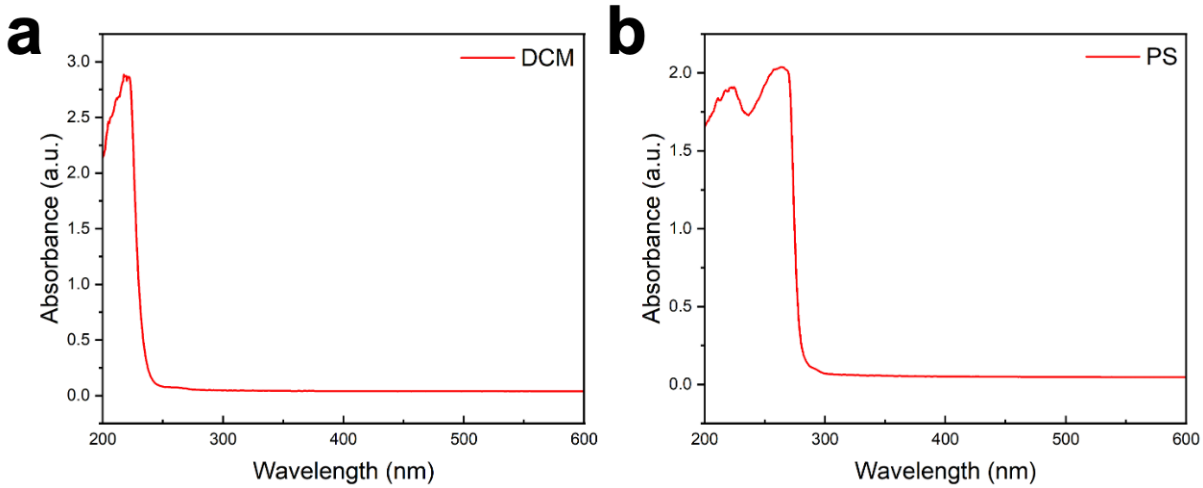

Figure 3.33. UV-vis absorption spectrum of (a) dichloromethane (DCM) solvent, and (b) polystyrene (PS) thin film.

Upon evaporation of the low-boiling point DCM solvent, the inks can be quickly drop casted in ambient conditions into a uniform powder/PS composite thin film (**Figure 3.34**). PXRD patterns of the $(18C6@K)_2HfBr_6$/PS composite (**Figure 3.35**) and $(18C6@K)_2ZrCl_4Br_2$/PS

composite (**Figure 3.36)** clearly show that the structural integrity of the powders is preserved in the PS matrix. Scanning electron microscopy (SEM) imaging of the $(18C6@K)_2HfBr_6$ powders and $(18C6@K)_2HfBr_6$/PS composite thin film surface (**Figure 3.37**) further suggests that the sub-micron sized powders are uniformly dispersed in the thin film, with little or no aggregation, and good coverage. Cross-sectional SEM imaging of the thin film (**Figure 3.38**) proves the presence and uniformity of the powders across all thicknesses. Under UV lamp, $(18C6@K)_2HfBr_6$/PS and $(18C6@K)_2ZrCl_4Br_2$/PS composite thin films show very bright blue and green emission, respectively (**Figure 3.34**). Compared with the PL of the powders, the PL shape of the thin films is also maintained (**Figure 3.32, 3.39**), and the PLQY is 80.29% and 68.99% for blue and green emitting composites, respectively.

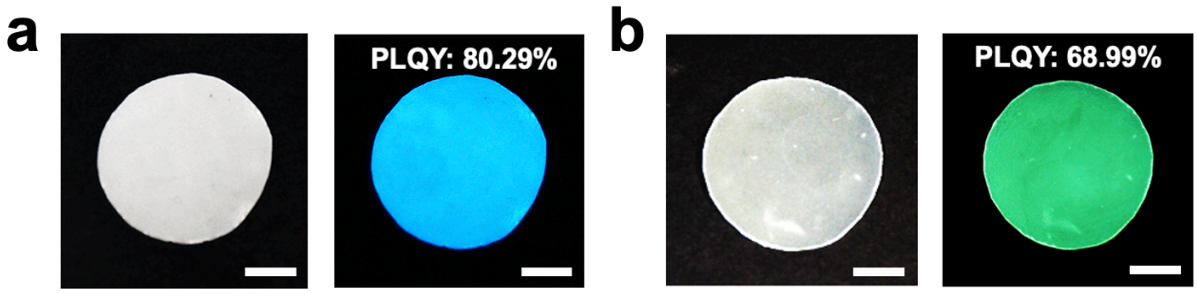

Figure 3.34. (a) $(18C6@K)_2HfBr_6$/PS composite thin film under white lamp and 254 nm UV lamp excitation. (b) $(18C6@K)_2ZrCl_4Br_2$/PS composite thin film under white lamp and 302 nm UV lamp excitation. The scale bars are 1 cm.

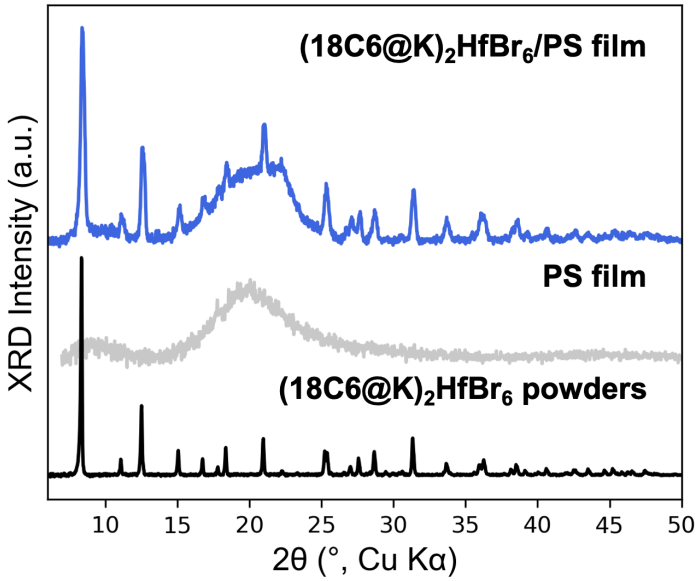

Figure 3.35. PXRD comparison of $(18C6@K)_2HfBr_6$/PS composite film, PS film, and $(18C6@K)_2HfBr_6$ powder.

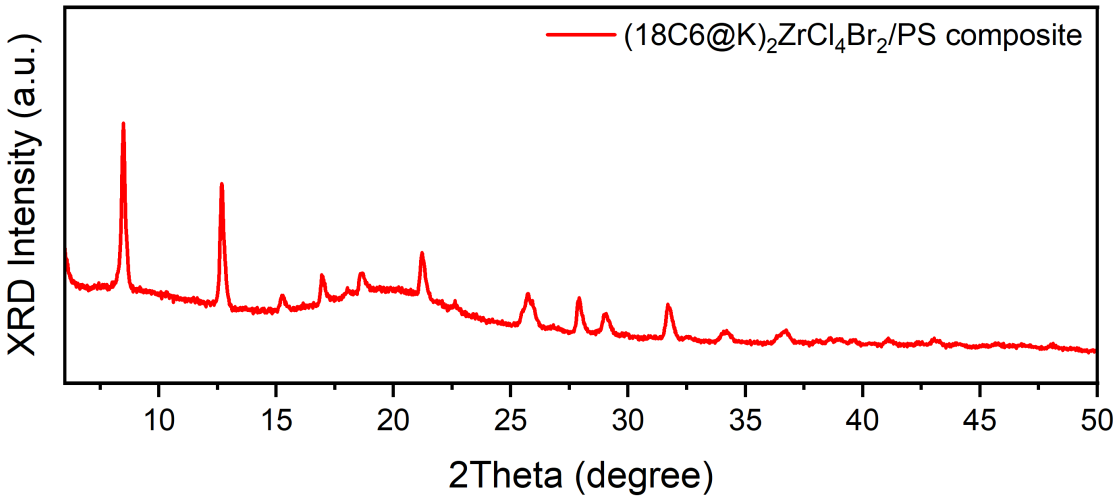

Figure 3.36. PXRD of $(18C6@K)_2ZrCl_4Br_2$/PS composite film.

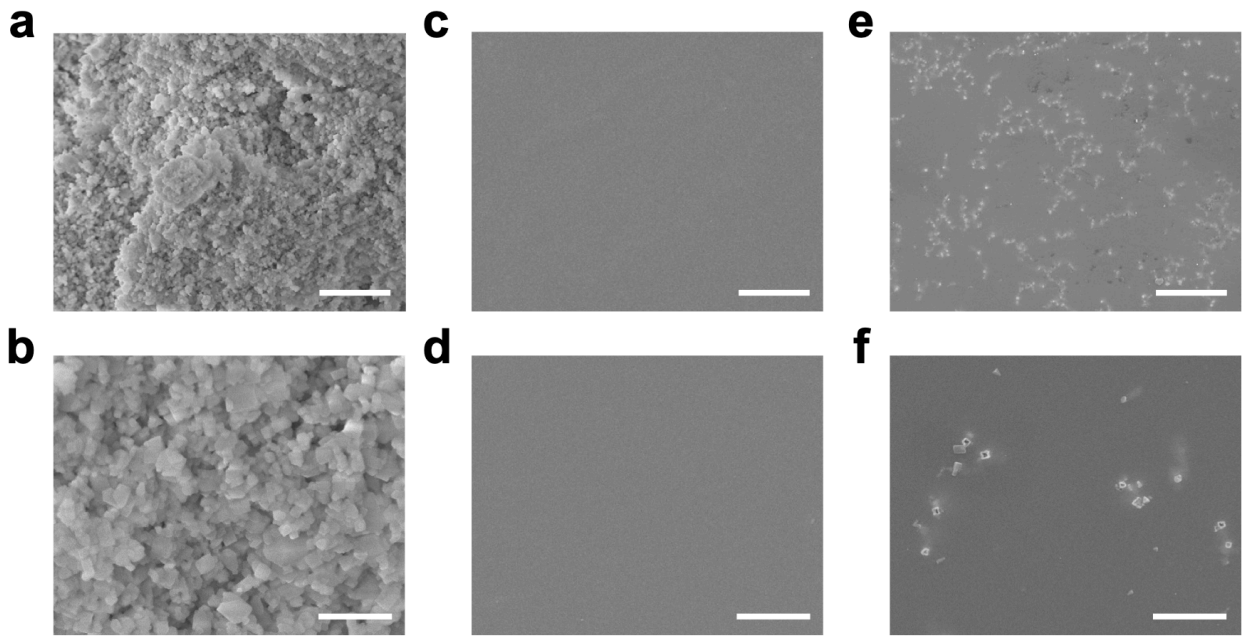

Figure 3.37. SEM imaging of the powder and thin films. (a, b) $(18C6@K)_2HfBr_6$ powder. (c, d) Top view of the surface of the pure polystyrene (PS) film. (e, f) Tope view of the surface of the $(18C6@K)_2HfBr_6$/PS composite film. The scale bars are 20 μm for a, c, and e, and 5 μm for b, d, and f.

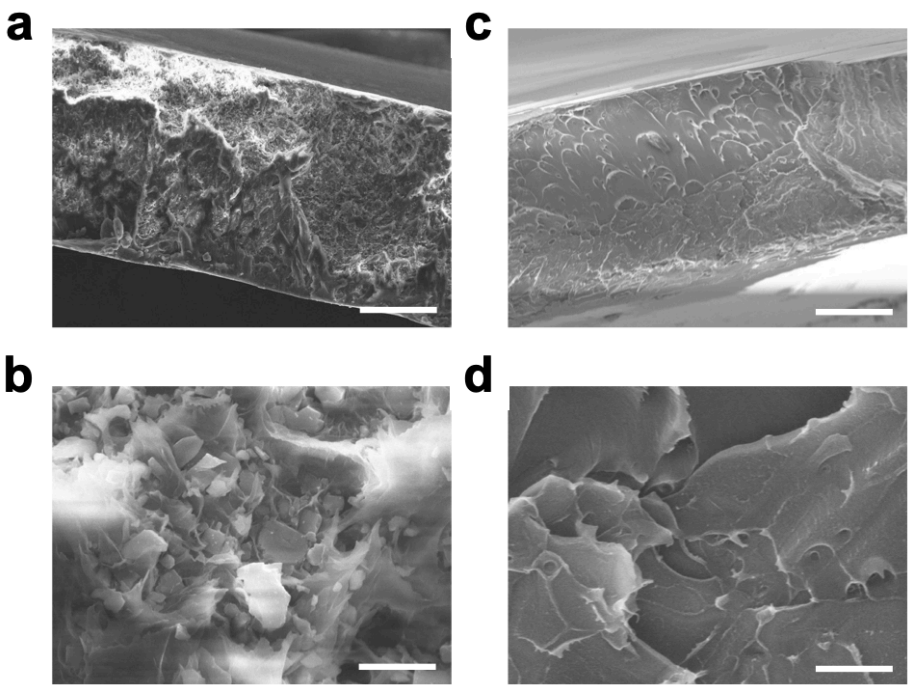

Figure 3.38. SEM imaging of the thin film cross-sections. (a, b) $(18C6@K)_2HfBr_6$/PS composite film. (c, d) Pure polystyrene (PS) film. The scale bars are 50 μm for a and c, and 5 μm for b and d.

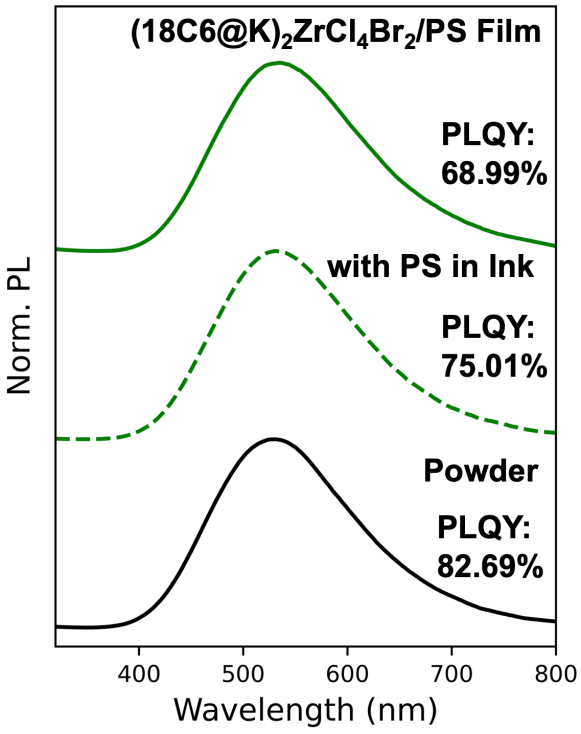

Figure 3.39. PL comparison of $(18C6@K)_2ZrCl_4Br_2$/PS composite film, $(18C6@K)_2ZrCl_4Br_2$ in PS ink, and $(18C6@K)_2ZrCl_4Br_2$ powder.

Besides, the stability of the air-sensitive Hf and Zr octahedral clusters are further enhanced in the PS polymer composite. It has been shown thermodynamically that O_2 and H_2O in the air will degrade the Cs_2HfBr_6 and Cs_2ZrBr_6 double perovskite structures[31]. This low air-stability has also been confirmed by our experimental observation. K_2HfBr_6 and K_2ZrBr_6 powders will turn from a white color into a brownish color upon exposure in air after only a few minutes and become non-emissive. In contrast, the $(18C6@K)_2HfBr_6$/PS and $(18C6@K)_2ZrCl_4Br_2$/PS composites still maintain their blue and green emission colors, respectively, after one month storage in the air. The air-stable PS polymers along with the hydrophobic crown ethers can greatly protect the air-sensitive Hf and Zr metal centers.

The intense luminescence, high uniformity and stability of the powder/PS composite thin films makes it a promising candidate for display application. Upon activation, the structured 250 nm UV light with programmed digital patterns (controlled by digital mirror device with pixel resolution 2560 × 1440) is sequentially patterned through projection optics onto the $(18C6@K)_2HfBr_6$/PS composite thin film at a spot size of 6.9 mm × 3.9 mm at a frame rate of 60 Hz. An emissive "Blue Cal Logo" is illuminated on the thin film with dimensions 3.8 mm in height and 4.7 mm in width (**Figure 3.40)**. Notably, the logo exhibits high luminosity, characterized by sharply defined edges. To further demonstrate dynamically changing display luminescence, we illuminate the alphabet sequence (from A to Z) onto the thin film, with fast flipping rate (0.1 s per letter). A video of 2.6 s is recorded (**https://youtu.be/4moKYc1sjzM**). Although the duration of each letter is very short, the blue emission with the shape of the letters is very sharp and bright, as illustrated in the snapshot photos (**Figure 3.41**). The size of the letters is only 3.1 mm in width and 3.9 mm in length, but every feature of the letters is clearly visible with similar emission intensity owing to the high uniformity of the thin film. Furthermore, the response time of the display should be very fast, since the PL decay rate of the $(18C6@K)_2HfBr_6$ powders is ~3 orders of magnitude faster than the frame rate of the digital mirror device. Indeed, playing the video frame by frame demonstrates that the letters switch extremely fast, with no blurring, ghosting, or trailing effects.

Figure 3.40. Image of the 'Cal Logo' blue emission on $(18C6@K)_2HfBr_6$/PS composite thin film. The scale bar for (F) is 3 mm.

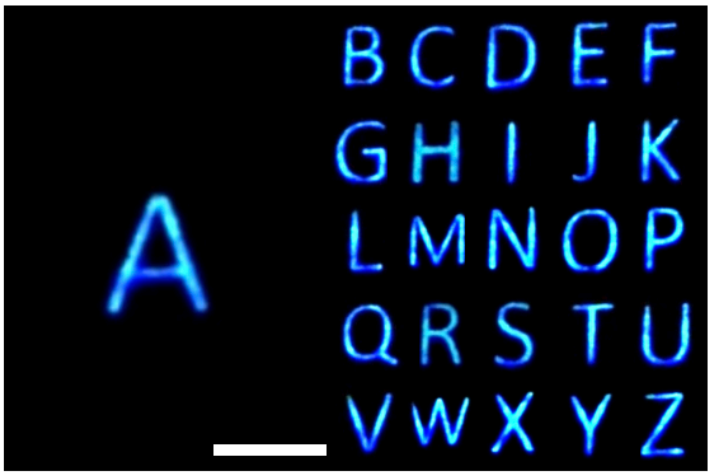

Figure 3.41. Snapshots of a video showing alphabet A through Z with 0.1 seconds per letter on (18C6@K)$_2$HfBr$_6$/PS composite thin film. The scale bar is 4 mm.

3.5.2 Blue-Green Dual-Color 3D-Printing with the Semiconductor Ink

The supramolecular assembled halide perovskite emitters exhibiting near-unity PLQY not only have applicability in display applications, but also demonstrate compatibility with 3D printing technologies. We propose the strategy to blend the emissive powders uniformly into a monomer resin. However, integration of diverse materials with 3D printing is a major barrier that requires all the materials to be compatible with the 3D printing process, and the preservation of the individual component functionalities without interference. Conventional resins for 3D printing typically use dyes as the photo absorber to control the depth of UV penetration and consequently the printing resolution, which however, absorbs light and shows its color in the printed parts. To avoid the interference with the blue and green emitters, we develop a photo-absorber-free resin mainly comprised of photo monomer poly(ethylene glycol) diacrylate (PEGDA). The polymerized PEGDA resin itself exhibits minimal absorption within the visible spectrum, featuring a modest absorption peak spanning from 355 nm to 425 nm (**Figure 3.52a**). Also, under 250 nm UV excitation, the resin exhibits significantly low emission (**Figure 3.52b**). Consequently, this suggests that the emission colors in the blue and green range of the powder should remain largely unaffected. Upon stirring and sonication, the powders can be uniformly dispersed into the PEGDA resin. We exploit a multi-material digital light printing method[52,53] to achieve a 3D assembly of the blue and green emitters into complex macro- and micro-architectures. Under 405 nm UV exposure, the photo-absorber-free resin can be rapidly converted into solid 3D structures (schematic of the 3D printing process shown in **Figure 3.53**). As expected, the PL from the (18C6@K)$_2$HfBr$_6$/PEGDA and the (18C6@K)$_2$ZrCl$_4$Br$_2$/PEGDA composites greatly resembles the PL from the powders (**Figure 3.52cd**).

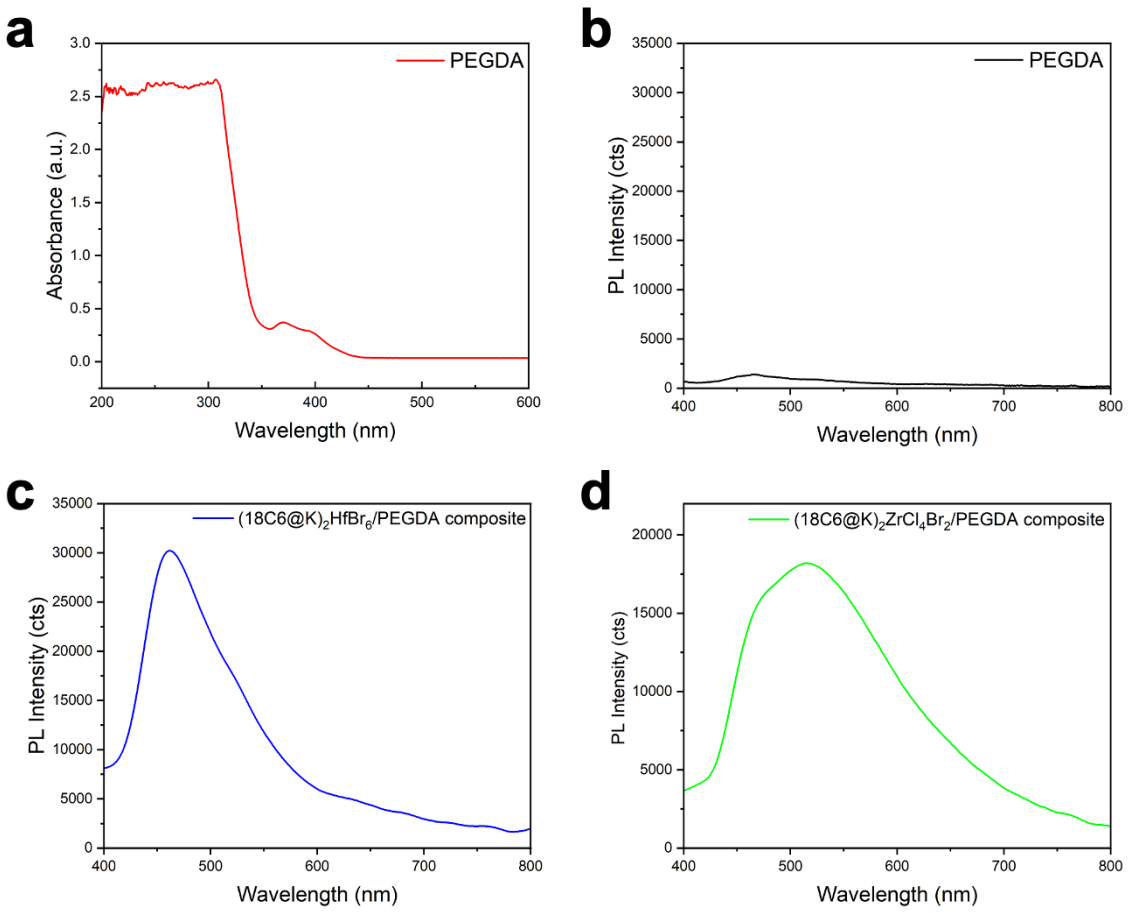

Figure 3.42. (a) UV-vis absorption spectrum of solid polyethylene glycol diacrylate (PEGDA) resin. PL measurement of (b) solid PEGDA resin, (c) $(18C6@K)_2HfBr_6$/PEGDA composite film, and (d) $(18C6@K)_2ZrCl_4Br_2$/PEGDA composite film. For the composites, the concentration of the crown ether powders in the PEGDA resin is 5 mg/ml.

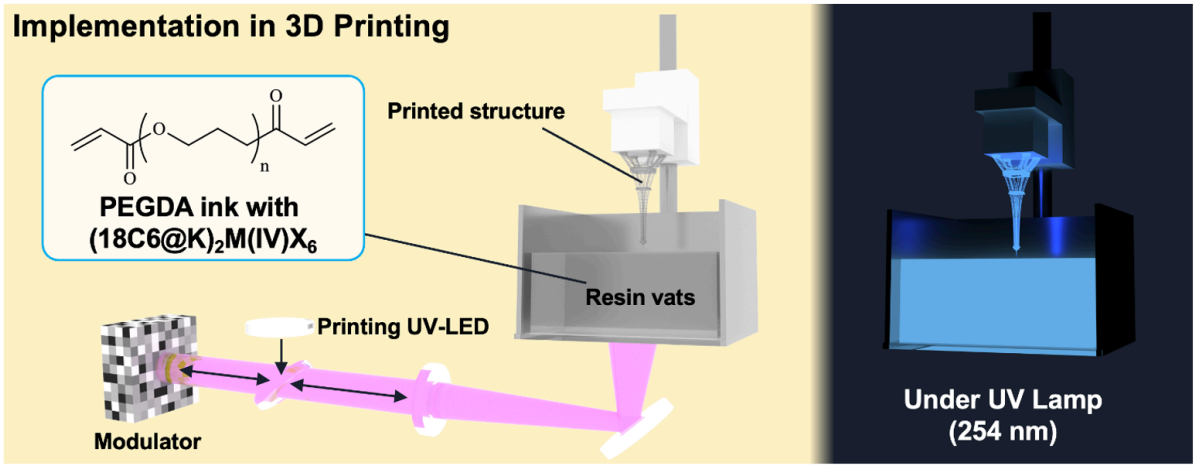

Figure 3.43. Schematic illustrating the 3D printing process.

In this study, we print the light emitting architectural models of the Eiffel Tower in both colors (**Figure 3.44a**). They are excited under 254 nm UV lamp, showing their respectively blue and green colors (**Figure 3.44b**). The dimensions of the two Eiffel Towers are within a few centimeters, but their intricate structural details are clearly discernible. This remarkable clarity results from the exceptional precision of the 3D printing process and the uniform dispersion of fine powders within the resin matrix. Given the sub-micrometer scale of these powders and a printing layer thickness of 40 μm, they can be evenly distributed throughout each layer, ensuring a homogeneous emission color profile across the entire architectural construct. More interestingly, a single 3D-printed structure can manifest dual emissions in both blue and green through resin alterations during the printing procedure. In **Figure 3.45**, we illustrate an Eiffel Tower design characterized by blue emissions at its upper and lower segments, with green emissions in its central region. Additionally, a second-order hierarchical octet truss structure is realized, displaying a distinct partition, with one half radiating in blue and the other in green (**Figure 3.46**). Notably, a close-up view of the boundary between these blue and green-emitting regions within the octet truss structure reveals the high precision in color transition, without any color crossover on either side. Twisted (**Figure 3.47a**) and conformal (**Figure 3.47b**) octet trusses architectures with dual emission are also achieved with bright emissions and high structural accuracy. Geometric shapes of cuboctahedron, tetrakaidecahedron, octet truss, and Menger sponge with the blue emitter embedded (**Figure 3.47c**) are also obtained to exhibit the variety of structures compatible with the 3D printing. These demonstrations serve as a proof of concept for the integration of emissive ionic powders with 3D printing technology. The potential applications of 3D printed light-emitting structures are extensive and constantly evolving, ranging from intricate interior ambient lighting solutions to seamless integration into wearable devices. Moreover, this technology extends its reach to art and sculpture, allowing for highly customized and visually captivating installations.

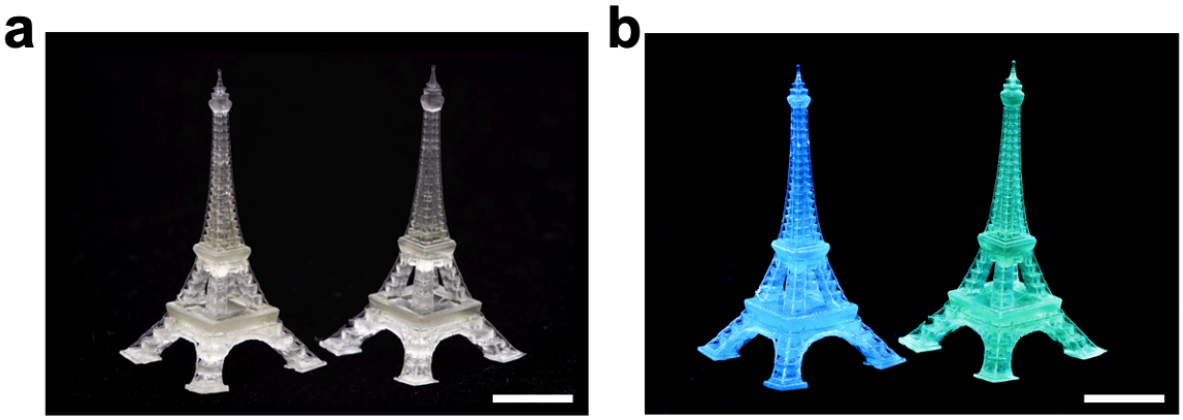

Figure 3.44. Two 3D-printed light-emitting Eiffel Towers under (a) white lamp and (b) 254 nm UV lamp excitation. The scale bars are 5 mm.

Figure 3.45. A dual-emitting Eiffel Tower under 254 nm UV lamp excitation. These printed architectures were photo-excited by 254 nm. The scale bar is 5 mm.

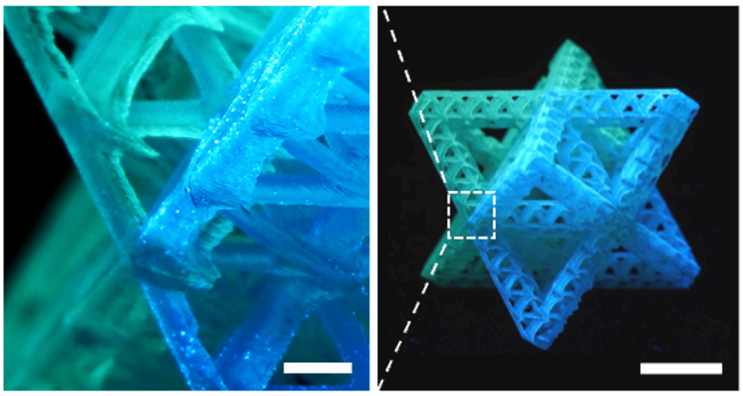

Figure 3.46. A dual-emitting conformal octet trusses with second-order hierarchical structures. The printed architecture was photo-excited by 254 nm. The scale bar is 5 mm and the scale bar for the zoom-in image is 0.6 mm.

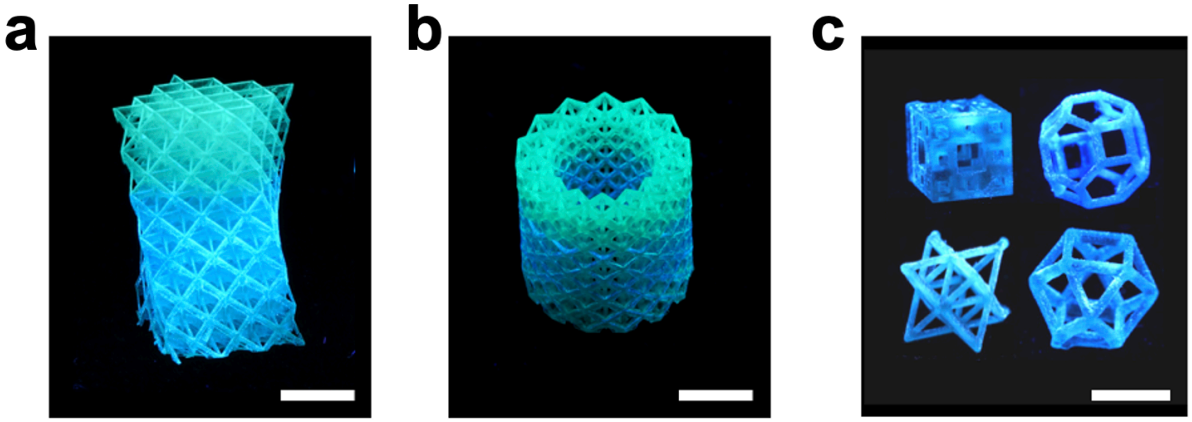

Figure 3.47. Conformal and twisted octet trusses with varying hierarchical structures, as well as geometric shapes including cuboctahedron, tetrakaidecahedron, and Menger sponge structures with the blue, and green emitters, or their combinations thereof, respectively. These printed architectures were photo-excited by 254 nm. The scale bars for (a) and (b) are 5 mm. The scale bar for (c) is 4 mm.

3.6 Experimental Methods

3.6.1 Materials Synthesis

Chemicals. 18-Crown-6 (18C6, 99%, Sigma Aldrich), KBr (99%, Sigma Aldrich), $HfBr_4$ (anhydrous, 98% (99.7%-Hf), Strem Chemicals), $ZrBr_4$ (99%, Alfa Aesar), acetonitrile (ACN, Fisher Chemical), diethyl ether (DEE, Sigma Aldrich), dichloromethane (DCM, Fisher Chemical), polystyrene (PS, average Mw ~192000, Sigma Aldrich), photo monomer poly(ethylene glycol) diacrylate (PEGDA, Mn 250, Millipore Sigma), photo initiator phenylbis(2,4,6-trimethylbenzoyl)phosphine oxide (Millipore Sigma), and inhibitor 4-methoxyphenol (Millipore Sigma) were used as received without further purification or modification. 18-Crown-6, KBr, $HfBr_4$, and $ZrBr_4$ were stored in an argon glovebox with O_2 and H_2O level below 0.5 ppm.

Synthesis of K_2HfBr_6 and K_2ZrBr_6 powders. KBr and $HfBr_4$/$ZrBr_4$ precursors with molar ratio 1:2 were measured and mixed into a grinder in an argon glovebox. The precursors were vigorously grinded for 10 minutes and then transferred into a 20 ml glass vial. They were heated on a hot plate in the glovebox at 200℃ for 1 h. The powder mixture was grinded again for 10 minutes, and then heated for another 1h at 200℃. The grinding and heating procedure were repeated for roughly five times until all the KBr had reacted with $HfBr_4$/$ZrBr_4$ according to inert atmosphere X-ray diffraction. Then the powder mixture was heated at 500℃ for 10 minutes to evaporate all the surplus $HfBr_4$/$ZrBr_4$ precursors.

Synthesis of $(18C6@K)_2HfBr_6$ and $(18C6@K)_2ZrBr_6$ powders and single crystals. 18-Crown-6, KBr, and $HfBr_4$/$ZrBr_4$ precursors with molar ratio 2:2:1 were weighed in the glovebox and transferred out into atmosphere using a 20 ml glass vial. The precursors were completely dissolved under 80℃ with vigorous stirring in acetonitrile (ACN) within 30 minutes. To obtain $(18C6@K)_2HfBr_6$ and $(18C6@K)_2ZrBr_6$ powders, 10 ml precursor solution was added into 30 ml diethyl ether (DEE) in a 50 ml centrifuge tube. White powders immediately formed upon the mixture of the two solutions. The powders were separated using centrifugation. The centrifugation speed was 5000 rpm, and the duration was 5 minutes. The powders were washed with DEE for three times and dried in vacuum at room temperature overnight. $(18C6@K)_2HfBr_6$ and $(18C6@K)_2ZrBr_6$ single crystals were grown using an anti-solvent diffusion method. 1 ml of the abovementioned precursor solution was added into a 4 ml vial, which was placed into a 20 ml vial with 4 ml of DEE. After approximately two days, single crystals were formed on the bottom and the wall of the 4 ml vial. Single crystals were washed 3 times with DEE and dried in vacuum at room temperature overnight. Powders and single crystals were stored in an argon glovebox with O_2 and H_2O level below 0.5 ppm for future use.

Synthesis of $(18C6@K)_2ZrCl_xBr_{6-x}$ powders and single crystals. 18-Crown-6, KCl, KBr, $ZrCl_4$ and $ZrBr_4$ precursors with molar ratio 12:2x:12-2x:x:6-x were weighed in the glovebox

and transferred out into atmosphere using a 20 ml glass vial. The precursors were completely dissolved under 80℃ with vigorous stirring in ACN within 30 minutes. To obtain $(18C6@K)_2ZrCl_{6-x}Br_x$ powder, 10 ml precursor solution was added into 30 ml diethyl ether (DEE) in a 50 ml centrifuge tube. White powders immediately formed upon the mixture of the two solutions. The powders were separated using centrifugation. The centrifugation speed was 5000 rpm, and the duration was 5 minutes. The powders were washed with DEE for three times and dried in vacuum at room temperature overnight. $(18C6@K)_2ZrCl_4Br_2$ single crystal was grown using an anti-solvent diffusion method. 1 ml of the abovementioned precursor solution was added into a 4 ml vial, which was placed into a 20 ml vial with 4 ml of DEE. After approximately two days, single crystals were formed on the bottom and the wall of the 4 ml vial. Single crystals were washed 3 times with DEE and dried in vacuum at room temperature overnight. Powders and single crystals were stored in an argon glovebox with O_2 and H_2O level below 0.5 ppm for future use.

Synthesis of Zr^{4+} doped $(18C6@K)_2HfBr_6$ powders and single crystals. 18-Crown-6, KBr, and $HfBr_4/ZrBr_4$ precursors with molar ratio 2:2:1 were weighed in the glovebox and transferred out into atmosphere using a 20 ml glass vial. The precursors were completely dissolved under 80℃ with vigorous stirring in ACN within 30 minutes. The same molar concentration $ZrBr_4$ and $HfBr_4$ precursor solutions were mixed with a 1:16, 1:8. 1:4 and 1:2 volume ratio, respectively for different Zr^{4+} atomic ratios. To obtain 6% Zr^{4+}: $(18C6@K)_2HfBr_6$ powders, 10 ml 1:16 mixed precursor solution was added into 30 ml DEE in a 50 ml centrifuge tube. White powders immediately formed upon the mixture of the two solutions. The powders were separated using centrifugation. The centrifugation speed was 5000 rpm, and the duration was 5 minutes. The powders were washed with DEE for three times and dried in vacuum at room temperature overnight. 6% Zr^{4+}: $(18C6@K)_2HfBr_6$ single crystals were grown using an anti-solvent diffusion method. 1 ml of the abovementioned mixed precursor solution was added into a 4 ml vial, which was placed into a 20 ml vial with 4 ml of DEE. After approximately two days, single crystals were formed on the bottom and the wall of the 4 ml vial. Single crystals were washed 3 times with DEE and dried in vacuum at room temperature overnight. Powders and single crystals were stored in an argon glovebox with O_2 and H_2O level below 0.5 ppm for future use.

Synthesis of $(18C6@K)_2HfBr_6$/PS in DCM, 6% Zr^{4+}: $(18C6@K)_2HfBr_6$/PS in DCM, and $(18C6@K)_2ZrCl_4Br_2$/PS in DCM inks. 100 mg PS was fully dissolved in 5 ml DCM with a stir bar in a 20 ml vial at room temperature. 50 mg $(18C6@K)_2HfBr_6$/6% Zr^{4+}: $(18C6@K)_2HfBr_6$/$(18C6@K)_2ZrCl_4Br_2$ powders were added into the abovementioned PS/DCM solution, then alternatively stirred and sonicated for 4 hours at room temperature to achieve a uniform suspension. The inks for PLQY measurements were diluted with DCM to achieve a 0.3 absorbance to guarantee the most accurate solution PLQY determination.

Synthesis of $(18C6@K)_2HfBr_6$/PS, 6% Zr^{4+}: $(18C6@K)_2HfBr_6$/PS and $(18C6@K)_2ZrCl_4Br_2$/PS composite thin films. The composite thin films were synthesized from direct drying of the inks in a glass petri dish at room temperature in air overnight. The dried thin films were then peeled off from the petri dish and cut into a round shape.

3.6.2 Materials Characterization

Optical Microscope Imaging. An unpolarized, white-light optical microscope was used to visualize single crystals/thin films under either a 10×, a 20×, or a 50× microscope objective. The samples were observed under bright-field imaging. The single crystals were dispersed onto glass for measurement. The thin film samples were free-standing.

Scanning electron microscopy (SEM) with standard secondary electron imaging. Prior to imaging, the powder and thin films samples were sputtered with ~5 nm of Au (Denton Vacuum, Moorestown, NJ). The samples were imaged at 15kV/ high probe current by Benchtop SEM (JCM-7000, Tokyo, Japan).

Scanning electron microscopy with energy dispersive X-ray (SEM/EDX) spectroscopy. Prior to imaging, the single crystal samples were sputtered with ~5 nm of Au (Denton Vacuum, Moorestown, NJ). A field-emission SEM (FEI Quanta 3D FEG SEM/FIB) and the EDX detector were used to determine elemental ratios at the QB3-Berkeley Biomolecular Nanotechnology Center (BNC).

Inductively coupled plasma atomic emission spectroscopy (ICP-AES). ICP-AES results were collected using a Perkin Elmer ICP Optima 7000 DV Spectrometer at the Microanalytical Facility in College of Chemistry, UC Berkeley.

Single-crystal X-ray diffraction (SCXRD). The SCXRD data were collected at the Small Molecule X-ray Crystallography Facility (CheXray) in College of Chemistry, UC Berkeley. SCXRD were measured with a Rigaku XtaLAB P200 instrument equipped with a MicroMax-007 HF microfocus rotating anode and a Pilatus 200K hybrid pixel array detector using monochromated Cu Kα radiation (λ = 1.54184 Å) or Mo Kα radiation (λ = 0.71073 Å). All crystal datasets were collected at room temperature (298 K). CrysAlisPro[54] was used for data collection and data processing, including a multi-scan absorption correction applied using the SCALE3 ABSPACK scaling algorithm within CrysAlisPro. Using Olex2[55], the structures were solved with the SHELXT[56] structure solution program using Intrinsic Phasing and refined with the SHELXL[57] refinement package using Least Squares minimization. Due to the occupation of disordered solvent molecules in the crystal voids, solvent masks were used during the refinement. All reflections where [error/esd] > 5 were omitted, as the existence of disordered molecules will result in high error/esd values in low d-spacing diffractions.

Ambient condition powder X-ray diffraction (PXRD). Powder X-ray diffraction (PXRD) data of $(18C6@K)_2HfBr_6$ powders, $(18C6@K)_2ZrBr_6$ powders, 6% Zr^{4+}: $(18C6@K)_2HfBr_6$ powders, $(18C6@K)_2HfBr_6$/PS composite, and 6% Zr^{4+}: $(18C6@K)_2HfBr_6$/PS composite were collected using a Bruker D8 laboratory diffractometer with a Cu Kα radiation source in ambient condition. Data was collected from $2\theta = 6°$ to 50°.

Inert atmosphere PXRD. PXRD of K_2HfBr_6 and K_2ZrBr_6 powders were collected using a Rigaku Miniflex 6G Benchtop Powder XRD with a Cu Kα radiation source and an inert atmosphere sample holder. The powder samples were loaded onto the sample holder inside an argon glovebox with O_2 and H_2O level below 0.5 ppm.

Raman spectroscopy. The Raman spectra of all the samples were measured by a confocal Raman microscope system (Horiba LabRAM HR800 Evolution). The powders were dispersed onto glass microscope slides for measurement. A continuous-wave (cw) 632.8 nm laser was focused onto a crystal facet at a constant power density set by neutral density filters. The Raman

signal from the sample was collected using a microscope objective in a backscattering geometry (100×, NA 0.6). High-resolution Raman spectra were measured with a charge-coupled device (CCD) detector equipped with a diffraction grating of 1800 gr/mm and a long pass filter (100 cm^{-1}) to remove the Rayleigh scattering line from the signal.

Photoluminescence spectroscopy (PL) and photoluminescence quantum yield (PLQY). PL and PLQY measurements were collected with the FS5 Spectrofluorometer (Edinburgh Instruments) using the SC-30 integrating sphere. The $(18C6@K)_2HfBr_6$, K_2HfBr_6, $(18C6@K)_2ZrBr_6$, K_2ZrBr_6, $(18C6@K)_2ZrCl_4Br_2$, and 6% Zr^{4+}: $(18C6@K)_2HfBr_6$ powders were densely packed onto the sample holder and then the surface was flattened for measurement. A 150 W continuous-wave ozone-free xenon lamp was focused onto the sample. $(18C6@K)_2HfBr_6$ and K_2HfBr_6 were excited using 275 nm excitation wavelength, $(18C6@K)_2ZrBr_6$ and K_2ZrBr_6 were excited using 290 nm excitation wavelength, $(18C6@K)_2ZrCl_4Br_2$ was excited using 295 nm excitation wavelength, and 6% Zr^{4+}: $(18C6@K)_2HfBr_6$ were excited using 305 nm excitation wavelength. The PL signal from the sample was collected by a UV-enhanced Si photodiode array equipped with a diffraction grating of 1200 gr/mm. The PL spectra were collected under a 0.2 s dwell time from 285 to 800 nm for the $(18C6@K)_2HfBr_6$ and K_2HfBr_6 samples, from 300 to 800 nm for $(18C6@K)_2ZrBr_6$ and K_2ZrBr_6 samples, from 305 to 800 nm for $(18C6@K)_2ZrCl_4Br_2$ sample, and from 315 to 800 nm for the 6% Zr^{4+}: $(18C6@K)_2HfBr_6$ sample. The PLQY spectra of both the blank and sample were collected under a 0.2 s dwell time from 265 to 800 nm for the $(18C6@K)_2HfBr_6$ and K_2HfBr_6 samples, from 280 to 800 nm for the $(18C6@K)_2ZrBr_6$ and K_2ZrBr_6 samples, from 285 to 800 nm for the $(18C6@K)_2ZrBr_6$ and K_2ZrBr_6 samples, and from 295 to 800 nm for the 6% Zr^{4+}: $(18C6@K)_2HfBr_6$ sample. The PLQY values were determined by the PLQY determination wizard of the Fluoracle (version 2.15.2) operating software for the FS5 Spectrofluorometer. PL and PLQY measurements of the PS polymer composite samples were measured with the free-standing composite films on a UV-grade fused silica microscope slide as a substrate. PL and PLQY measurements of the DCM ink samples were measured using a quartz cuvette as the sample holder.

Low-temperature photoluminescence spectroscopy (Low-T PL). The low-T PL measurements were collected with a home-built PL microscope system. Powder samples were dispersed onto mica substrates for measurement. A broadband deuterium lamp (Thorlabs SLS204 Stabilized Deuterium Lamp) was filtered down to a 250 nm excitation line using a bandpass filter (250 nm/10 nm). The 250 nm excitation line was focused obliquely onto the sample with a constant power density. The PL signal from the sample was collected using a microscope objective (50×) coupled to a longpass filter (cut-on wavelength: 325 nm) to remove the excitation line from the signal. PL spectra were collected with a Si charge-coupled device (CCD) detector cooled to −120 °C via liquid nitrogen and equipped with a diffraction grating of 150 gr/mm. The low-T (4 K to 293 K) PL measurements were performed in a Janis ST-500 SuperTran continuous flow cryostat system attached to the home-built PL microscope system. Liquid gallium-indium eutectic (Ga 75.5%/In 24.5%, ≥ 99.99% trace metals basis) was used to adhere samples to the cryostat stage, and the cryostat chamber was placed under vacuum with a continuous flow of liquid helium (LHe). A temperature controller was used to monitor the cryostat stage temperature and maintain it at the desired temperature.

Time-resolved photoluminescence spectroscopy (TRPL). Single crystals were placed and pressed onto a double-sided copper tape supported by a quartz slide. The $(18C6@K)_2HfBr_6$ and

$(18C6@K)_2ZrCl_4Br_2$ single crystal samples were excited at 310 nm, and the $(18C6@K)_2ZrBr_6$ single crystal sample was excited at 330 nm. The rep. rate of the excitations was 7.6kHz (~135μs between pulses. ~200 fs pulse) and the PL was separated from the residual excitations using two color glass filters (CS #: 3-70). A photomultiplier tube (PMT) (Hamamatsu-R9110) biased at 2 kV was used as the detector. The PMT output was connected to a current amplifier whose gain was set to 10^6 V/A. The output of the current amplifier was read using a 300MHz oscilloscope, each trace was averaged 512 times.

Chromaticity determination. The CIE 1931 chromaticity diagrams for all the samples were determined using the Fluoracle (version 2.15.2) operating software for the FS5 Spectrofluorometer from the corresponding PL spectra.

UV-visible (UV-vis) absorption spectroscopy. The absorption spectra for all the samples were measured by a UV-vis spectrophotometer (Shimadzu UV-2600). Data was collected in absorption mode over a wavelength range of 200 nm and 900 nm with a medium scanning rate.

2D display on thin film. $(18C6@K)_2HfBr_6$/PS thin film was illuminated at a 250 nm wavelength (High-power UV LED with ball lens, 250 nm, LED250J, Thorlabs) through structured UV light using a digital light modulator (digital mirror device, pixel resolution 2560 × 1440). The structured UV light with programmed digital patterns was sequentially patterned through projection optics onto the thin film at a spot size of 6.9 mm × 3.9 mm at a frame rate of 60 Hz. The thin film instantly displayed patterned images which were recorded through a digital camera.

Printing of light emitting 3D micro-architectures. A photo-absorber-free resin comprised of photo monomer poly(ethylene glycol) diacrylate, photo initiator phenylbis(2,4,6-trimethylbenzoyl)phosphine oxide (0.5 wt.% of PEGDA), and inhibitor 4-methoxyphenol (1.2 wt.% of PEGDA) was applied. $(18C6@K)_2HfBr_6$ and $(18C6@K)_2ZrCl_4Br_2$ powders were blended into the photo-absorber-free resin in a 5 mg/g ratio using vortex and bath sonication for 15 min. The inhibitor in high content is required to control the UV penetration depth and ensure the printing resolutions in the absence of photo absorbers. Upon 405 nm UV exposure (light intensity ~7 mW/cm^2), the photo-absorber-free resin was rapidly converted into solid 3D structures.

Density functional theory (DFT) calculations. The electronic band structures of $(18C6@K)_2HfBr_6$, K_2HfBr_6, $(18C6@K)_2ZrBr_6$, and K_2ZrBr_6 were calculated by DFT calculations with the CASTEP[58] code implemented in the Materials Studio 2020. The norm conserving pseudopotential[59] was applied for electron interactions in metal halides. All three structures models were imported from CIF files, and the geometry optimization has been applied with PBE-GGA[60]. A fine frame was chosen for energy cutoffs and calculation quality. Electronic band structures and partial density of states (pDOS) were calculated with PBE+GGA without spin-orbital coupling (SOC).

3.7 Conclusion

In conclusion, we demonstrate a supramolecular assembly strategy for achieving halide perovskite blue and green emitters with ultra-high PLQY, elucidate the mechanism behind these unique emissions, and showcase the compatibility with display and 3D printing applications.

Specifically, A composition of $(18C6@K)_2HfBr_6$ warrants a blue emission with near-unity (96.22%) PLQY, and $(18C6@K)_2ZrCl_4Br_2$ show green emission with a PLQY of 82.69%, respectively. The emission of the supramolecular assembled samples originates from the STE emission, with very strong electron-phonon coupling and micro-second PL lifetimes. The strongly confined excitonic emission with long lifetime may help understand the high PLQY in this new materials system. Fundamental question of energy transfer behavior among the various octahedra is probed with the alloying samples. We also show that the supramolecular approach is very promising in solution processability. The $(18C6@K)_2HfBr_6$/PS-DCM ink maintains a high PLQY of over 90%. Upon simple drop casting of the ink, uniform and highly emissive (over 80% PLQY) $(18C6@K)_2HfBr_6$/PS thin film can be obtained for display application. Finally, the powders with blue and green emissions are highly compatible with the 3D printing technology. The supramolecular assembly approach for halide perovskite building blocks catalyzes further investigation into the synthesis and characterization of supramolecular assembled functional materials, thereby laying the foundation for substantial progress in the field.

3.8 References

[1] M. A. Reshchikov, R. Y. Korotkov, Analysis of the temperature and excitation intensity dependencies of photoluminescence in undoped GaN films. Phys. Rev. B 64, 115205 (2001). doi:10.1103/PhysRevB.64.115205

[2] A. K. Viswanath, J. I. Lee, D. Kim, C. R. Lee, J. Y. Leem, Exciton-phonon interactions, exciton binding energy, and their importance in the realization of room-temperature semiconductor lasers based on GaN. Phys. Rev. B 58, 16333–16339 (1998). doi:10.1103/PhysRevB.58.16333

[3] W. Shan, B. D. Little, A. J. Fischer, J. J. Song, B. Goldenberg, W. G. Perry, M. D. Bremser, R. F. Davis, Binding energy for the intrinsic excitons in wurtzite GaN. Phys. Rev. B 54, 16369–16372 (1996). doi:10.1103/PhysRevB.54.16369

[4] C. Hauswald, P. Corfdir, J. K. Zettler, V. M. Kaganer, K. K. Sabelfeld, S. Fernández-Garrido, T. Flissikowski, V. Consonni, T. Gotschke, H. T. Grahn, L. Geelhaar, O. Brandt, Origin of the nonradiative decay of bound excitons in GaN nanowires. Phys. Rev. B 90, 19 (2014). doi:10.1103/PhysRevB.90.165304

[5] Y. Nanishi, The birth of the blue LED. Nat. Photon. 8, 884–886 (2014). doi:10.1038/nphoton.2014.291

[6] M. A. Reshchikov, M. Foussekis, J. D. McNamara, A. Behrends, A. Bakin, A. Waag, Determination of the absolute internal quantum efficiency of photoluminescence in GaN co-doped with Si and Zn. J. Appl. Phys. 111, 073106 (2012). doi:10.1063/1.3699312

[7] M. Shibata, T. Furuya, H. Sakaguchi, S. Kuma, Synthesis of gallium nitride by ammonia injection into gallium melt. J. Cryst. Growth 196, 47–52 (1999). doi:10.1016/S0022-0248(98)00819-7

[8] W. Yina, T. Shi, Y. Yan, Unusual defect physics in $CH_3NH_3PbI_3$ perovskite solar cell absorber. Appl. Phys. Lett. 104, 063903 (2014). doi: 10.1063/1.4864778

[9] R. J. Sutton, G. E. Eperon, L. Miranda, E. S. Parrott, B. A. Kamino, J. B. Patel, M. T. Hörantner, M. B. Johnston, A.-A. Haghighirad, D. T. Moore, H. J. Snaith, Bandgap-tunable cesium lead halide perovskites with high thermal stability for efficient solar cells. Adv. Energy Mater. 6, 1502458 (2016). doi: 10.1002/aenm.201502458

[10] M. R. Filip, G. E. Eperon, H. J. Snaith, F. Giustino, Steric engineering of metal-halide perovskites with tunable optical band gaps. Nat. Commun. 5, 5757 (2014). doi:10.1038/ncomms6757

[11] L. Protesescu, S. Yakunin, M. I. Bodnarchuk, F. Krieg, R. Caputo, C. H. Hendon, R. X. Yang, A. Walsh, M. V. Kovalenko, Nanocrystals of cesium lead halide perovskites ($CsPbX_3$, X = Cl, Br, and I): novel optoelectronic materials showing bright emission with wide color gamut. Nano Lett. 15, 3692–3696 (2015). doi:10.1021/nl5048779

[12] J. Kang, L.-W. Wang, High defect tolerance in lead halide perovskite $CsPbBr_3$. J. Phys. Chem. Lett. 8, 489–493 (2017). doi:10.1021/acs.jpclett.6b02800

[13] K. X. Steirer, P. Schulz, G. Teeter, V. Stevanovic, M. Yang, K. Zhu, J. J. Berry, Defect tolerance in methylammonium lead triiodide perovskite. ACS Energy Lett. 1, 360–366 (2016). doi:10.1021/acsenergylett.6b00196

[14] F. Deschler, M. Price, S. Pathak, L. E. Klintberg, D.-D. Jarausch, R. Higler, S. Hüttner, T. Leijtens, S. D. Stranks, H. J. Snaith, M. Atatüre, R. T. Phillips, R. H. Friend, High photoluminescence efficiency and optically pumped lasing in solution-processed mixed halide perovskite semiconductors. J. Phys. Chem. Lett. 5, 1421–1426 (2014). doi:10.1021/jz5005285

[15] F. D. Stasio, S. Christodoulou, N. Huo, G. Konstantato, Near-unity photoluminescence quantum yield in $CsPbBr_3$ nanocrystal solid-state films via postsynthesis treatment with lead bromide. Chem. Mater. 29, 7663–7667 (2017). doi:10.1021/acs.chemmater.7b02834

[16] J. Li, L. Gan, Z. Fang, H. He, Z. Ye, Bright tail states in blue-emitting ultrasmall perovskite quantum dots. J. Phys. Chem. Lett. 8, 6002–6008 (2017). doi:10.1021/acs.jpclett.7b02786

[17] S. Wang, C. Bi, J.Yuan, L. Zhang, J. Tian, Original core–shell structure of cubic $CsPbBr_3$@amorphous $CsPbBr_x$ perovskite quantum dots with a high blue photoluminescence quantum yield of over 80%. ACS Energy Lett. 3, 245–251 (2018). doi:10.1021/acsenergylett.7b01243

[18] X. Gong, O. Voznyy, A. Jain, W. Liu, R. Sabatini, Z. Piontkowski, G. Walters, G. Bappi, S. Nokhrin, O. Bushuyev, M. Yuan, R. Comin, D. McCamant, S. O. Kelley, E. H. Sargent, Electron–phonon interaction in efficient perovskite blue emitters. Nat. Mater. 17, 550–556 (2018). doi:10.1038/s41563-018-0081-x

[19] H. Luo, Y. Huang, H. Liu, B. Zhang, J. Song, Ionic liquid assisted pure blue emission $CsPbBr_3$ quantum dots with improved optical properties and alkyl chain regulated stability. J. Chem. Eng. 430. 132790 (2022). doi:10.1016/j.cej.2021.132790

[20] M. C. Folgueras, S. Louisia, J. Jin, M. Gao, A. Du, S. C. Fakra, R. Zhang, F. Seeler, K. Schierle-Arndt, P. Yang, Ligand-free processable perovskite semiconductor ink. Nano Lett. 21, 8856–8862 (2021). doi:10.1021/acs.nanolett.1c03308

[21] J. Jin, M. C. Folgueras, M. Gao, S. Yu, S. Louisia, Y. Zhang, L. N. Quan, C. Chen, R. Zhang, F. Seeler, K. Schierle-Arndt, P. Yang, A new perspective and design principle for halide perovskites: ionic octahedron network (ION). Nano Lett. 21, 5415–5421 (2021). doi:10.1021/acs.nanolett.1c01897

[22] M. Gao, Y. Zhang, Z. Lin, J. Jin, M. C. Folgueras, P. Yang, The making of a reconfigurable semiconductor with a soft ionic lattice. Matter 4, 3874–3896 (2019). doi:10.1016/j.matt.2021.09.023

[23] J. S. Manser, M. I. Saidaminov, J. A. Christians, O. M. Bakr, P. V. Kamat., Making and breaking of lead halide perovskites. Acc. Chem. Res. 49, 330–338 (2016). doi:10.1021/acs.accounts.5b00455

[24] C. Zhou, H. Lin, Y. Tian, Z. Yuan, R. Clark, B. Chen, L. J. van de Burgt, J. C. Wang, Y. Zhou, K. Hanson, Q. J. Meisner, J. Neu, T. Besara, T. Siegrist, E. Lambers, P. Djurovich, B. Ma, Luminescent zero-dimensional organic metal halide hybrids with near-unity quantum efficiency. Chem. Sci. 9, 586–593 (2018). doi:10.1039/C7SC04539E

[25] P. Han, C. Luo, S. Yang, Y. Yang, W. Deng, K. Han, All-inorganic lead-free 0D perovskites by a doping strategy to achieve a PLQY boost from < 2% to 90%. Angew. Chem. Int. Ed. 59, 12709–12713 (2020). doi: 10.1002/anie.202003234

[26] Z. Wang, Z. Zhang, L. Tao, N. Shen, B. Hu, L. Gong, J. Li, X. Chen, X. Huang, Hybrid chloroantimonates (III): thermally induced triple-mode reversible luminescent switching and laser-printable rewritable luminescent paper. Angew. Chem., Int. Ed. 58, 9974–9978 (2019). doi:10.1002/anie.201903945

[27] M. Li, Z. Xia. Recent progress of zero-dimensional luminescent metal halides. Chem. Soc. Rev. 50, 2626–2662 (2021). doi:10.1039/D0CS00779J

[28] J. A. Steele, P. Puech, M. Keshavarz, R. Yang, S. Banerjee, E. Debroye, C. W. Kim, H. Yuan, N. H. Heo, J. Vanacken, A. Walsh, J. Hofkens, M. B. J. Roeffaers, Giant electron–phonon coupling and deep conduction band resonance in metal halide double perovskite. ACS Nano 12, 8081–8090 (2018). doi:10.1021/acsnano.8b02936

[29] K. Saeki, Y. Fujimoto, M. Koshimizu, D. Nakauchi, H. Tanaka, T. Yanagida, K. Asai, Luminescence and scintillation properties of Cs_2HfBr_6 and Cs_2ZrBr_6 crystals. J. Appl. Phys. 57, 030310 (2018). doi:10.7567/JJAP.57.030310

[30] A. Abfalterer, J. Shamsi, D. J. Kubicki, C. N. Savory, J. Xiao, G. Divitini, W. Li, S. Macpherson, K. Gałkowski, J. L. MacManus-Driscoll, D. O. Scanlon, S. D. Stranks, Colloidal synthesis and optical properties of perovskite-inspired cesium zirconium halide nanocrystals. ACS Materials Lett. 2, 1644-1652 (2020). doi:10.1021/acsmaterialslett.0c00393

[31] C. Kaewmeechai, Y. Laosiritaworn, A. P. Jaroenjittichai, DFT calculation on electronic properties of vacancy-ordered double perovskites Cs_2(Ti, Zr, Hf)X_6 and their alloys: Potential

as light absorbers in solar cells. Results Phys. 25, 104225 (2021). doi:10.1016/j.rinp.2021.104875

[32] W. Thomas, H. Elias, Darstellung von HfCl4 und HfBr4 durch umsetzung von hafnium mit geschmolzenen metallhalogeniden. J. Inorg, Nucl. Chem. 38, 2227–2229 (1976). doi:10.1016/0022-1902(76)80199-6

[33] E. V. van Loef, G. Ciampi, U. Shirwadkar, L. S. Pandian, K. S. Shah, Crystal growth and scintillation properties of Thallium-based halide scintillators. J. Cryst. Growth. 532, 125438 (2020). doi:10.1016/j.jcrysgro.2019.125438

[34] S. Kodama, S. Kurosawa, K. Fujii, T. Murakami, M. Yashima, J. Pejchal, R. Král, M. Nikl, A. Yamaji, M. Yoshino, S. Toyoda, H. Sato, Y. Ohashi, K. Kamada, Y. Yokota, A. Yoshikawa, Single-crystal growth, structure and luminescence properties of $Cs_2HfCl_3Br_3$. Opt. Mater. 106, 109942 (2020). doi:10.1016/j.optmat.2020.109942

[35] C. Zhu, J. Jin, M. Gao, A. M. Oddo, M. C. Folgueras, Y. Zhang, C.-K. Lin, P. Yang, Supramolecular assembly of halide perovskite building blocks. J. Am. Chem. Soc. 144, 12450–12458 (2022). doi:10.1021/jacs.2c04357

[36] J. E. Saal, S. Kirklin, M. Aykol, B. Meredig, C. Wolverton, Materials design and discovery with high-throughput density functional theory: the open quantum materials database (OQMD). JOM 65, 1501–1509 (2013). doi:10.1007/s11837-013-0755-4

[37] S. Kirklin, J. E. Saal, B. Meredig, A. Thompson, J. W. Doak, M. Aykol, S. Rühl, C. Wolverton, The open quantum materials database (OQMD): assessing the accuracy of DFT formation energies. Npj Comput. Mater. 1, 15010 (2015). doi:10.1038/npjcompumats.2015.10

[38] Q. A. Akkerman, . D'Innocenzo, S. Accornero, A. Scarpellini, A. Petrozza, M. Prato, L. Manna, Tuning the optical properties of cesium lead halide perovskite nanocrystals by anion exchange reactions. J. Am. Chem. Soc. 137, 10276–10281 (2015). doi:10.1021/jacs.5b05602

[39] Y. Toyozawa. Further contribution to the theory of the line-shape of the exciton absorption band. Prog. Theor. Phys. 27, 89–104 (1962). doi:10.1143/PTP.27.89

[40] W. Stadler, D. M. Hofmann, H. C. Alt, T. Muschik, B. K. Meyer, E. Weigel, G. Müller-Vogt, M. Salk, E. Rupp, K. W. Benz, Optical investigations of defects in $Cd_{1-x}Zn_xTe$. Phys. Rev. B. 51, 10619–10630 (1995). doi:10.1103/PhysRevB.51.10619

[41] Y. Song, X. Zhang, L. Li, Z. Mo, J, Xu, S. Yu, X. Liu, J. Zhang, Temperature-dependent photoluminescence of cesium lead halide perovskite ($CsPbX_3$, X = Br, Cl, I) quantum dots. Mater. Res. Express 6, 115064 (2019). doi:10.1088/2053-1591/ab4911

[42] S. J. Zelewski, J. M. Urban, A. Surrente, D. K. Maude, A. Kuc, L. Schade, R. D. Johnson, M. Dollmann, P. K. Nayak, H. J. Snaith, P. Radaelli, R. Kudrawiec, R. J. Nicholas, P. Plochocka, M. Baranowski, Revealing the nature of photoluminescence emission in the metal-halide double perovskite $Cs_2AgBiBr_6$. J. Mater. Chem. C 7, 8350–8356 (2019). doi:10.1039/C9TC02402F

[43] K. Saeki, Y. Fujimoto, M. Koshimizu, T. Yanagida, K. Asai, Comparative study of scintillation properties of Cs_2HfCl_6 and Cs_2ZrCl_6. Appl. Phys. Express 9, 042602 (2016). doi:10.7567/APEX.9.042602

[44] H.-H. Kuo, Z.-L. Zhu, C.-S. Lee, Y.-K. Chen, S.-H. Liu, P.-T. Chou, A. K.-Y. Jen, Y. Chi. Bis-tridentate iridium(III) phosphors with very high photostability and fabrication of blue-emitting OLEDs. *Adv. Sci.* **5**, 1800846 (2018). doi: 10.1002/advs.201800846

[45] H.-H. Kuo, L.-Y. Hsu, J.-Y. Tso, W.-Y Hung, S.-H. Liu, P.-T. Chou, K.-T. Wong, Z.-L. Zhu, C.-S. Lee, A. K.-Y. Jen, Y. Chi. Blue-emitting bis-tridentate Ir(III) phosphors: OLED performances vs. substituent effects. *J. Mater. Chem. C* **6**, 10486–10496 (2018). doi: 10.1039/c8tc03194k

[46] S. Schmidbauer, A. Hohenleutner, B. König. Studies on the photodegradation of red, green and blue phosphorescent OLED emitters. *Beilstein J. Org. Chem*. **9**, 2088–2096 (2013). doi:10.3762/bjoc.9.245

[47] W. Hui, L. Chao, H. Lu, F. Xia, Q. Wei, Z. Su, T. Niu, L. Tao, B. Du, D. Li, Y. Wang, H. Dong, S. Zuo, B. Li, W. Shi, X. Ran, P. Li, H. Zhang, Z. Wu, C. Ran, L. Song, G. Xing, X. Gao, J. Zhang, Y. Xia, Y. Chen, W. Huang., Stabilizing black-phase formamidinium perovskite formation at room temperature and high humidity. Science 371, 1359–1364 (2021). doi:10.1126/science.abf7652

[48] F. Mathies, T. Abzieher, A. Hochstuhl, K. Glaser, A. Colsmann, U. W. Paetzold, G. Hernandez-Sosa, U. Lemmer, A. Quintilla, Multipass inkjet printed planar methylammonium lead iodide perovskite solar cells. J. Mater. Chem. A 4, 19207–19213 (2016). doi:10.1039/C6TA07972E

[49] S. Li, X. L. Xu, Y. Yang, Y. S. Xu, Y. Xu, H. Xia, Highly deformable high-performance paper-based perovskite photodetector with improved stability. ACS Appl. Mater. Interfaces 13, 31919–31927 (2013). doi:10.1021/acsami.1c05828

[50] M. Kaseem, K. Hamad, Y. G. Ko, Fabrication and materials properties of polystyrene/carbon nanotube (PS/CNT) composites: A review. Eur. Polym. J. 79, 36–62 (2016). doi:10.1016/j.eurpolymj.2016.04.011

[51] Y. Tu, L. Zhou, Y. Z. Jin, C. Gao, Z. Z. Ye, Y. F. Yang, Q. L. Wang, Transparent and flexible thin films of ZnO-polystyrene nanocomposite for UV-shielding applications. J. Mater. Chem. **20**, 1594–1599 (2010). doi:10.1039/B914156A

[52] H. Cui, D. Yao, R. Hensleigh, H. Lu, A. Calderon, Z. Xu, S. Davaria, Z. Wang, P. Mercier, P. Tarazaga, X. Zheng, Design and printing of proprioceptive three-dimensional architected robotic metamaterials. Science, 376, 1287–1293 (2022). doi:10.1126/science.abn0090

[53] R. Hensleigh, H. Cui, Z. Xu, J. Massman, D. Yao, J. Berrigan, X. Zheng. Charge-programmed three-dimensional printing for multi-material electronic devices. Nat. Electron. 3, 216–224 (2020). doi:10.1038/s41928-020-0391-2

[54] CrysAlisPro 1.171.39.45f.

[55] O. V. Dolomanov, L. J. Bourhis, R. J. Gildea, J. A. K. Howard, H. Puschmann, OLEX2: a complete structure solution, refinement and analysis program. J. Appl. Crystallogr. 42 339−341 (2009). doi:10.1107/S0021889808042726

[56] G. M. Sheldrick, SHELXT-integrated space-group and crystal-structure determination. Acta Crystallogr., Sect. A: Found. Adv. 71, 3−8 (2015). doi:10.1107/S2053273314026370

[57] G. M. Sheldrick, Crystal structure refinement with SHELXL. Acta Crystallogr., Sect. C: Struct. Chem. 71, 3−8 (2015). doi:10.1107/S2053229614024218

[58] S. J. Clark, M. D. Segall, C. J. Pickard, P. J. Hasnip, M. I. J. Probert, K. Refson, M. C. Payne, First principles methods using CASTEP. Z. Kristallogr. 220, 567–570 (2005). doi:10.1524/zkri.220.5.567.65075

[59] D. R. Hamann, M. Schlüter, C. Chiang, Norm-conserving pseudopotentials. Phys. Rev. Lett. 43, 1494–1497 (1979). doi:10.1103/PhysRevLett.43.1494

[60] W. Kohn, L. J. Sham, Self-consistent equations including exchange and correlation effects. Phys. Rev. 140, A1133–A1138 (1965). doi:10.1103/PhysRev.140.A1133

Chapter 4 Summary and Outlooks on the Supramolecular Approach for Halide Perovskites

This chapter aims to provide a comprehensive overview of research efforts centered on exploring the supramolecular approach for halide perovskites. Additionally, it will delve into a broader outlook concerning the future directions and potential implications within this new field of study.

4.1 Summary

Chapter 1 serves as an introductory exploration into the realm of halide perovskites. Within this chapter, the focus is placed on elucidating the unique properties of halide perovskites, a class of emerging ionic semiconductors. Key discussions revolve around the optoelectronic properties and synthesis methodologies regarding these innovative materials. Delving deeper, the chapter introduces the structural adaptability and dimensionality control of halide perovskites, emphasizing the pivotal role played by the metal halide octahedral unit as the fundamental building block and functional unit. Furthermore, the chapter discusses the diverse array of promising optoelectronic applications of halide perovskites. This chapter lays the foundation for the research projects explored in subsequent chapters.

Chapter 2 introduces the initial efforts in discovering and studying the supramolecular assembly approach for constructing various individual ionic octahedra. In this study, we found the crown ethers and $A_2M(IV)X_6$ will form a unique charge-neutral dumbbell structure with the formula (crown ether@A)$_2$M(IV)X_6 in solution. Single crystals with diverse packing geometries and symmetries will form as the solid assembly of this new supramolecular building block. This supramolecular assembly route introduces a new general strategy for designing halide perovskite structures with potentially new optoelectronic properties. We have successfully demonstrated that the dumbbell structural units are highly tunable, with crown ether = 18-Crown-6, 21-Crown-7; A = Cs^+, Rb^+, K^+; M = Te^{4+}, Sn^{4+}, Pt^{4+}, Se^{4+}, Ir^{4+}, Zr^{4+}, Ce^{4+}; X = Cl^-, Br^-, I^-, laying the foundation for highly tunable optoelectronic properties, including optical absorption and emission.

By conducting an in-depth investigation of the assembly process of the supramolecular approach, we decoupled the process into two critical steps: (1) solution stabilization of the dumbbell structural units and (2) the solid assembly of those units. The study provides us with molecular insights into the rational design and manipulation of new functional materials. The chemistry of synthesizing the family of supramolecular assembled single crystals is facile, reproducible, and straightforward. By simply varying the precursors in the synthesis, all four components of the dumbbell structural unit can be tuned in the solution stage. The unique crystal structure of the solid assembly may lead to new physical phenomena. For example, the optical absorption and emission of the material can be tuned by tuning the composition, packing geometry, and coordination environment of the $[MX_6]^{n-}$ building blocks. This study opens up opportunities for probing the supramolecular assembly mechanism and ignites fundamental research on the synthesis and characterization of supramolecular assembled functional materials.

In Chapter 3, I report that near-unity photoluminescence quantum yield (PLQY) blue emission can be achieved with the supramolecular assembly of less explored $[HfBr_6]^{2-}$ octahedral centers. Specifically, $(18C6@K)_2HfBr_6$ solid powders show a near-unity (96.22%) PLQY, which is much higher than K_2HfBr_6 (12.57%). Moreover, an efficient green emission (82.69% PLQY) can also be achieved due to the high chemical composition tunability of the dumbbell structural unit. We identify the emissions as self-trapped exciton (STE) emissions and conduct an in-depth investigation of the photophysics of these supramolecular assembled samples. These materials also maintain their exceptional luminescence when transformed into solution-processable semiconductor inks, laying the foundation for various applications, including thin film display application and emissive 3D printed architectures.

This study showcases the potential of luminescent materials with STE emissions as a viable platform for achieving blue and green emissions with ultra-high PLQY. By utilizing a supramolecular assembly approach, a new design principle for PL enhancement is unveiled, and the solution processability of these materials allows for various thin film and templating applications. Additionally, this research ignites further exploration into the synthesis and characterization of supramolecular assembled functional materials, paving the way for fundamental advancements in the field.

4.2 Outlooks

4.2.1 The Potential to Revolutionize the Display Industry

The primary and most immediate application for our technology lies within the rapidly growing display industry. According to a study by Precedence Research, the display market is anticipated to double in size over the next decade, projecting to exceed 300 billion USD by the year 2032. The substantial growth in the display industry presents a significant opportunity for our technology, especially if we can successfully replace the current materials utilized in displays. This potential market expansion underscores the substantial impact our materials could have within the display sector.

In the current display market, there are three predominant technological routes associated with specific types of materials: LED (light-emitting diodes), OLED (organic LED), and QLED (quantum dot LED). Compared to the current technologies, our supramolecular-assembly technology's unique attributes lie in the facile synthesis, solution processability, cost-effectiveness through the use of affordable metals, tunable emission colors, and enhanced stability, positioning it as a strong competitor against conventional materials in the LED, OLED, and QLED markets (**Table 4.1**).

Traditional LED materials are primarily covalent semiconductors, such as gallium nitride (GaN) and indium gallium nitride (InGaN). Their synthesis involves solid-state reactions at elevated temperatures around 1000°C, demanding high purity to prevent nonradiative recombination at crystal structure defects. In contrast, our technology relies on halide perovskites, which are emerging ionic semiconductors known for facile low-temperature (below 80°C) solution-based synthesis and high defect tolerance, simplifying the overall synthesis process.

OLEDs predominantly use organic materials, often with a metal component influencing their emission properties. Many OLEDs employ organometallic chelates like $Ir(mppy)_3$, but the cost

of iridium metal, priced at a few hundred dollars per gram, poses a challenge. In contrast, our materials utilize hafnium (Hf) and zirconium (Zr), which are significantly more affordable than iridium by two orders of magnitude, making our technology more cost-effective. Additionally, the versatility of our materials allows tunable emission colors, providing a distinct advantage over certain limitations of conventional OLED materials.

QLEDs are constructed with colloidal quantum dots and are acknowledged for efficient blue, green, and red light generation. However, their synthesis involves multiple steps at high temperatures, and material stability is hindered by aggregation issues, heavily relying on ligands protecting nanoscale quantum dots. In contrast, our materials have enhanced stability due to their ligand-free nature and stable crystal structure, offering a competitive edge over QLEDs by simplifying synthesis processes and ensuring robust material stability.

Table 4.1. A Comparison matrix showing how the key features of our product compare to existing products.

New Blue and Green Light Emitters vs. Competitors	GaN based LED	Ir-complex OLED	CdSe QLED	New Blue and Green Light Emitters	Advantage of Our Technology
Cost-effective solution fabrication	No	No	No	Yes	Our emitters are synthesized in common organic solution, while others require solid-state synthesis
Our emitters are synthesized in common organic solution	High (>900℃)	Moderate (~400℃)	Moderate (~200℃)	Low (80℃)	Our emitters are synthesized at 80℃, much lower than other materials, and are less energy intensive
Synthesis compatible with air	No	No	No	Yes	Our emitters are synthesized in air atmosphere, while others require inert atmosphere such as argon or nitrogen, so our equipment setup is much simpler

Contains precious metal	No	Yes	No	No	Our emitter utilize cheap and earth-abundant Hf and Zr metals
Photoluminescence quantum yield (PLQY)	~90%	~80%	~90%	~96%	Our emitters approaches the theoretical maximum PLQY value (100%), meaning it is extremely efficient in light generation
Longevity (stability)	High	Moderate	Moderate	High	The stability of our emitters under operating conditions are higher than the reported OLED and QLED materials
Structural tunability	Low	Moderate	Moderate	High	Our emitters have greater structural versatility and emission color tunability than other materials
Printable	No	No	No	Yes	Our emitters can be printed into various 2D and 3D structures with micrometer resolution

4.2.2 Unlock the Electroluminescence Capability of the Supramolecular Approach

Our research has not extended to investigating the suitability of our materials for electrically driven LEDs yet, however, it will be interesting to research into it. The development of electrically driven LEDs would require a dedicated and specialized investigation of the electroluminescence (EL) of the materials. Since near-unity PLQY has been achieved for both the blue and the green emitters, we are focusing on the PL study of this new family of supramolecular assembled materials. However, it is known that high PLQY is necessary for good LEDs, so it is worthwhile to pursue this direction in the next stage of our study.

The key to unlock the electroluminescence capability of the supramolecular approach is to make the material electrically conductive. There are two potential methods to realize this goal. The first one is to replace the insulating 18C6 with a conductive molecule. Porphyrin molecule

(**Figure 4.1**) is also capable of binding with a transitional metal cation in its center. It has shown good conductivity, and the HOMO energy levels are well aligned with the valence band of halide perovskites, such as methylammonium lead iodide[1]. The second method is to connect the electrically conductive halide perovskite octahedra using the supramolecular approach. In our current dumbbell structural unit, one octahedron is sandwiched by two crown ether supramolecular cations, making them isolated. If the dumbbell structural units are connected (**Figure 4.2**), then electrons and holes can be transported along the molecular chain. This new structural design requires the carefully selection of the cation crowned by the ring molecule. It has to be large enough to have enough coordination sites to bind with two octahedra, and it has to be electrically conductive.

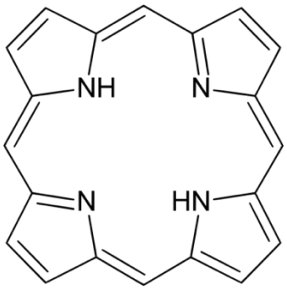

Figure 4.1. Potential electrically conductive ring molecules for supramolecular assembly: porphyrin.

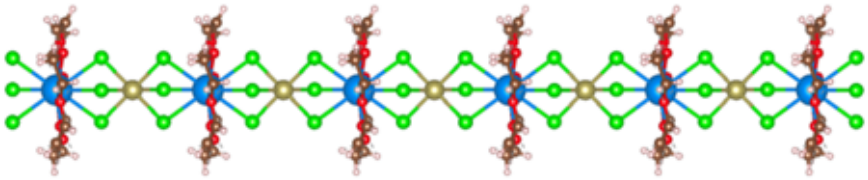

Figure 4.2. A hypothetical supramolecular assembled electrically conductive molecular wire.

4.2.3 New Platform for the Mechanism Study of the Energy Transfer Between Octahedral Complexes

In **Chapter 2.3**, I discussed the compositional and structural tunability of the dumbbell structural unit. Particularly, the metal center of the halide perovskite octahedra is highly tunable, and different metal centers can all form the same R-3 space group crystal structure using the same synthetic method. This means that we can easily incorporate multiple metal centers into one crystal structure. A previous work[2] on vacancy-ordered double perovskite has shown that six different metal elements can be randomly distributed in a single crystal, forming a high-entropy semiconductor (HES) (**Figure 4.3**). Dexter and Förster resonance energy transfer mechanisms among the different octahedra are both present according to the study in that work. Since the octahedra in the supramolecular assembled crystals are further separated from each

other, it would be interesting to study how the octahedra interact in this new crystal structure, and new optical phenomena may be discovered.

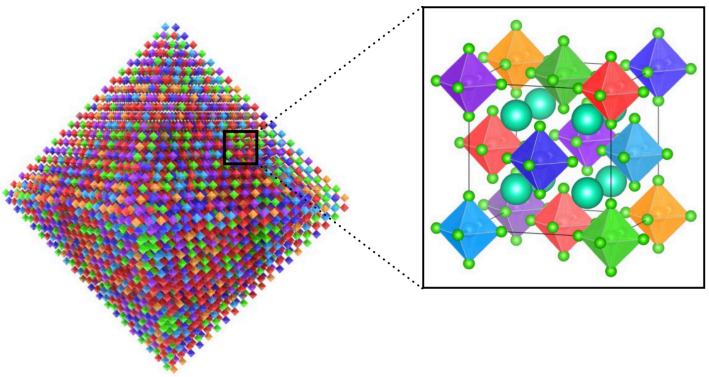

Figure 4.3. Schematic representation and crystal structure of the high-entropy semiconductor (HES) perovskite single crystal.[2] Copyright © 2023, Springer Nature.

Some initial study along this direction has been done on the Zr^{4+} doped $(18C6@K)_2HfBr_6$ structure. PLE spectra of 6% Zr^{4+}: $(18C6@K)_2HfBr_6$ (**Figure 4.4a**) and 33% Zr^{4+}: $(18C6@K)_2HfBr_6$ (**Figure 4.4b**) demonstrate that with excitation wavelength smaller than 285 nm, the $(18C6@K)_2HfBr_6$ PL peak is present, and the $(18C6@K)_2ZrBr_6$ PL peak is present across all excitation wavelengths from 245 nm to 330 nm. However, it is worth noting that apart from the combination of the individual effects of $(18C6@K)_2HfBr_6$ and $(18C6@K)_2ZrBr_6$, some extent of energy transfer from $[HfBr_6]^{2-}$ to $[ZrBr_6]^{2-}$ in the emission of the Zr^{4+} doped $(18C6@K)_2HfBr_6$ samples is also possible. It has also been shown in $[Hf/ZrCl_6]^{2-}$ and $[Hf/ZrBr_6]^{2-}$ alloyed vacancy-ordered double perovskite systems that there is an energy transfer from $[HfX_6]^{2-}$ to the lower energy $[ZrX_6]^{2-}$ ($X = Cl^-$ or Br^-)[3-6]. In our supramolecular assembled samples, the octahedra are further separated in space (10.75503(6) Å in $(18C6@K)_2HfBr_6$, and 10.76943(6) Å in $(18C6@K)_2ZrBr_6$), but still within the length scale of the Förster resonance energy transfer mechanism (below 10 nm). As hypothesized, PL spectra of 6% Zr^{4+}: $(18C6@K)_2HfBr_6$ (**Figure 4.5a**) and 33% Zr^{4+}: $(18C6@K)_2HfBr_6$ (**Figure 4.5b**) at 275 nm excitation show that the PL intensity ratio of the deconvolved $(18C6@K)_2ZrBr_6$ and $(18C6@K)_2HfBr_6$ exceeds the molar ratio of Zr^{4+} to Hf^{4+}, indicating energy transfer from $[HfBr_6]^{2-}$ to $[ZrBr_6]^{2-}$. The PLE spectra of $(18C6@K)_2HfBr_6$ and 6% Zr^{4+}: $(18C6@K)_2HfBr_6$ at 548 nm emission (**Figure 4.6a**) both feature two broad excitation bands around 250 nm and 290 nm, indicating that in the alloyed sample, the excited state of $[HfBr_6]^{2-}$ is accessed. However, the PLE of 6% Zr^{4+}: $(18C6@K)_2HfBr_6$ also has a shoulder peak around 320 nm, which can be attributed to the excitation state of $(18C6@K)_2ZrBr_6$ (**Figure 4.6b**). Hence, both $[HfBr_6]^{2-}$ and $[ZrBr_6]^{2-}$ are excited and contribute to the emission peak at 548 nm. As a result, we speculate that the performance of 6% Zr^{4+}: $(18C6@K)_2HfBr_6$ is a combination of intrinsic $(18C6@K)_2ZrBr_6$ STE emission and certain energy transfer from $[HfBr_6]^{2-}$ to $[ZrBr_6]^{2-}$.

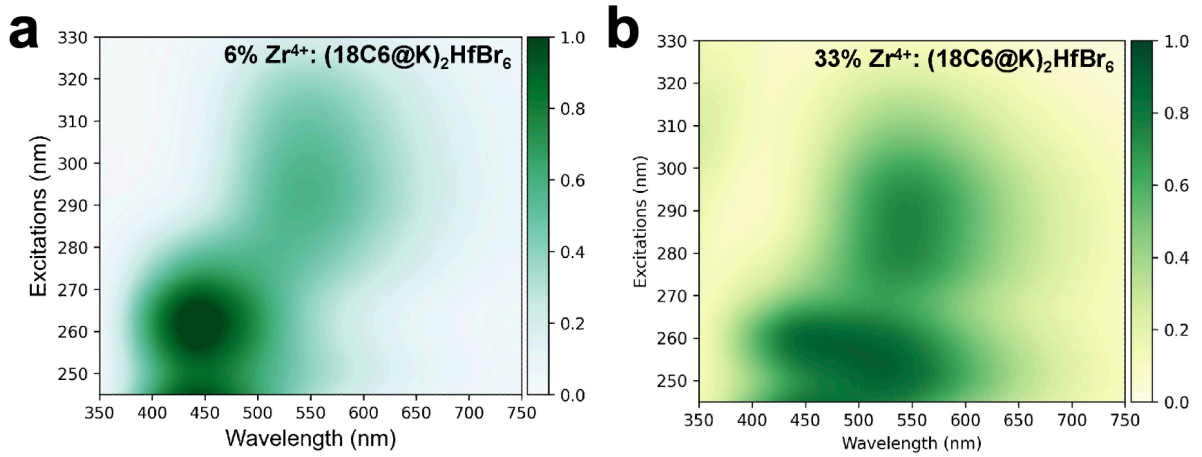

Figure 4.4. Photoluminescence excitation (PLE) spectroscopy of (a) 6% Zr^{4+}: $(18C6@K)_2HfBr_6$ powders and (b) 33% Zr^{4+}: $(18C6@K)_2HfBr_6$ powders.

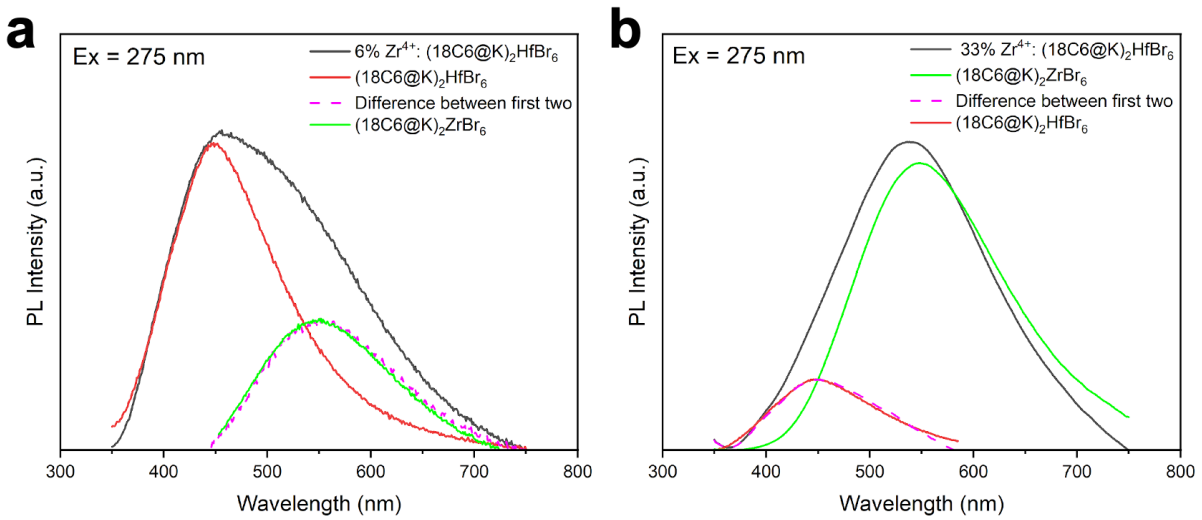

Figure 4.5. PL measurement of Zr^{4+}doped $(18C6@K)_2HfBr_6$ powders at room temperature at 275 nm excitation. (a) 6% Zr^{4+}: $(18C6@K)_2HfBr_6$. (b) 33% Zr^{4+}: $(18C6@K)_2HfBr_6$.

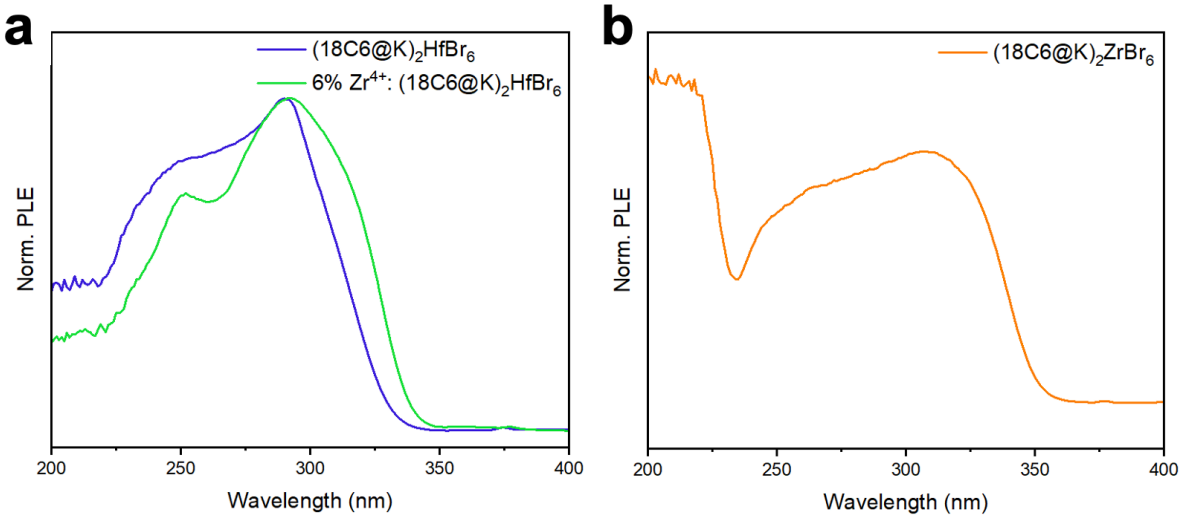

Figure 4.6. PLE spectra of (a) $(18C6@K)_2HfBr_6$ powders and 6% Zr^{4+}: $(18C6@K)_2HfBr_6$ powders at 548 nm emission; (b) $(18C6@K)_2ZrBr_6$ powders at 548 nm emission.

4.2.4 Rich Structural Tunability of the Supramolecular Approach

4.2.4.1 Boosting the PLQY through a More Rigid Structure

Previous highly phosphorescent Ir(III) complexes studies have shown that improvement of PLQY is expected with more rigid macrocycles or cages[7]. The supramolecular assembly approach offers flexibility in tuning the organic ligands, so we can also consider replacing crown ether with other structurally different ligand for the cation. For example, cryptand is more rigid than crown ether, and it would be interesting to see if cryptand can further boost the PLQY.

As an initial demonstration of this concept, we explore using 2.2.2-Cryptand (C222) as an alternative ligand. We have successfully demonstrated the feasibility of stabilizing Hf and Zr halide octahedral clusters with C222. Our previous solution-based synthesis of these new materials is applied. Upon mixing the C222, KBr, and $HfBr_4$/$ZrBr_4$ precursors with 2:2:1 molar ratio in acetonitrile, a white flocculent precipitate immediately forms. The precipitate is quite emissive. According to the colors of the emissions (blue for the Hf sample and yellow for the Zr sample), we suspect that the Hf and Zr halide octahedra are stabilized in the powders. PXRD (**Figure 4.7**) indicates a new phase has been achieved. Raman spectroscopy (**Figure 4.8**) analysis suggests that the metal halide octahedral units are present within the crystal, as the corresponding vibrational modes have been identified. However, due to the challenges in obtaining high-quality single crystals, we cannot resolve the crystal structures at this stage.

Nonetheless, preliminary results indicate that samples synthesized with C222 as the ligand exhibit a blue emission with 19.16% PLQY (Hf sample) and a yellow emission with 26.70% (Zr sample). The samples are not as pure as the crown ether samples, so the PLQY values may be further improved when the synthesis is optimized. We would also like to highlight that compared to the crown-ether samples; these cryptand-assembled samples display red-shifted emission colors (**Figure 4.9, 4.10**).

The study is still at the initial stage, nevertheless, these intriguing initial observations suggest that further exploration and refinement of our synthetic method may unlock the potential for improved PLQY using different ligands, a promising avenue for future research in this field.

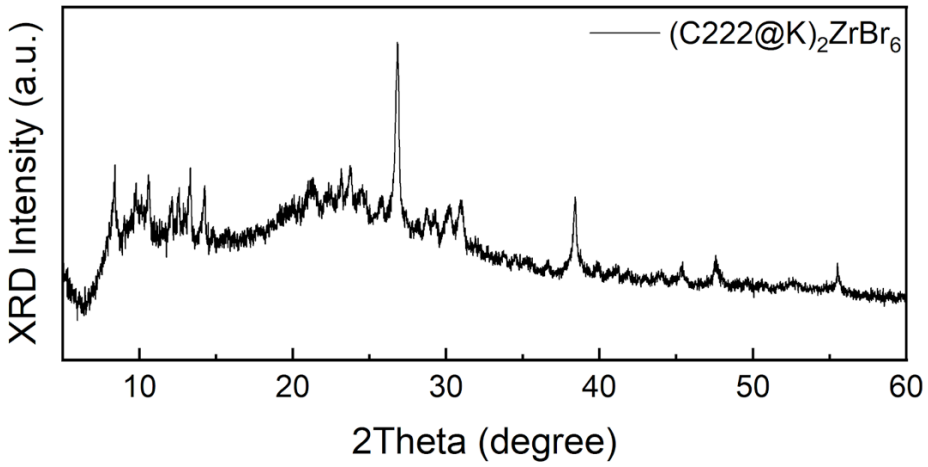

Figure 4.7. PXRD pattern of the C222 assembled $[ZrBr_6]^{2-}$ powders, labelled as $(C222@K)_2ZrBr_6$.

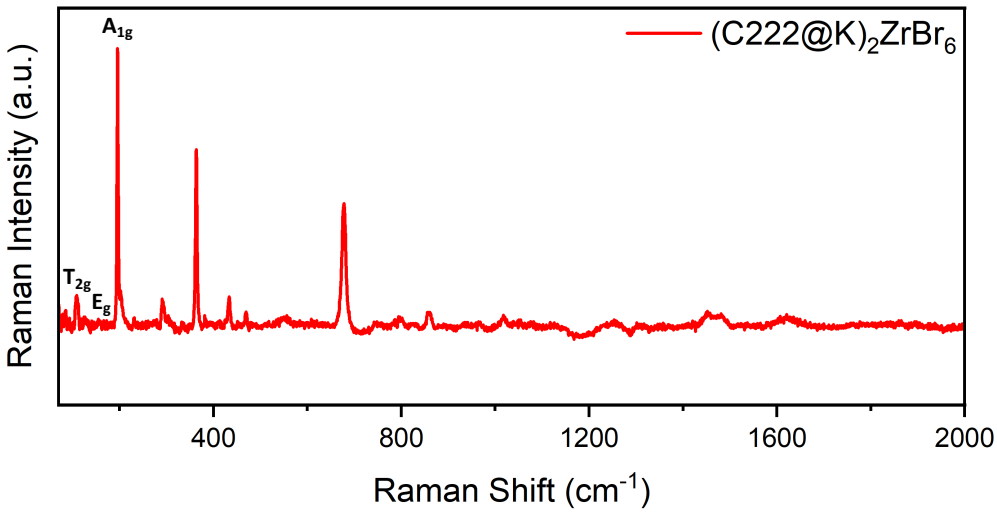

Figure 4.8. Raman spectroscopy of the C222 assembled $[ZrBr_6]^{2-}$ powders, labelled as $(C222@K)_2ZrBr_6$. The distinct Raman-active modes including the low-frequency asymmetric bending mode T_{2g} and the high-frequency symmetric stretching mode A_{1g} corresponding to the O_h-symmetric vibrating $[ZrBr_6]^{2-}$ have been identified. The asymmetric stretching mode E_g is quite weak.

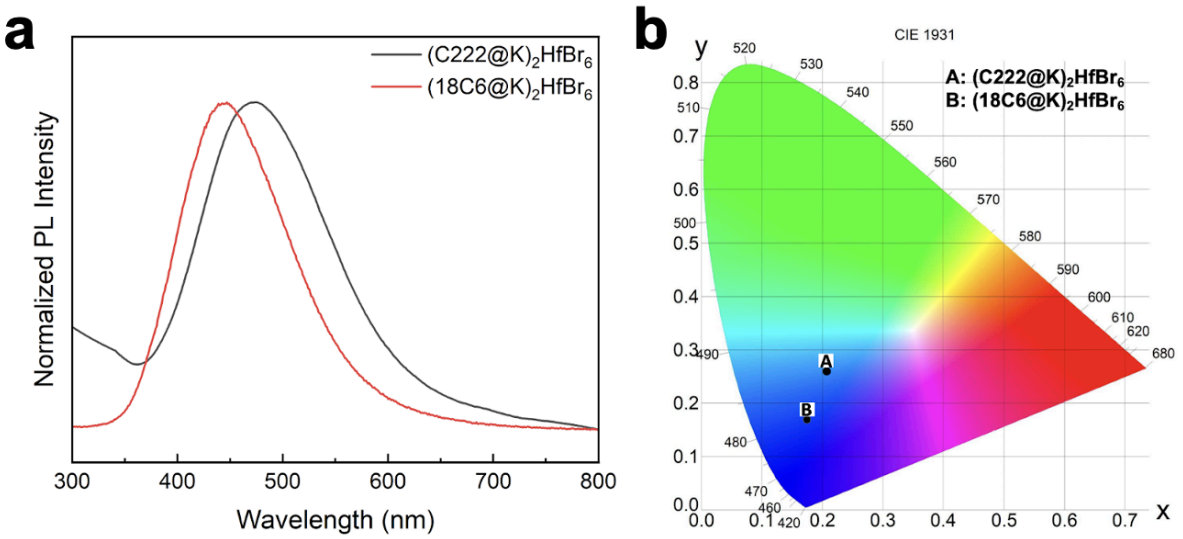

Figure 4.9. Comparison of (a) the PL spectra and (b) the CIE 1931 color coordinates of $(18C6@K)_2HfBr_6$ powders and the C222 assembled $[HfBr_6]^{2-}$ powders, labelled as $(C222@K)_2HfBr_6$. The CIE 1931 coordinates are (0.20699, 0.25982) and (0.17438, 0.16922) for $(C222@K)_2HfBr_6$ and $(18C6@K)_2HfBr_6$, respectively.

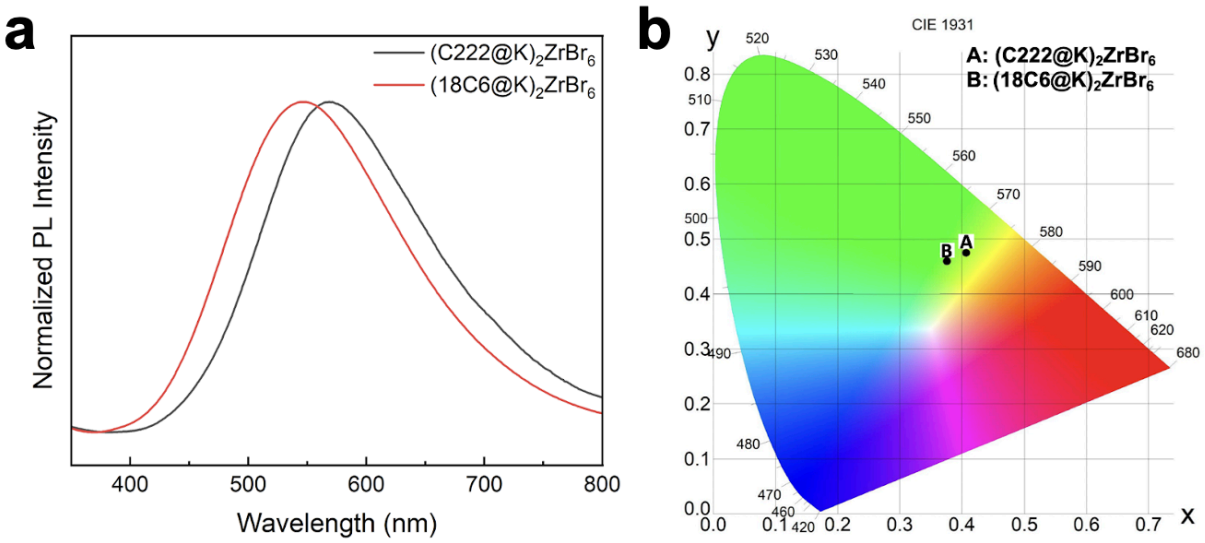

Figure 4.10. Comparison of (a) the PL spectra and (b) the CIE 1931 color coordinates of $(18C6@K)_2ZrBr_6$ powders and the C222 assembled $[ZrBr_6]^{2-}$ powders, labelled by $(C222@K)_2ZrBr_6$. The CIE 1931 coordinates are (0.40693, 0.47474) and (0.37601, 0.45927) for $(C222@K)_2ZrBr_6$ and $(18C6@K)_2ZrBr_6$, respectively.

4.2.4.2 Assembly of a Variety of Metal Halide Complexes

The current research delves into the supramolecular assembly of metal halide octahedral complexes (MX_6), with the metal center typically being a tetravalent metal cation. However, as elucidated in **Chapter 1.2.2**, a diverse array of metal halide complexes exists (**Figure 4.11**).

For instance, divalent cations such as Pb^{2+} and Sn^{2+}, as well as trivalent ones like Sb^{3+} and Bi^{3+}, can also form 6-coordinated octahedral complexes. Additionally, there are reports of 4-coordinated tetrahedral and 5-coordinated pyramid metal halide complexes. Moreover, through the sharing of halides between metal centers, metal halides can give rise to various structures, including dimers, trimers, and even molecular chains. The rich chemistry of metal halides, coupled with the versatility of supramolecular assembly, presents a wide range of opportunities in this domain.

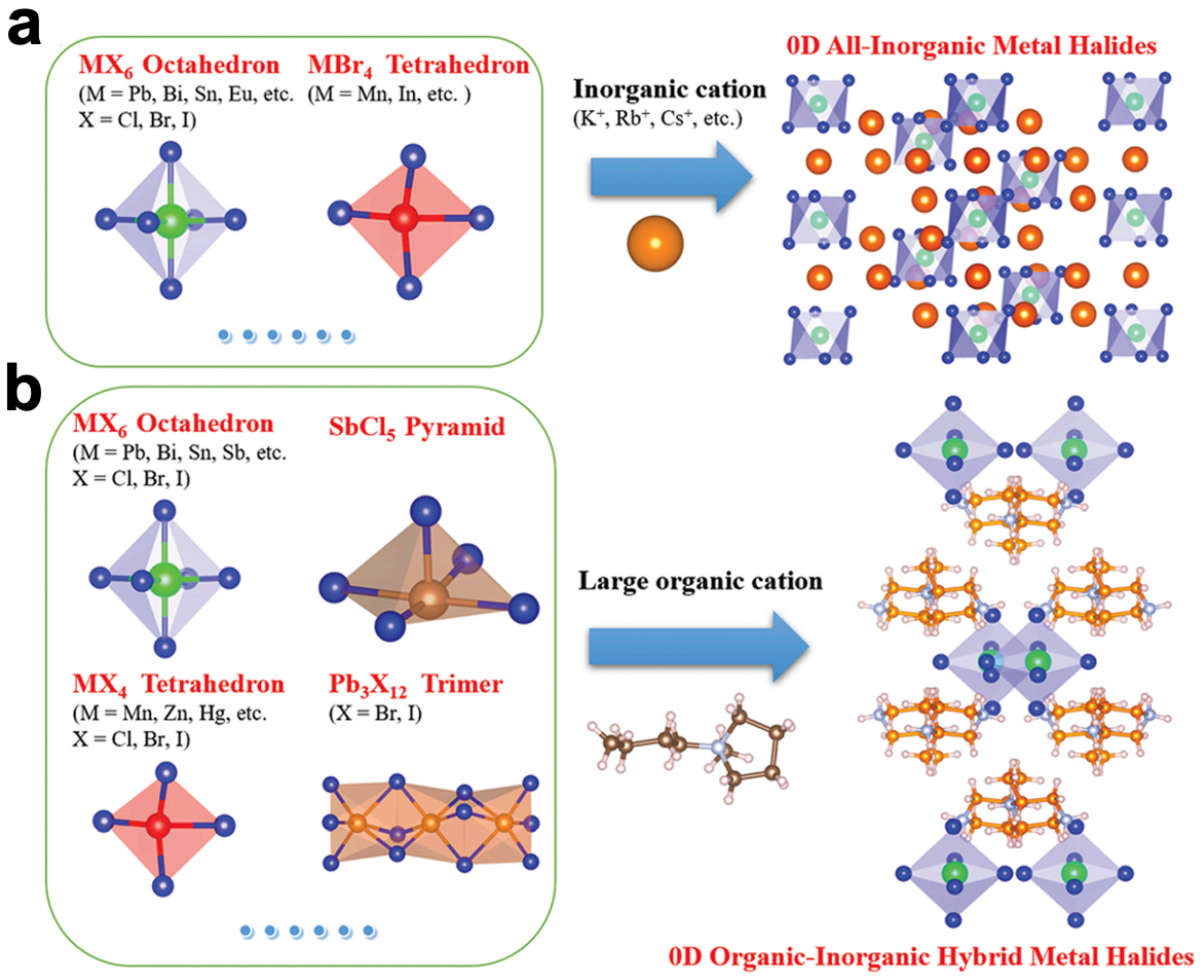

Figure 4.11. Rich chemistry of metal halides. Design principles of (a) 0D all-inorganic metal halides and (b) 0D organic-inorganic hybrid metal halides focusing on different building units to address their interesting structural models.[8] © The Royal Society of Chemistry 2021.

4.2.4.3 Polarized Luminescence Enabled by Chiral Structures

The generation of polarized light, particularly circularly polarized luminescence (CPL), is a phenomenon rooted in the luminescent quantum states of chiral nanostructures or molecules dispersed within a medium. CPL arises from a mechanism wherein a photon emitted from a chiral excited state becomes polarized due to the non-zero dot product between the electric

dipole transition moment and the imaginary magnetic dipole transition moment associated with the electronic transition responsible for luminescence.

Chiral low-dimensional metal halides represent a promising avenue for harnessing CPL due to their unique combination of properties from both chiral materials and low-dimensional metal halides. Chiral materials possess a natural ability to manipulate the circular polarization states of light. By leveraging the strategy of chirality transfer from organic chiral ligands, researchers have extensively explored and developed the chiroptoelectronic properties of low-dimensional metal halides, including CPL[9]. CPL involves the emission of light with a specific polarization state, characterized by the rotation of the electric field vector in a circular manner. Owing to its distinctive optical properties, CPL has found wide-ranging applications in critical domains such as 3D imaging and printing, sensing and probing, and quantum computing. Thus, the integration of chiral low-dimensional metal halides opens up exciting possibilities for advancing CPL technology and its applications.

The supramolecular approach presents an innovative design strategy for chiral low-dimensional metal halides at the molecular level. Leveraging the diverse symmetries inherent in supramolecular cations, this approach facilitates access to various crystal structures with chiral point groups (**Figure 4.12a**). Preliminary studies[10,11] have demonstrated the generation of CPL through the crown ether-assisted assembly of 0D metal halides (**Figure 4.12b, c**). There remains ample room for further exploration and advancement in this promising direction.

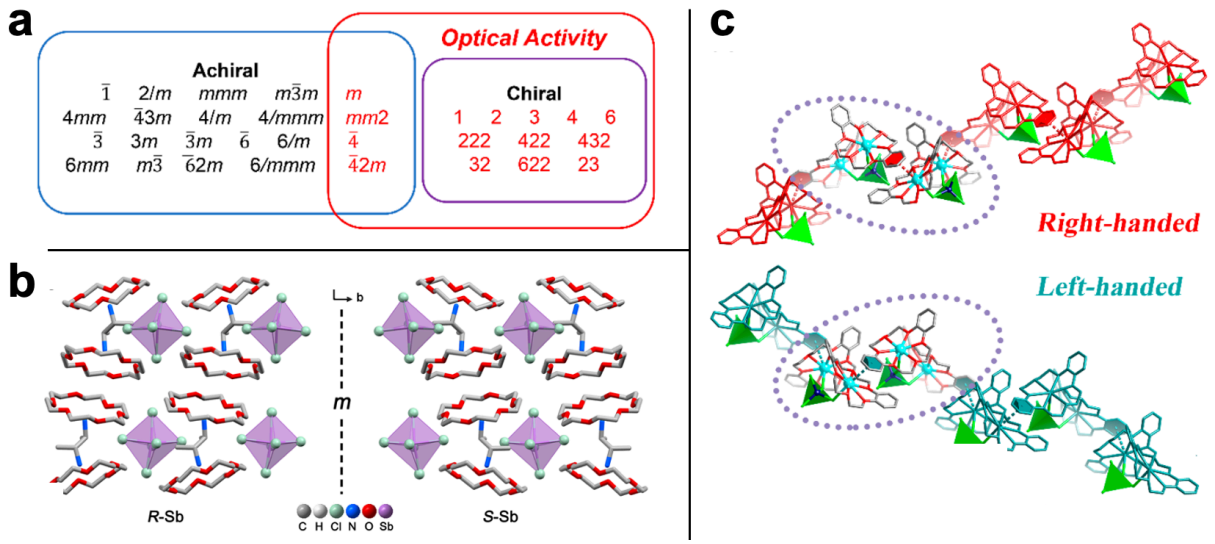

Figure 4.12. Structures with circularly polarized luminescence. (a) Relationship between crystal symmetry, chirality, and optical activity.[10] Copyright © 2019, American Chemical Society. (b) Single-crystal structures of the chiral 0D antimony halides. Chiral R-Sb and S-Sb crystallize in tetragonal chiral space groups of $P4_32_12$ and $P4_12_12$, respectively, subordinate to the 422 crystal symmetry. [11] © The Royal Society of Chemistry 2024. (c) Right-handed helix (colored in red) and left-handed helix (colored in blue) built from $[K(dibenzo\text{-}18\text{-}crown\text{-}6)]^+$ and $[MnCl_4]^{2-}$.[10] Copyright © 2019, American Chemical Society.

4.2.4.4 Ferroelectricity through Non-Centrosymmetric Symmetries

Ferroelectricity is a pivotal phenomenon characterized by the displacement of positive and negative charge centers in crystal structure with non-centrosymmetric symmetry (**Figure 4.13**). Ferroelectric materials possess the remarkable ability to store and switch spontaneous electric polarization, rendering them valuable in various applications. This class of functional materials exhibits exceptional dielectric constants, superior pyroelectricity and piezoelectricity, and other optical effects, making them highly sought after for technological advancements.

Despite the significant advancement made in ferroelectric oxide perovskites research, exploration into ferroelectric properties within the halide perovskites remains relatively scarce (**Figure 4.14**). The infancy of halide perovskite ferroelectrics is evidenced by the limited number of reported works on the subject thus far. Consequently, there exists a compelling need for intensified investigation and attention towards the development of ferroelectricity in halide perovskites.

The supramolecular approach introduces a novel strategy for designing ferroelectric halide perovskites. As discussed in **Chapter 4.2.4.2**, the versatility of supramolecular assembly allows for the creation of diverse metal halide complexes. By rationally engineering the crystal symmetry through the design of supramolecular cations, a variety of ferroelectric structures can be realized. Additionally, the interaction between the supramolecular cation and the metal halide anion can induce distortion within the metal halide complexes, amplifying electrical dipoles. Embracing this direction of research promises to discover novel insights and open up new possibilities for the advancement of ferroelectric functional materials in the future.

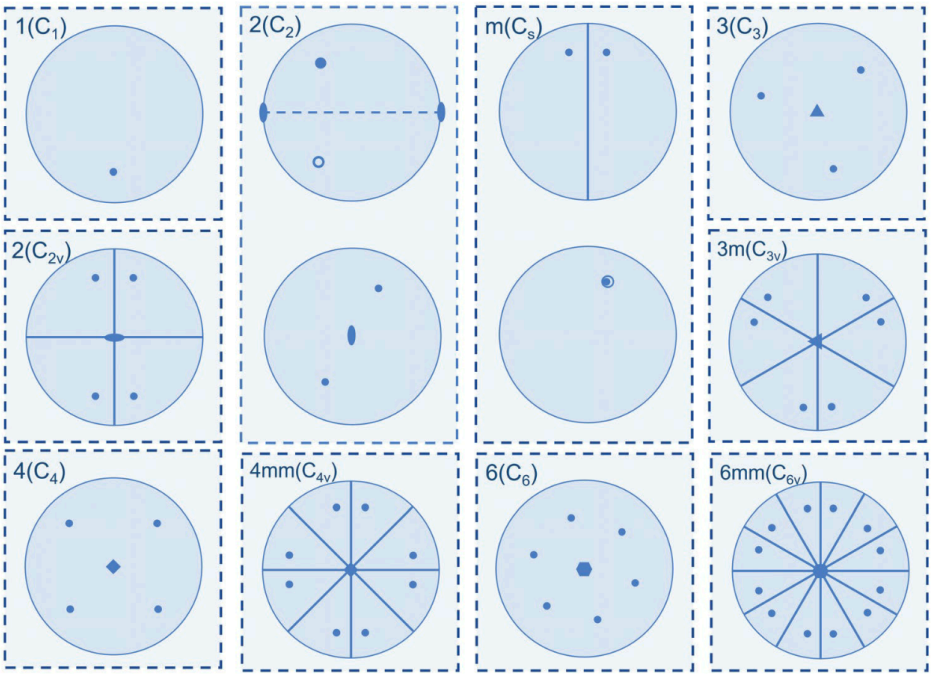

Figure 4.13. Equatorial plane projection of 10 ferroelectric point groups.[12] © 2023 Wiley-VCH GmbH.

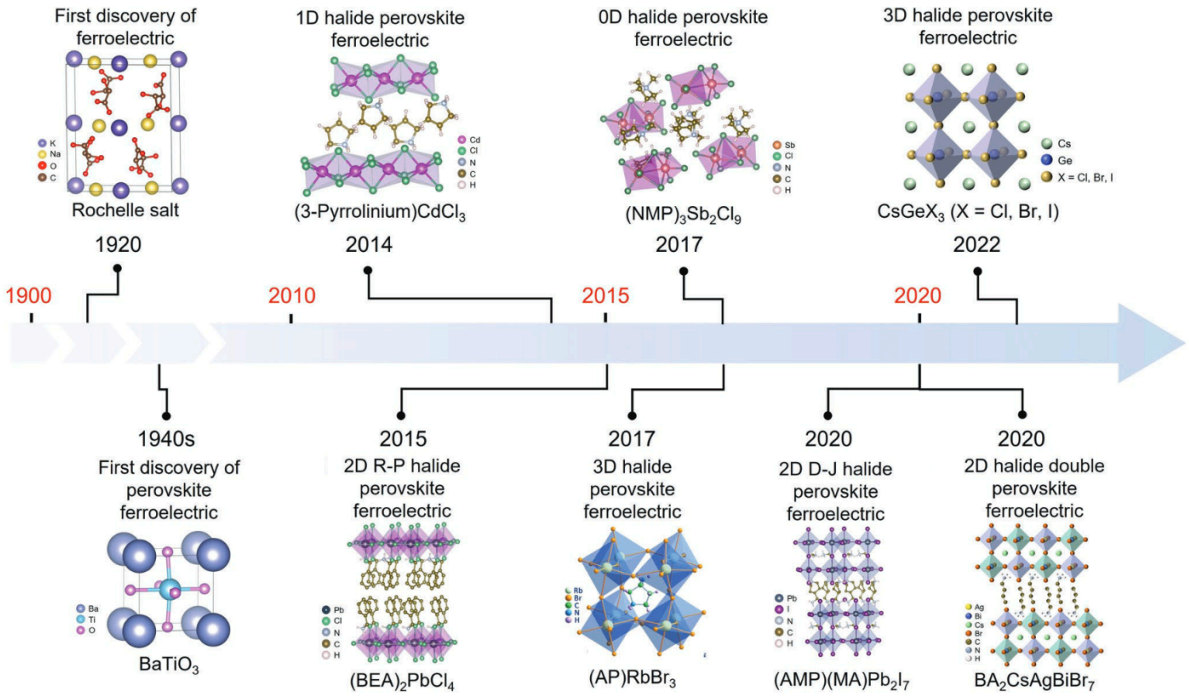

Figure 4.14. The discovery of ferroelectric and major development of halide perovskite ferroelectrics. [12] © 2023 Wiley-VCH GmbH.

4.3. References

[1] G. Reddy, R. Katakam, K. Devulapally, L. A. Jones, E. D. Gaspera, H. M. Upadhyaya, N. Islavath, L. Giribabu, Ambient stable, hydrophobic, electrically conductive porphyrin hole-extracting materials for printable perovskite solar cells. J. Mater. Chem. C, 7, 4702–4708 (2019). doi:10.1039/C9TC00605B

[2] M. C. Folgueras, Y. Jiang, J. Jin, P. Yang, High-entropy halide perovskite single crystals stabilized by mild chemistry. Nature, 621, 282–288 (2023). doi:10.1038/s41586-023-06396-8

[3] K. Saeki, Y. Fujimoto, M. Koshimizu, D. Nakauchi, H. Tanaka, T. Yanagida, K. Asai, Luminescence and scintillation properties of Cs_2HfBr_6 and Cs_2ZrBr_6 crystals. J. Appl. Phys. 57, 030310 (2018). doi:10.7567/JJAP.57.030310

[4] V. Vaněček, J. Páterek, R. Král, M. Buryi, V. Babin, K. Zloužeová, S. Kodama, S. Kurosawa, Y. Yokota, A. Yoshikawa, M. Nikl, Cs_2HfCl_6 doped with Zr: Influence of tetravalent substitution on scintillation properties. J. Cryst. Growth 573, 126307 (2021). doi:10.1016/j.jcrysgro.2021.126307

[5] R. Král V. Babin, E. Mihóková, M. Buryi, V. V. Laguta, K. Nitsch, M. Nikl, Luminescence and charge trapping in Cs_2HfCl_6 single crystals: optical and magnetic resonance spectroscopy study. J. Phys. Chem. C 121, 12375–12382 (2017). doi:10.1021/acs.jpcc.7b02327

[6] M. Buryi, R. Král, V. Babin, J. Páterek, V. Vaněček, P. Veverka, M. Kohoutková, V. Laguta, M. Fasoli, I. Villa, F. Cova, A. Vedda, M. Nikl, Trapping and recombination centers in cesium hafnium chloride single crystals: EPR and TSL Study. J. Phys. Chem. C 123, 19402–19411 (2019). doi:10.1021/acs.jpcc.9b05760

[7] Y. You, S. Y. Park. Phosphorescent iridium(III) complexes: toward high phosphorescence quantum efficiency through ligand control. Dalton Trans., 1267–1282 (2009). doi: 10.1039/B812281D

[8] M. Li, Z. Xia, Recent progress of zero-dimensional luminescent metal halides. Chem. Soc. Rev., 50, 2626 (2021). doi: 10.1039/d0cs00779j

[9] H. Lu, Z. V. Vardeny, M. C. Beard, Control of light, spin and charge with chiral metal halide semiconductors. Nat. Rev. Chem., 6, 470–485 (2022). doi: 10.1038/s41570-022-00399-1

[10] J. Zhao, T. Zhang, X.-Y. Dong, M.-E. Sun, C. Zhang, X. Li, Y. S. Zhao, S.-Q. Zang, Circularly Polarized Luminescence from Achiral Single Crystals of Hybrid Manganese Halides. J. Am. Chem. Soc., 141, 15755−15760 (2019). doi:10.1021/jacs.9b08780

[11] X. Han, P. Cheng, S. Han, Z. Wang, J. Guan, W. Han, R. Shi, S. Chen, Y. Zheng, J. Xu, X.-H. Bu, Multi-stimuli-responsive luminescence enabled by crown ether anchored chiral antimony halide phosphors. Chem. Sci.,15, 3530 (2024). doi: 10.1039/d3sc06362c

[12] W. Zheng, X. Wang, X. Zhang, B. Chen, H. Suo, Z. Xing, Y. Wang, H.-L. Wei, J. Chen, Y. Guo, F. Wang, Emerging halide perovskite ferroelectrics. Adv. Mater., 35, 2205410 (2023). doi: 10.1002/adma.202205410